JOURNAL OF THE AERONAUTICAL SCIENCES

VOLUME 19 SEPTEMBER, 1952 NUMBER 9

CONTENTS

Flutter Analysis of Complex Airplanes by Experimental Methods ..... E. BERKELEY KINNAMAN 577

Analysis of Oval Rings by Fourier Series ..... ROLAND J. BENJAMIN 585

Two-Dimensional Airfoils at Moderate Hypersonic Velocities ..... WILLIAM H. DORRANCE 593

The Effects on Dynamic Lateral Stability and Controllability of Large Artificial Variations in the Rotary Stability Derivatives ..... ROBERT O. SCHADE, ORDWAY B. GATES, JR., AND JAMES L. HASSELL, JR. 601

Investigation into the Operating Cycle of a Two-Dimensional Supersonic Wind Tunnel ..... G. V. BULL 609

A Review of Certain Analysis Methods for Swept-Wing Structures ..... M. L. WILLIAMS 615

The Development of Cascade Profiles for High Subsonic Potential Flows ..... HSUAN YEH 630

Readers' Forum: "Comments on 'Remarks on Dynamic Loads in Landing,'" by H. Norman Abramson; "A Third Kind of 'Incompressible' Fluid," by A. Martinot-Lagarde; "Computation of Possio's Integral for Linearized Supersonic Flow," by Frederic E. Fuller; "Remarks on 'Correction for Aspect Ratio of the Indicial Lift Functions of Wagner and Küssner,'" by S. F. Shen; "Hooke's Gas in Aerothermodynamics," by Ing. Ennio Mattioli; "Reply to Comments on 'Horizontal Tail Loads in Abrupt Pull-Ups from Level Flight,'" by J. L. Decker; "Note on the Calculation of Transport Properties of Gas Mixtures," by Eldon L. Knuth; "The Prandtl Membrane Analogy for Temperature Fields with Permanent Heat Sources or Sinks," by Paul J. Schneider; "Note on the Theory of Hurricanes," by Theodore Theodorsen; "On Boundary-Layer Temperature Recovery Factors," by B. des Clers and J. Sternberg; "Secondary Flow in Cascades," by H. G. Loos and J. Zwaaneveld; "The von Kármán Integral Method as Applied to a Turbulent Boundary Layer," by Nguyen Van Le 639–648

Published by the

INSTITUTE OF THE AERONAUTICAL SCIENCES, INC.

JOURNAL OF THE AERONAUTICAL SCIENCES

Editor: HUGH L. DRYDEN, *Director, N.A.C.A.*

Associate Editor: ROBERT R. DEXTER *Managing Editor:* BERNEICE H. JARCK

Editorial Committee

Aerodynamics

Francis Clauser
Howard Emmons
Alexander Flax
R. Paul Harrington
R. T. Jones
Carl Kaplan
H. W. Liepmann
C. C. Lin
H. F. Ludloff
Harold Luskin
John R. Markham
Clark B. Millikan
Shatswell Ober
W. Bailey Oswald
Allen B. Puckett
Elliott G. Reid
H. J. E. Reid
Russell Robinson
G. B. Schubauer
W. R. Sears
John Stack
Theodore von Kármán
Richard von Mises

Air Transport

Charles Froesch
J. A. Herlihy
R. D. Kelly
Otto E. Kirchner
Jerome Lederer
John C. Leslie
R. Dixon Speas

Flight Testing

W. K. Ebel
R. R. Gilruth
Melvin N. Gough
E. G. Stout

Structures and Materials

W. B. Bleakney
E. W. Conlon
L. H. Donnell
E. C. Hartmann
N. J. Hoff
Samuel Levy
E. E. Lundquist
Alfred S. Niles
W. Ramberg
E. Reissner
F. R. Shanley
H. W. Sibert
C. R. Strang
S. Timoshenko
H. S. Tsien
Chi-Teh Wang

Rotating Wing Aircraft

F. B. Gustafson
K. H. Hohenemser
Bartram Kelley
R. B. Maloy
Ralph McClarren
R. H. Miller
R. H. Prewitt
Igor I. Sikorsky

Vibration and Flutter

Lee Arnold
M. A. Biot
R. L. Bisplinghoff
William Bollay
Chieh-Chien Chang
I. E. Garrick
Martin Goland
J. P. Den Hartog

Aircraft Design

W. E. Beall
W. K. Ebel
Hall L. Hibbard
Richard Hutton
C. L. Johnson
A. A. Kartveli
C. J. McCarthy
Fred E. Weick
Robert J. Woods

Electronics in Aviation

K. C. Black
E. F. Herzog
David S. Little
D. K. Martin
George Rappaport
Paul Rosenberg
L. M. Sherer

Physiologic Problems

H. G. Armstrong
Louis H. Bauer
Robert J. Benford
Eugene Du Bois
W. Randolph Lovelace, II
Ross A. MacFarland

Fuels and Oils

D. P. Barnard
J. H. Doolittle
Graham Edgar
R. T. Goodwin
S. D. Heron
A. M. Rothrock

Flight Propulsion

George W. Brady
Frank W. Caldwell
L. S. Hobbs
E. E. Johnson
Joseph Keenan
R. P. Kroon
Hans Reissner
Abe Silverstein
C. Fayette Taylor
E. S. Taylor
P. Taylor
E. S. Thompson
H. S. Tsien

Instruments

Allan G. Binnie
J. R. Bradburn
Charles H. Colvin
C. S. Draper
S. G. Eskin
O. E. Esval
H. W. Holzapfel
W. L. Howland
George H. Purcell
C. F. Savage
O. Hugo Schuck
C. L. Seward, Jr.
L. D. Statham
R. C. Sylvander
D. K. Warner

Meteorology

C. F. Brooks
D. M. Little
E. J. Minser
F. W. Reichelderfer
H. C. Willett

SUBSCRIPTION RATES

JOURNAL OF THE AERONAUTICAL SCIENCES, Published Monthly.—United States and Possessions: 1 Year, $12.00; Single Copies, $1.50. Foreign Countries Including Canada (American Currency Rates): 1 Year, $13.00; Single Copies, $1.50.

AERONAUTICAL ENGINEERING REVIEW, Published Monthly.—United States and Possessions: 1 Year, $3.00; Single Copies, $0.50. Foreign Countries Including Canada (American Currency Rates): 1 Year, $3.50; Single Copies, $0.50.

Notices of change of address should be sent to the Institute at least 30 days prior to actual change of address.

Manuscripts for publication, proofs, and all correspondence should be addressed to the Editorial Office of the JOURNAL.

Correspondence regarding subscriptions may be addressed to Publication Office, 20th and Northampton Sts., Easton, Pa., or to the Editorial Office of the JOURNAL OF THE AERONAUTICAL SCIENCES, 2 East 64th Street, New York 21, New York.

Copyright, 1952, by the Institute of the Aeronautical Sciences, Inc.

Entered as Second Class Matter at the Post Office, Easton, Pa., May 1, 1937. Acceptance for mailing at a special rate of Postage provided for in the Act of August 24, 1912. Authorized April 29, 1937.

JOURNAL OF THE AERONAUTICAL SCIENCES

VOLUME 19 SEPTEMBER, 1952 NUMBER 9

Flutter Analysis of Complex Airplanes by Experimental Methods

E. BERKELEY KINNAMAN*

Boeing Airplane Company

ABSTRACT

The analysis of the flutter potentialities of a highly elastic airplane having a wing of high aspect ratio with large flexibly mounted concentrated masses distributed along the span has proved to be amenable to solution by the use of elastically and dynamically scaled wind-tunnel models. Experimental flutter testing at Boeing has progressed from a simple half-wing cantilever model of 1946 to today's almost completely scaled flutter models tested in reasonable simulation of free flight.

Continued development of experimental flutter analysis techniques and correlation with full-scale flight testing and theory are needed to permit more accurate predictions of the flutter characteristics of an airplane prior to the final design and flight stages.

INTRODUCTION

THE PREVENTION OF THE DYNAMIC INSTABILITY of an airplane, called "flutter," is approaching "big business" in the aircraft industry and research agencies.

Primarily, this field of engineering is preventive medicine for the high-performance aircraft now in progress of design, since flutter engineers are required to ensure that flutter is not designed into the airplane.

Being certain that a complex airplane will be free from flutter is becoming increasingly more difficult if not impossible. The growth of the facilities available to the flutter engineer have not in fact been so rapid as the increase in design problems. At Boeing, we have been faced with the problem of wing-supported concentrated masses from the initiation of the airplane design. We have been faced with problems such as low frequencies, highly swept wings, variable density, and interaction of components.

Presented at the Aeroelasticity Session, Twentieth Annual Meeting, I.A.S., New York, January 28–February 1, 1952.

*Vibration Unit Chief.

PRELIMINARY FLUTTER ANALYSIS

The approach to the analysis of the flutter characteristics of an airplane design is similar to most other engineering problems. Ideally, we need to answer rapidly the preliminary design engineers' questions, first, on the probability of flutter of the airplane configuration as a whole and, second, as to the effects, flutterwise, of all the variations that show promise of increasing the efficiency of the flight article.

Obviously, long and involved calculations are impractical in this early stage. In most instances, the flutter analyst can do no more than call on intuition based on experience and on the available literature to recommend preferable assemblies of components. As the design begins to take shape and coordination between the aerodynamics, power plant, structures, and equipment has resolved the airplane into one general pattern with several variations, the usefulness of a more complete flutter investigation of the airplane and components becomes apparent. It is at this point that the need for a facility to calculate the flutter characteristics in an expeditious manner is a necessity if the airplane design is to benefit from these calculations. The desk calculator, IBM, differential analyzer, and analog all have features that limit their usefulness. We have no experience with the high-speed digital computer; however, we are hoping that it will markedly reduce the number of limitations.

Recognizing the fact that engineering calculations start with significant simplifying assumptions, it then becomes a matter of choice of assumptions necessary to accomplish the task and selection of the best analytical procedure.

A flutter engineer's definition of an airplane is considerably different from that of other aeronautical engineers—namely, an infinite number of masses connected

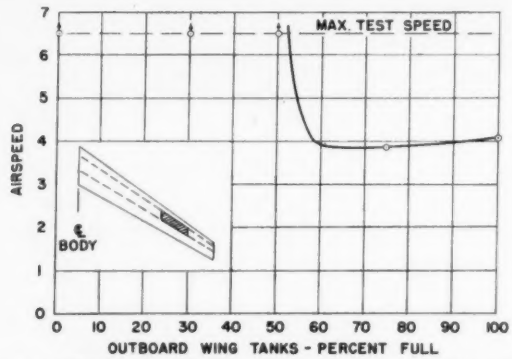

FIG. 1. Effect of fuel in outboard wing tanks on one flutter mode.

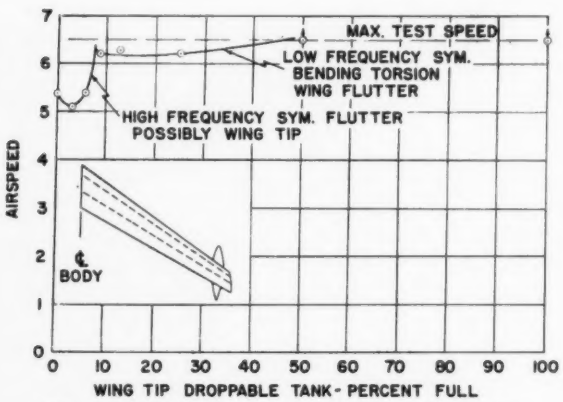

FIG. 2. Effect of fuel in tip tank for one configuration.

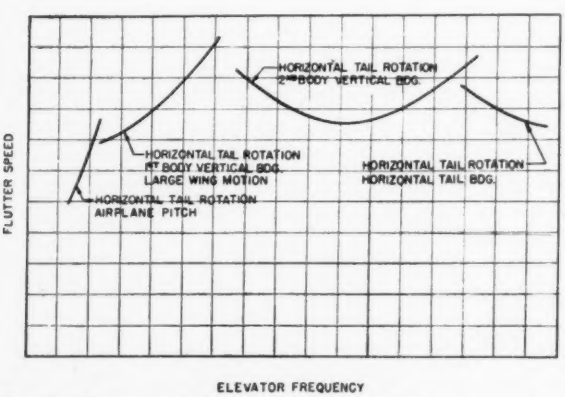

FIG. 3. Flutter variations as a function of elevator rotation frequency. (Flutter speed vs. elevator frequency.)

by springs and dampers in a geometrical pattern, each mass being subjected to aerodynamic, elastic, accelerating, and damping forces.

The necessary parameters for inclusions in the flutter analysis must be resolved from the drawings into numbers. Immediately the simplifying assumption of a finite number of masses (whether 5, 10, or 1,000) is necessary. This is done by arbitrarily selecting segments of the wing, fuselage, and empennage surfaces as the mass and aerodynamic area parameters. Since these segments are structural components of the airplane, they also comprise the elastic structure.

Determination of the mass characteristics of the segments requires skilled weight engineers to calculate the detail ingredients to the required accuracy. The elastic properties of the complex structure built up from thin sheet, stiffeners, multiple spars, etc., present a more difficult analysis problem. On the assumption that primary modes of the components are the important ones, it is possible to consider that the simple EI and JG stiffnesses are sufficient. Available information indicates that this may be oversimplification due to effects of shear lag, discontinuous structure, and redundancies. Rigorous analysis and consideration of higher order modes would require the inclusion of all of these. However, since these details are not available until well into the detail design stage of the airplane, it is necessary to proceed with the simpler stiffness data.

The next decision required is that regarding the aerodynamic terms. Cross-coupling of air forces between segments, tip effects, compressibility, and downwash on the horizontal tail surfaces all require consideration prior to determining both the method of making the flutter calculation and the facility to use.

Choice of Computing Facility

After reviewing the assumptions required to conduct either mathematical or experimental flutter analyses, it becomes apparent that there are several advantages in exploiting the mechanical analog or wind-tunnel flutter model. The model can include the same mass and elastic terms for all components as would be used in the mathematical calculations and, within the limitations of the test air velocity, all aerodynamic terms. The model makes flutter calculations so rapidly that numerous changes in configuration (six to 18 per test day) can easily be made. This makes it possible to determine rapidly the flutter sensitivity of many of the influential parameters.

At Boeing, we began our work on experimental low-speed wind-tunnel models several years ago, with the expectation of obtaining a check of the calculated flutter characteristics of an airplane. It appeared advisable to make the model include the same assumptions used in the flutter calculations, which included the rigid body freedoms; wing vertical bending and wing torsion stiffnesses; and infinite stiffnesses of the fuselage, empennage, and engine nacelle attaching struts. The calculations indicated that flutter would occur at 120 per cent design speed in an antisymmetrical mode. The model agreed that the flutter speed was approximately as predicted analytically; however, it fluttered in a symmetrical mode. This was one of the first indications that the analytical approach might have major deficiencies. There began the struggle to reduce the number of assumptions, refine the analyses, and include

additional aerodynamic elastic and mass terms as additional degrees of freedom.

Our models have become increasingly complex as we have gained more experience with the various items influencing flutter modes. We are finding that the number of test configurations required to satisfy even the minimum of possible couplings of parameters is continually increasing.

We initially tested the easiest changes, such as spanwise and chordwise location of wing-mounted concentrated weights and only one airplane weight that experience and intuition had said was the most critical. We are now testing 14 or more gross weight configurations involving various distributions of useful weight and variation in stiffness and stiffness ratio of the wings and nacelle struts, thus multiplying the number of tests.

The present models scale the elastic, mass, and geometric dimensions for horizontal and vertical tail surfaces, fuselage, wings, and nacelles and struts. We are not including movable control surfaces on our present models because of mechanical difficulties, as well as the questionable character of the low Reynolds Number of the small chord surfaces. Simulation of the jet stream of the engines has not been attempted; however, the gyroscopic effect of the engines has been included for some cases. Simulation of different altitudes has been made by incorporating the true scale of model-to-air-weight ratio and to obtain the proper load factor wing deflection scale.

Parameter Sensitivity

Some flutter modes have régimes of variation of parameters where extreme sensitivity is shown, and small changes result in large changes in flutter speed. This has been shown many times by the models. For example, a 20 per cent increase in wing torsional stiffness resulted in more than 100 per cent increase in flutter speed; 5 per cent reduction in outboard wing fuel raised flutter speed more than 100 per cent; 3 per cent reduction in fuel in external fuel tank reduced flutter speed by 20 per cent with a major change in mode. Figs. 1 and 2 show the abrupt change in flutter mode and speed for two variables. One mode was sensitive to relatively minor changes in model assembly, such as slight friction contact between the balsa wing sections and lead weights simulating fuel; small angles of yaw, 1° or less, of the external fuel tank; change from a small tubular weight to a streamlined tank; or the addition of a small amount of liquid fuel in the tank. An investigation of the influence of rotational frequency of an all movable horizontal tail surface resulted in wide changes of mode shape. Fig. 3 shows this variation. Investigations of the nacelle strut stiffness have shown this to be a significant variable.

Significant changes in wing flutter also have occurred with variations in fuel weight distribution in the fuselage.

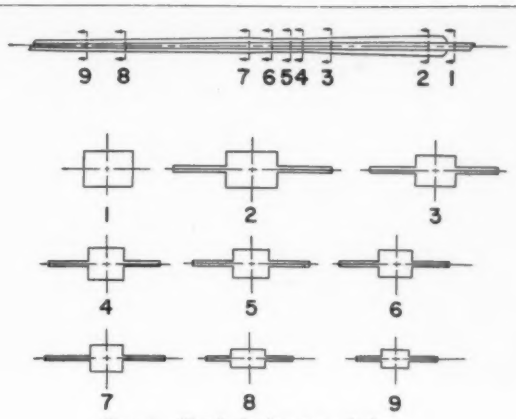

Fig. 4. Typical wing spar design.

One interesting and significant result to which we had not previously given sufficient importance was experienced during a series of tests of identical configurations on models scaled for simulation of two different altitudes. Flutter curves at one altitude were shifted a considerable amount from the curves obtained at the other altitude for one series of parameter changes. Where one flutter mode had been the critical one, another mode became critical at a lower speed for the second altitude. In addition to the significance of the air density change, the problem of being sure that all of the necessary parameter variations had been investigated is highlighted by these results.

Model Wing Design

The above phenomena have been experienced over a period of several years and the testing of a number of models, and they appreciably influenced the details of our model construction. A good example of this was the development of our wing design. The first model wing was conceived as the simplest possible structure. The choice of scale parameters, geometry to be as large as possible for ease of manufacture and speed scale to permit simulation of the maximum airplane speed within the speed range of available tunnels, resulted in a mass and stiffness scale that permitted the simple wing design. Tests showed that a wing of solid balsa could, with suitable spanwise and chordwise slots, be made to scale the wing vertical bending and torsional stiffnesses. It was assumed that scaling the fore-and-aft stiffness was not necessary. We were fortunate that, by trial-and-error slotting, the first set of wings easily achieved the proper stiffness. Subsequent wings were more difficult. After it appeared that we would be expending more effort in experimental model testing, we decided to develop the structural design so that the proper stiffnesses would be predicted rather than rely on trial-and-error procedure. A spar of rectangular cross section, tapered spanwise as necessary and with flanges to control stiffness in that plane, was selected and resulted in excellent accuracy in

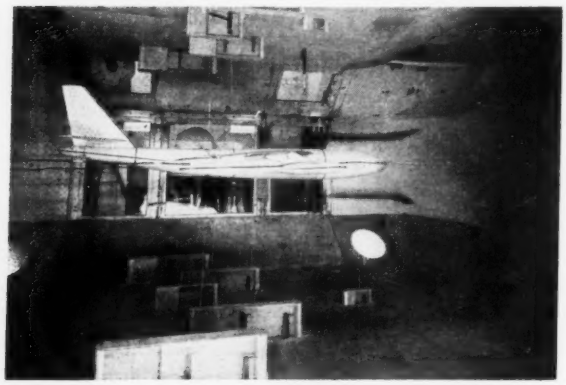

FIG. 5. Side view of initial soft spring support.

stiffness and stiffness distribution, as seen in Fig. 4. The flutter modes of the first model with this wing design involved large fore-and-aft displacements of the wing tip. Review of the stiffness data for the model and airplane uncoverd an oversight in computation of the fore-and-aft wing stiffness which had resulted in extra flexibility for the model. Correction of this deficiency raised the flutter speed approximately 20 per cent and reduced the fore-and-aft deflection to a small magnitude.

Consideration of the significance of the fore-and-aft stiffness leads logically to the recognition that the static vertical bending deflection is also important flutterwise because of the coupling of fore-and-aft wing bending with wing torsion. The additional aerodynamic coefficients of the fore-and-aft movement can also be effective. To obtain the scaled wing deflection, the static aerodynamic span load distribution must be scaled unless preformed spars are used. It also follows that, if the aerodynamic coefficients are nonlinear, the wing must be operating at the same C_L as the full-scale airplane.

We have been flying the models at unit load factor and in most cases designing for true scale deflection. If it is desired to investigate other than unit load factor wing deflection, then additional wing spar stiffnesses are required for simulating stiffness changes due to skin wrinkling or to obtain the desired deflection curve unless some loading provision that will not interfere with the flutter mode is used.

Model Support

The support of the dynamically and elastically scaled model is a major problem in a successful wind-tunnel flutter model program. Our suspension systems have varied considerably in attempting to achieve the desired boundary conditions. Provision for the rigid body motions for symmetrical or antisymmetrical simulations, ensurance that the flutter modes are influenced as little as possible by the supporting means, prevention of low-frequency unstable oscillations of the model, and safety provisions to prevent destruction of the model in case of flutter are some of the design requirements.

Our first support installation was chosen after reviewing the available information of flutter model testing by others and was patterned on the spring suspension used by Junkers in Germany. Fig. 5 shows this installation. The model was supported on music wire attached to soft cantilever springs at the floor and ceiling. Multiple wires attached to the wing and fuselage leading to a manual pull-down, which pulled the wires taut to restrain the model firmly. A single drag wire was attached to the nose of the fuselage. Two antidrag wires diagonally aft to each side and attached to the tunnel wall by soft springs positioned the model laterally. This resulted in elastic restraint in all rigid body rotations and translations, except fore and aft which was rigid. The fish net stretched across the tunnel was to catch the broken pieces of the model as it disintegrated during flutter. The first test run on this installation introduced us to one of the most troublesome problems of complete model testing—that of instability in pitch and vertical translation. Several trial-and-error changes were required before it became apparent that, even though the vertical restraining springs were

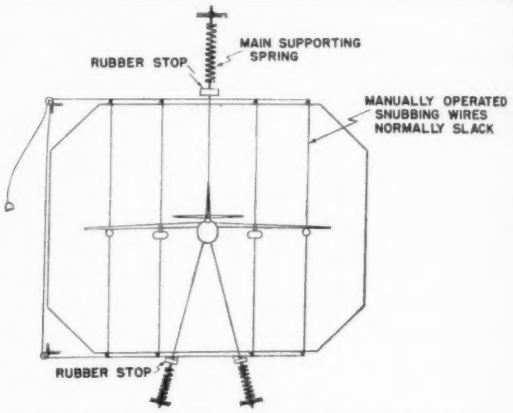

FIG. 6. Front view of initial soft spring support.

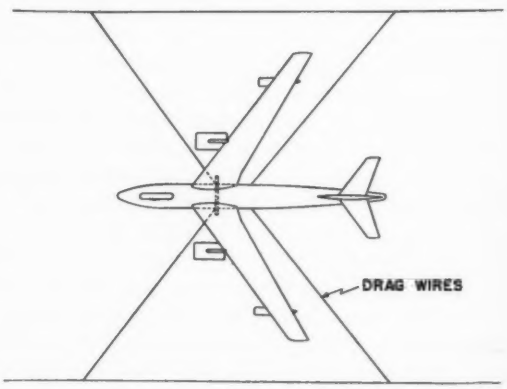

FIG. 7. Plan view of initial soft spring support.

extremely soft, their fore-and-aft location with respect to the airplane center of gravity was important. Having the elastic center behind the c.g. is beneficial. Figs. 6 and 7 are sketches of the most successful arrangement. Rigidity in side translation provided by the cross drag bracing was used to help control Dutch-roll instability.

A second approach was to design independent supports for symmetrical and antisymmetrical testing. Fig. 8 is a side view of the symmetrical installation with the model attached to the end of a rigid strut which was free to travel vertically on four roller bearings. The model was free to pitch on a bearing at the strut attachment located at the model c.g. Provision for large vertical displacement of the model approximately 40 in. was incorporated on the premise that the model instability difficulties were primarily due to the limited displacement and the nonlinear galloping of the model off the snubbers. In addition, a hydraulic shock absorber was designed for limiting vertical translation and bounce-off. In spite of these precautions, considerable difficulty was experienced with instability at high air speeds for many of the test configurations.

The extra weight of the strut was a disadvantage in that it was impossible for the lighter gross weights to be scaled for true weight distributions. Fig. 9 is a photo of the strut and upper bearing support. Fig. 10 shows the attachment of the strut to the fuselage spar and pitch bearing.

Fig. 11 is a side view of the antisymmetrical support providing fixity in drag and vertical translation, freedom in pitch and yaw, and elastic restraint in roll and side translation. Instability in roll and side translation made it necessary to restrain elastically the model in side translation to obtain a favorable frequency ratio. Positioning of the model in roll was accomplished by a remotely operated electric motor rotating a torque tube attached to the trunnion and fuselage spar. Fig. 12 gives additional details of this installation.

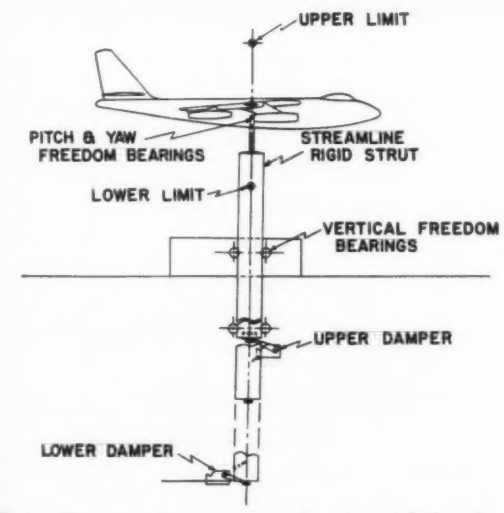

FIG. 8. Side view of strut support for symmetrical modes.

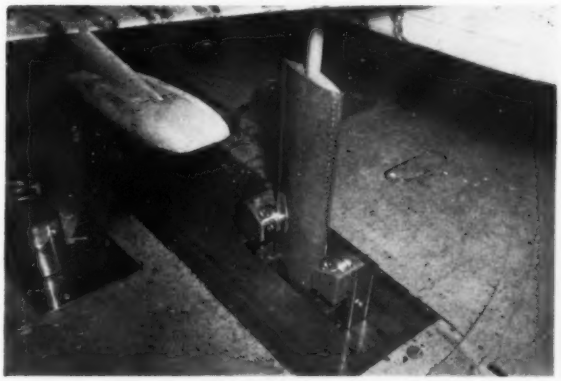

FIG. 9. Detail of strut and bearing support.

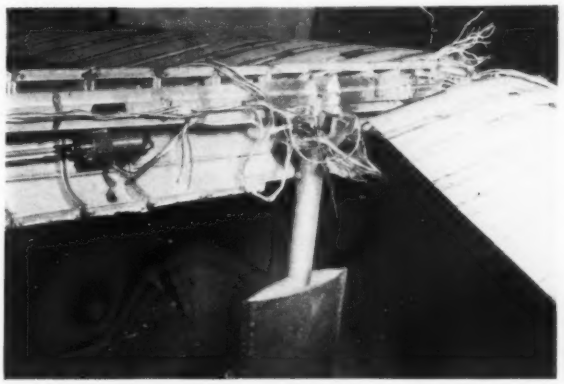

FIG. 10. Detail of model—strut attachment.

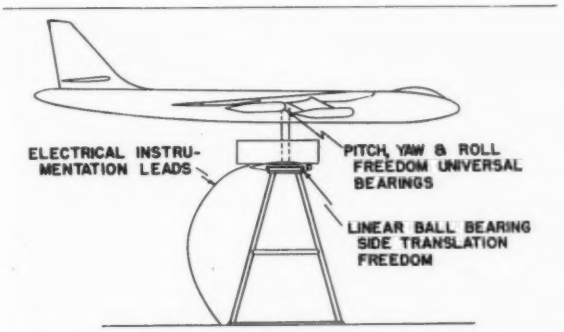
ELECTRICAL INSTRUMENTATION LEADS
PITCH, YAW & ROLL FREEDOM UNIVERSAL BEARINGS
LINEAR BALL BEARING SIDE TRANSLATION FREEDOM

FIG. 11. Side view of side translation mount for antisymmetrical modes.

One test result not anticipated was the sensitivity of the antisymmetrical flutter mode to the fore-and-aft position of the trunnion attachment on the body spar; moving from 10 to 18 per cent M.A.C. raised the flutter speed by 110 per cent.

A major fault in the use of two independent installations for symmetrical and antisymmetrical investigations considerably devaluates their usefulness. The

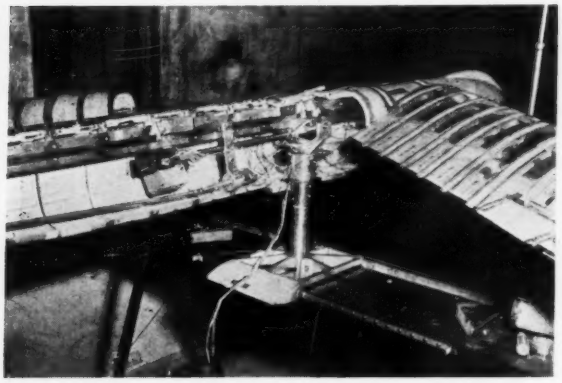

FIG. 12. Details of side translation mount.

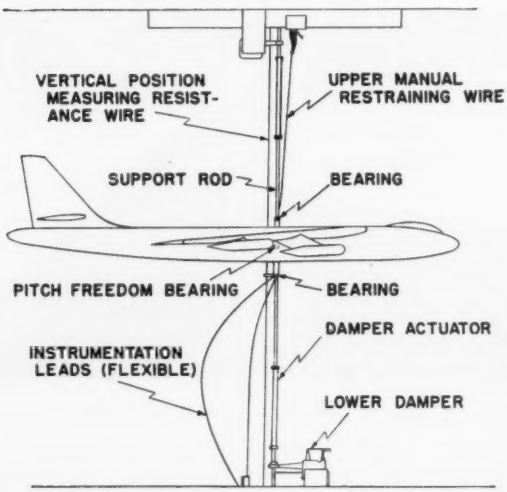

FIG. 13. Side view of vertical rod installation.

artificial locking of the rigid body motions change the flutter characteristics of the model for the condition not being studied. For example, many cases of symmetrical flutter occurred with the model mounted on the antisymmetrical mount at speeds considerably lower than the required maximum speed.

The flutter model suspension system now being used for our testing has improved features. Fig. 13 is a schematic side view of the vertical rod installation.

A $^1/_4$-in. diameter rod, ground to uniform diameter and hard-chrome plated, is installed under controlled tension. A short trunnion sliding on the rod and attached to the fuselage spar through a pitch bearing located at the model center of gravity provides all of the rigid body degrees of freedom; zero frequencies in vertical translation, pitch and yaw; elastic restrain provided by the rod, in roll and lateral and fore-and-aft translation at approximately one-half the frequency of the lowest antisymmetrical mode. The shock absorbers at the limits of travel on the rod are secondary safety stops on this installation. The flexible cables attached to the trunnion above and below the model lead outside the tunnel to a servomechanism to suppress the vertical translation-pitch instability. A low-frequency pass filter reduces the effect of the cable restraint, although the cables are slack except when needed as controlled by the intelligence of the mechanism. Our automatic damper is a skilled, dexterous, and hard-working engineer holding the ends of the cables. Oscillograph records of his force-time-displacement show good 90° phase. The design of an electromechanical servomechanism is on our list of work to be done, since our present models sometimes demand the maximum of frequency and force response from our human servomechanism.

Locks for stopping the flutter to prevent damage to the model are not used. It has been found that the models are sufficiently rugged to withstand the majority of the flutter cases. Numerous minor failures have occurred during the developmental period; however, only one major failure has resulted from flutter. A high-frequency flutter mode of the horizontal tail surface failed an underdesigned spar fitting, causing loss of the whole surface. The resultant divergence of the model failed the wings. The time for failure was so short that the operation of any safety system would have been improbable.

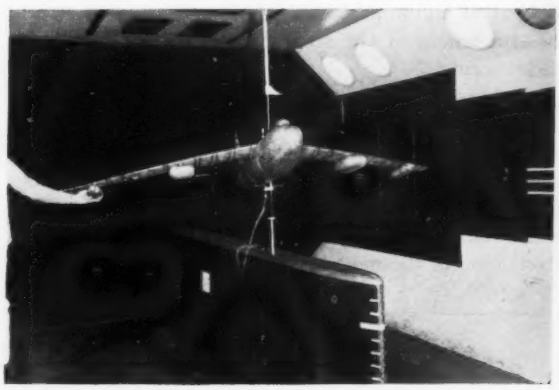

FIG. 14. Vertical rod installation.

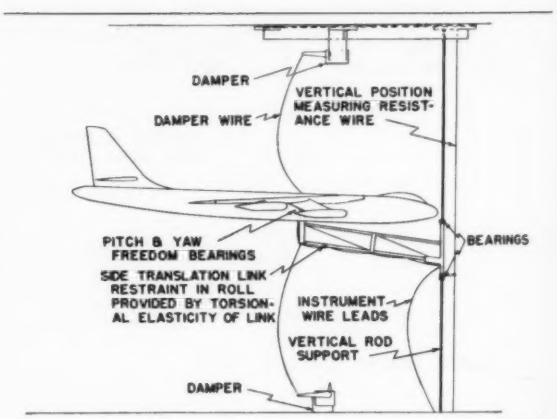

FIG. 15. Combination installation of vertical rod and link.

Fig. 14 shows the tunnel installation. The faired island below the model surrounds fixed instrumentation in the tunnel not associated with the flutter testing.

An attempt was made to remove the side translation elastic restraint and to reduce the roll spring rate by the installation shown in Fig. 15. This was a combination of the vertical rod support and a pinended link. Dutch roll occurred at extremely low speeds and could not be eliminated by reasonable measures. This system was quickly abandoned.

Model Construction

The details of the model construction have developed in the same manner as the model supports. The solid balsa structure of Fig. 16 has changed to hollow boxes covered with balsa and silkspan tissue paper. Fig. 17 is one design of a wing segment. The single point attachment at the spar prevents the stiff box from affecting the spar stiffness. The slots between segments

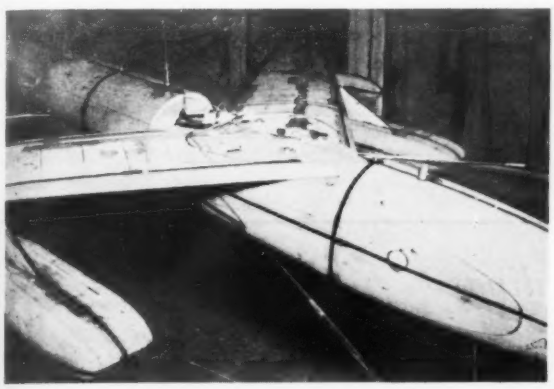

Fig. 16. Solid balsa wing and fuselage.

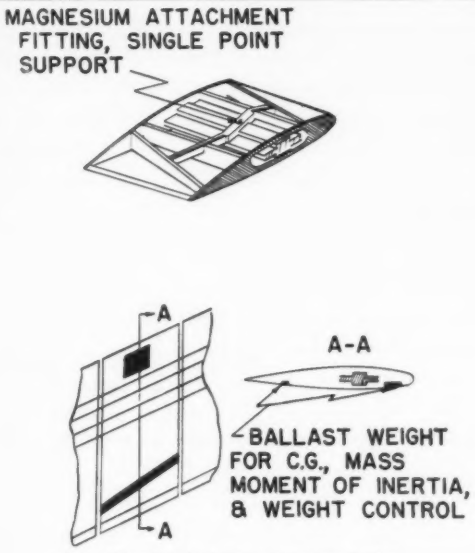

Fig. 17. Typical wing segment design.

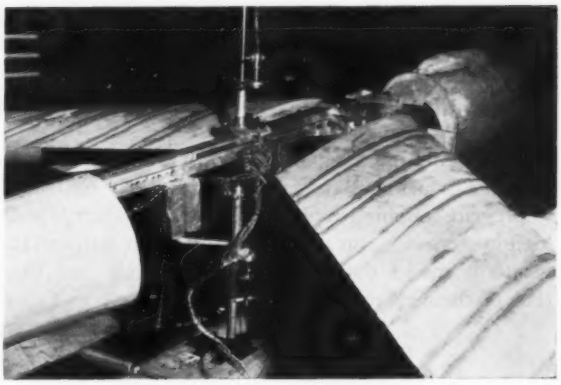

Fig. 18. Model details.

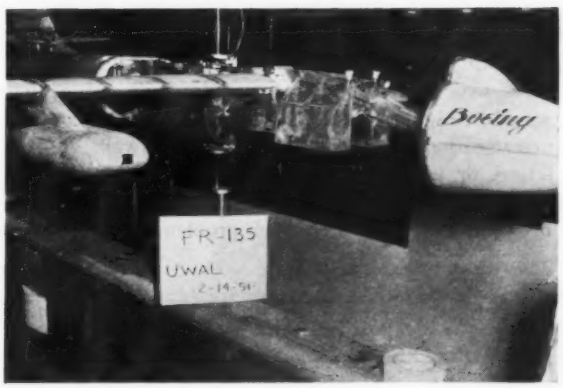

Fig. 19. Model details of plastic liquid-containing tanks.

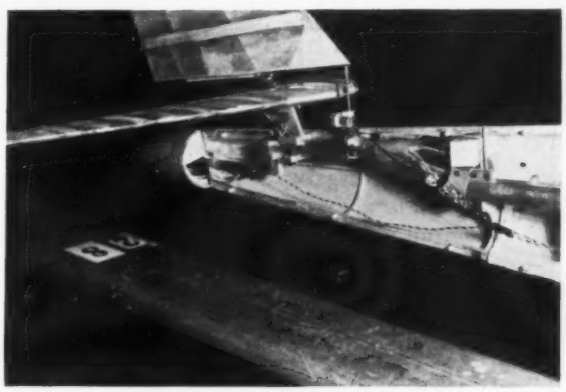

Fig 20. Empennage assembly.

are covered with thin rubber strips cemented on the final assembly. Control of weight, center of gravity, and pitch moment of inertia per segment is achieved by actual weighing, balancing, and swinging on a bifilar pendulum, then adding the necessary ballast weights.

In Fig. 18, part of the fuselage shell has been removed, revealing instrumentation leads, fuselage spar, and trunnion details. Fig. 19 shows liquid-containing tanks for fuel simulation; Fig. 20, the empennage.

The small electric motor, worm and gear, and screw attached to the leading edge of the stabilizer and fuselages spar raises or lowers the stabilizer angle for flying the model in the tunnel. Aileron and rudder control has not been necessary.

Since structural damping can be an important parameter, the model construction must be closely controlled to prevent rubbing friction or the use of materials with high hysteresis. Our design is easily controlled, and the resultant model damping is conservatively less than that of the airplane.

Future Development

Continued development of experimental flutter analysis is required along several lines. The use of a variable density wind tunnel to investigate further the influence of altitude on flutter modes is needed. Flutter testing of a complete scaled model at a one-to-one speed scale further to reduce aerodynamic assumptions would be highly beneficial. It is necessary to continue investigation of the influence of tunnel walls on oscillating air forces. The simulation of the elastic properties of the full-scale wings, especially the lower aspect ratios, is a good research problem.

A major gap exists in the knowledge of how well the models or mathematical analyses simulate the full-scale airplane flutter characteristics. Full-scale flight-flutter testing of a number of configurations, which have been previously investigated in the wind tunnel, would be necessary to provide the minimum information. It should be emphasized that negative flight results would not serve this purpose. Testing techniques and safety measures would have to be developed to permit obtaining the required information with a near approach to flutter.

Conclusions

Experience has shown that flutter analysis by use of the mechanical analog or wind-tunnel flutter model is an expeditious means for investigating the flutter characteristics of a complex airplane.

Continued effort to develop this technique and to reduce the number of significant assumptions of elastic simulation, aerodynamic compressibility, and tunnel-wall effects will be well worth while. Correlation of flutter analyses and full-scale flight-flutter investigations is necessary to assist in improving the accuracy of flutter predictions.

Proceedings

Third Anglo-American Aeronautical Conference

Now Available

Proceedings of the Joint Conference between the Royal Aeronautical Society and the Institute, held in Brighton last September, are now ready for distribution in England. These volumes contain all of the full-length papers and discussions presented at the Conference. Only a limited supply is available for distribution.

Order Direct from

The Royal Aeronautical Society

4 Hamilton Place — London, W. 1, England

Send remittance with order:
£5.5.0 ($14.70), postage prepaid.

(10% U.S. Customs Duty
Payable upon Receipt.)

Analysis of Oval Rings by Fourier Series*

ROLAND J. BENJAMIN†
University of Illinois

SUMMARY

The distinguishing feature of this method of analysis of thin oval rings is the representation of the shape of the ring by the use of Fourier series. By means of standard computational schemes, the coefficients of Fourier series of sine and/or cosine terms may be so selected as to cause the graph of the function represented by the series to approximate closely the shape of the ring under consideration.

Once the ring has thus been represented by an analytical expression, any of the common strain energy methods may be employed in the solution of the problem. Because of its simplicity, the method of elastic weights is used herein, and a sample problem of a general oval ring subjected to concentrated loads is worked out.

The possibilities of application of the method to fuselage ring design are pointed out by the solution of the problem of an elliptical ring subjected to a concentrated load and held in equilibrium by distributed skin forces.

The accuracy of the method, established by analyzing true elliptical rings whose solutions are already known, is high. To reduce computation, some of the higher harmonics of the Fourier series may be neglected with but negligible effect upon the result.

The method is general and may be applied to rings having two, one, or no axes of symmetry.

INTRODUCTION

THE PROBLEM OF ANALYSIS of a thin closed ring occurs frequently in the design of aeronautical structures. For rings of circular or elliptical shapes, numerous solutions are available in the literature.[1–5] The more general case of rings with but one axis of symmetry has been treated by several writers[6–8] in broad terms, but in the applications of the proposed methods of solution to specific rings (other than circular) difficulties are encountered in attempting to evaluate the integrals required. For such rings some method of graphical integration must usually be employed.

The method of solution proposed in this paper avoids such procedures and permits solution of the problem on an analytical basis. It is applicable to rings having two, one, or no axes of symmetry. However, the case of complete lack of symmetry is of little importance, since the rings encountered in aircraft design, particularly fuselage rings, normally have at least one axis of symmetry.

Received March 17, 1952.

* From an M.S. thesis in the Department of Theoretical and Applied Mechanics, University of Illinois. Special acknowledgment is due to Prof. H. L. Langhaar, of the University of Illinois, for suggesting this problem to the author and for his helpful comments and criticism in the preparation of this paper.

† University Fellow in Theoretical and Applied Mechanics.

The basic step in this method is the analytical expression of the coordinates of a point on the ring by means of Fourier series.

DETERMINATION OF FOURIER SERIES

Let us now consider the ring shown in Fig. 1. To locate points on the ring, the vertical axis of symmetry is chosen as the y-axis. The x-axis may be taken through any convenient point; in this case it is midway between the extreme ends of the ring.

It is desired to express the coordinates (x, y) of any point on the ring in terms of the parameter s, where s is the distance along the curve measured clockwise from the top of the ring. In order to obtain simple periodic functions, it is convenient to replace s by the parameter θ defined as

$$\theta = \pi s/c \tag{1}$$

where c is the semicircumference of the ring. Thus, as the ring is traversed from the uppermost point in the clockwise direction, s increases from zero to $2c$ and θ increases from zero to 2π. It should be pointed out that θ is merely the quantity defined by Eq. (1) and is not the measure of any geometric angle.

We wish to find expressions for x and y as functions of θ in the form of Fourier series. In the computational

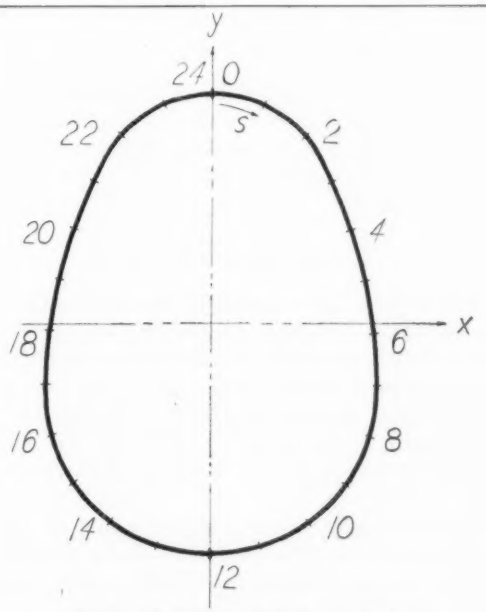

FIG. 1. Oval ring for Fourier analysis.

TABLE 1
Coordinates of Points on Ring of Fig. 1

Point	s	x	y
0	0	0	10.00
1	$c/12$	2.20	9.52
2	$c/6$	4.01	8.17
3	$c/4$	5.25	6.27
4	$c/3$	6.20	4.20
5	$5c/12$	6.83	1.99
6	$c/2$	7.16	−0.28
7	$7c/12$	7.14	−2.56
8	$2c/3$	6.80	−4.83
9	$3c/4$	5.83	−6.90
10	$5c/6$	4.25	−8.54
11	$11c/12$	2.24	−9.61
12	c	0	−10.00
13	$13c/12$	−2.24	−9.61
14	$7c/6$	−4.25	−8.54
15	$5c/4$	−5.83	−6.90
16	$4c/3$	−6.80	−4.83
17	$17c/12$	−7.14	−2.56
18	$3c/2$	−7.16	−0.28
19	$19c/12$	−6.83	1.99
20	$5c/3$	−6.20	4.20
21	$7c/4$	−5.25	6.27
22	$11c/6$	−4.01	8.17
23	$23c/12$	−2.20	9.52
24	$2c$	0	10.00

scheme to be used, the coordinates of equally spaced points around the ring are required; it is particularly convenient to use 24 such points. These values, as well as the value of c, may easily be determined from a drawing of the ring with the aid of dividers. The values of x, y, and s for the various points are tabulated in Table 1. The value of c was found to be 27.46.

Evidently x is an odd function of θ and y is an even function of θ. Hence, x may be represented by a sine series and y by a cosine series. Following the method of Fourier analysis described by Den Hartog[9] and using the values in Table 1, we get

$$x = (1/12)(9.06 \sin\theta - 2.97 \sin 2\theta + 4.40 \sin 3\theta + 1.09 \sin 4\theta + 0.22 \sin 5\theta + 0.46 \sin 6\theta + 0.10 \sin 7\theta - 0.15 \sin 8\theta + 0.04 \sin 9\theta - 0.05 \sin 10\theta - 0.14 \sin 11\theta) \quad (2)$$

$$y = (1/12)(-2.57 + 115.91 \cos\theta + 1.65 \cos 2\theta + 3.94 \cos 3\theta + 1.04 \cos 4\theta + 0.17 \cos 5\theta + 0.04 \cos 6\theta + 0.01 \cos 7\theta - 0.16 \cos 8\theta - 0.06 \cos 9\theta - 0.01 \cos 10\theta - 0.03 \cos 11\theta + 0.01 \cos 12\theta) \quad (3)$$

APPLICATION TO OVAL RING

Since we now have expressions representing the shape of an arbitrarily chosen oval ring, we may proceed to find the bending moment at any section of the ring due to the action of applied loads. As an example, let the ring be loaded as shown by Fig. 2a. The vertical forces $P/2$ located at the points $s = 2c/3$ and $s = 4c/3$ are resisted by the single force P acting at the top of the ring.

Any convenient strain energy method of analysis may be followed. The method of elastic weights[6] will be used in the illustrative examples; the "dummy-load" method has been used with equal ease. In either case it is assumed that Hooke's Law is valid and that the strain energy due to axial and shear forces is negligible as compared with that due to bending.

Since both the ring and its loading are symmetrical about the vertical centerline, the ring may be assumed to be cut at the top and bottom and only one-half of it need be considered, as in Fig. 2b.

In applying the method of elastic weights the ring is assumed rigidly fixed at the top section. Instead of applying the indeterminate moment and forces directly to the cut section at a, they are assumed to be acting at the end of a rigid arm L rigidly attached to the ring.

An elastic weight dw is defined by

$$dw = ds/EI \quad (4)$$

where ds is a differential length of the ring. E and I have their usual meaning and are here considered to be constant throughout the ring.

The length of the fictitious arm L is such that its free end will fall on the origin of coordinates. This origin must be located at the "center of gravity of the elastic weights" of the complete ring such that

$$\int x\,dw = \int xy\,dw = \int y\,dw = 0$$

or, if EI is constant,

$$\int x\,ds = \int xy\,ds = \int y\,ds = 0 \quad (5)$$

Since the ring is symmetrical about the y-axis, the first two conditions of Eq. (5) are automatically satisfied. To satisfy the third condition, the vertical location of the origin, which was arbitrarily chosen to carry out the Fourier analysis, must be changed. Let us denote by y' the ordinate of a point referred to the present axis and by y the ordinate of the same point referred to the axis through the c.g. of the elastic weights.

Considering the present axis,

$$\int_0^c y'\,ds = c\bar{y} \quad (6)$$

where c is the semicircumference of the ring and $\bar{y}$ is

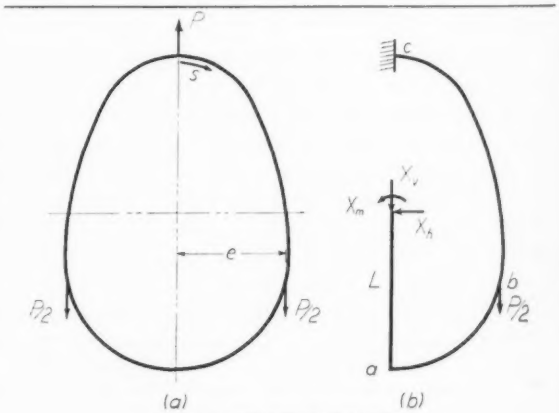

FIG. 2. Problem of oval ring.

the ordinate of the c.g. of the elastic weights. If $\bar{y}$ is now found and the origin translated to the point $(0, \bar{y})$, the condition prescribed for the use of the elastic weight method will have been fulfilled.

The expression for the quantity now denoted by y' is given by Eq. (3) in terms of θ. Recalling that $\theta = \pi s/c$, we have

$$d\theta = \frac{\pi ds}{c} \quad \text{or} \quad ds = \frac{c}{\pi} d\theta$$

Then the integral of Eq. (6) becomes

$$\int_0^c y' \, ds = \frac{c}{\pi} \int_0^\pi y' \, d\theta$$

This may easily be evaluated by term-by-term integration of Eq. (3), giving

$$\frac{c}{\pi} \int_0^\pi y' \, d\theta = \frac{c}{12} (-2.57) = c\bar{y}$$

Thus,

$$\bar{y} = -(2.57/12)$$

and the origin must be transferred to the point $(0, -2.57/12)$. The effect of this transfer is to eliminate the constant in the expression for y', and there results

$$\begin{aligned} y = (1/12)(&115.91 \cos\theta + 1.65 \cos 2\theta + 3.94 \cos 3\theta + \\ &1.04 \cos 4\theta + 0.17 \cos 5\theta + 0.04 \cos 6\theta + \\ &0.01 \cos 7\theta - 0.16 \cos 8\theta - 0.06 \cos 9\theta - \\ &0.01 \cos 10\theta - 0.03 \cos 11\theta + 0.01 \cos 12\theta) \end{aligned} \qquad (7)$$

We see that the location of the axis through the c.g. of the elastic weights is particularly simple when the Fourier series method is used. First, the series expression for y' is found referred to any convenient horizontal axis. Then, by merely dropping the initial constant, the expression for y referred to the axis through the c.g. of the elastic weights is obtained.

We have now satisfied the conditions required for the use of the elastic weight method. Returning to Fig. 2b, let X_m, X_h, and X_v denote the indeterminate moment, horizontal force, and vertical force, respectively, assumed to be acting at the end of the rigid arm L. These quantities are taken as positive in the directions indicated.

At any point $P(x, y)$ of the ring, the bending moment M is given by

$$M = M_0 + X_m + X_v x + X_h y \qquad (8)$$

where M_0 is the moment that would exist because of the external loads on the ring if X_m, X_v, and X_h were all zero. It may be shown that

$$\begin{aligned} X_m &= -\frac{\int M_0 \, ds}{\int ds}, \qquad X_v = -\frac{\int M_0 x \, ds}{\int x^2 \, ds} \\ X_h &= -\int M_0 y \, ds / \int y^2 \, ds \end{aligned} \qquad (9)$$

These are the basic equations of the elastic weight method. When M_0 is not symmetrical about the vertical axis, the integrations must be carried out completely around the ring. If, as in the present case, there is vertical symmetry of M_0, the integrations need be carried out over but one-half of the ring, and X_v will always be found to be zero.

Solution of Sample Problem

For the problem of Fig. 2b, we define M_0' as the value of M_0 at any section between a and b and M_0'' as the value of M_0 at any section between b and c. Thus,

$$M_0' = 0, \qquad M_0'' = (P/2)(x - e)$$

where e is the x-coordinate of the point of application of the load and is found to be 6.80.

Now

$$X_m = -\int_c^0 M_0 \, ds / \int_c^0 ds = \int_c^0 M_0 \, ds/c$$

where

$$\begin{aligned} \int_c^0 M_0 \, ds &= \int_c^{2c/3} M_0' \, ds + \int_{2c/3}^0 M_0'' \, ds \\ &= \frac{Pc}{2\pi} \int_{2\pi/3}^0 x \, d\theta - \frac{Pe}{2} \int_{2c/3}^0 ds \end{aligned}$$

Integrating each of these terms separately

$$\frac{Pc}{2\pi} \int_{2\pi/3}^0 x \, d\theta = -1.75Pc$$

by term-by-term integration of Eq. (2), and

$$-\frac{Pe}{2} \int_{2c/3}^0 ds = \frac{2Pec}{6} = \frac{2P(6.80)c}{6} = 2.27Pc$$

Then,

$$X_m = (-1.75 + 2.27)Pc/c = 0.52P$$

Because of symmetry, $X_v = 0$.

Determination of X_h

$$X_h = -\int_c^0 M_0 y \, ds / \int_c^0 y^2 \, ds$$

$$\begin{aligned} \int_c^0 M_0 y \, ds &= \int_c^{2c/3} M_0' y \, ds + \int_{2c/3}^0 M_0'' y \, ds \\ &= \frac{Pc}{2\pi} \int_{2\pi/3}^0 xy \, d\theta - \frac{Pec}{2\pi} \int_{2\pi/3}^0 y \, d\theta \end{aligned}$$

The product xy, in which x and y are represented by series expressions, requires investigation. Since

$$\left.\begin{aligned} y &= a_1 \cos\theta + a_2 \cos 2\theta + \ldots + a_{12} \cos 12\theta \\ x &= b_1 \sin\theta + b_2 \sin 2\theta + \ldots + b_{11} \sin 11\theta \end{aligned}\right\} \qquad (10)$$

obviously the product will be of the form

$$xy = \sum_{m=1}^{12} \sum_{n=1}^{11} a_m \cos m\theta \cdot b_n \sin n\theta$$

We now recall the trigonometric identity

$$\cos m\theta \cdot \sin n\theta = (1/2)[\sin(n+m)\theta + \sin(n-m)\theta]$$

Using this identity and neglecting harmonics higher than those originally present, we obtain

$$xy = (1/2)(K_1 \sin\theta + K_2 \sin 2\theta + \ldots + K_{12} \sin 12\theta) \quad (11)$$

The values of the constants K_i in the above expression are functions of the coefficients of Eq. (10) and are given by

$$K_i = \sum_{j=1}^{12} a_j(b_{i-j} + b_{i+j}) \qquad (i = 1, 2, 3, \ldots, 12)$$

subject to the definitions $b_{-n} = -b_n$, $b_0 = 0$, and $b_n = 0$ for $n > 12$. For example,

$$K_1 = a_1(0 + b_2) + a_2(-b_1 + b_3) + a_3(-b_1 + b_5) + a_4(-b_2 + b_6) + \ldots + a_{12}(-b_{11} + 0)$$

$$K_2 = a_1(b_1 + b_3) + a_2(0 + b_4) + a_3(-b_1 + b_5) + a_4(-b_2 + b_6) + \ldots + a_{12}(-b_{10} + 0)$$

etc. Eq. (11) for xy may easily be integrated, giving

$$\int_{2\pi/3}^{0} xy\, d\theta = -\frac{3}{4}(K_1 + K_2 + K_4 + K_5 + K_7 + K_8 + K_{10} + K_{11})$$

where K_3, K_6, K_9, and K_{12} have dropped out. Thus these constants need not be computed. Using the Fourier coefficients previously determined for this ring, the above expression may be evaluated.

$$\frac{Pc}{2\pi}\int_{2\pi/3}^{0} xy\, d\theta = -\frac{3Pc}{8\pi}(78.63) = -9.39Pc$$

The term

$$\int_{2\pi/3}^{0} y\, d\theta$$

presents no difficulties; term-by-term integration of Eq. (7) may be used, giving

$$-\frac{Pec}{2\pi}\int_{2\pi/3}^{0} y\, d\theta = 9.00Pc$$

Thus,

$$\int_c^0 M_0 y\, ds = -0.39Pc$$

The denominator of the expression for X_h is

$$\int_c^0 y^2\, ds = \frac{c}{\pi}\int_\pi^0 y^2\, d\theta$$

Now

$$\frac{c}{\pi}\int_\pi^0 y^2\, d\theta = \frac{c}{\pi}\int_\pi^0 \left(\sum_{m=1}^{12}\sum_{n=1}^{12} a_m \cos m\theta \cdot a_n \cos n\theta\right) d\theta$$

For m unequal to n the value of this integral is zero. For m equal to n,

$$\frac{c}{\pi}\int_\pi^0 y^2\, d\theta = \frac{c}{\pi}\int_\pi^0 \sum_{n=1}^{12} a_n^2 \cos^2 n\theta\, d\theta = \frac{c}{2}\sum_{n=1}^{12} a_n^2$$

Substituting values of a_n from Eq. (7),

$$\int_c^0 y^2\, ds = -47.06c$$

Therefore,

$$X_h = -(-0.39Pc/-47.06c) = -P/121$$

The final expressions for the bending moment are: from a to b,

$$M = P[0.52 - (y/121)]$$

from b to c,

$$M = P[(x/2) - (y/121) - 2.88]$$

The normal and shear forces at any section may be found in terms of P and X_h by the usual methods, taking into account the angle the section makes with the horizontal.

By substituting appropriate values for the Fourier coefficients a_n and b_n, this solution may be applied to any ring with one axis of symmetry loaded as indicated in Fig. 2a, regardless of size or shape. The values to be used would, of course, be found from a Fourier analysis of the particular ring.

Accuracy of the Method

As a check on its accuracy this method was applied to a true elliptical ring subjected to various conditions of loading. The solution of such rings has previously been worked out by Burke[1] through the use of elliptic integrals. The comparison of the results of the two methods of analysis for two specific loadings chosen at random is given by Table 2. It will be noted that the differences between the results of the two methods are small. There is no convenient way to check the accuracy of the Fourier series method for nonelliptical rings, but the close agreement with Burke's method for elliptical rings indicates that the accuracy should be high.

Also in Table 2 is illustrated the effect of using a reduced number of terms in the series. The extremely small magnitudes of the coefficients of the higher harmonics suggested the idea of dropping them entirely. For the true ellipse, the complete series contained only six terms because of the presence of both horizontal and vertical symmetry. When the last four terms of each series were dropped off, the effect upon the results was negligible. However, the computational effort required was greatly reduced, particularly when one series was to be multiplied by the other.

TABLE 2
Comparison of Results of Different Analyses of Elliptical Rings (Major Axis Assumed Vertical)

Method of Analysis \ Type of Loading	Vertical Forces: P Upward at $s = 0$ P Downward at $s = c$ (Ends of Major Axis) No Horizontal Forces	Vertical forces: P Upward at $s = 0$ $P/2$ Downward at $s = 3c/4$ $P/2$ Downward at $s = 5c/4$ Horizontal Forces: Q to the right at $s = c/3$ Q to the left at $s = 5c/3$
Method of Burke (elliptic integrals)	$X_h = X_v = 0$ $X_m = -1.76P$	$X_v = 0$ $X_h = 0.046P + 0.76Q$ $X_m = -(5.16Q + 1.97P)$
Fourier series, six terms	$X_h = X_v = 0$ $X_m = -1.77P$	$X_v = 0$ $X_h = 0.046P + 0.76Q$ $X_m = -(5.18Q + 1.98P)$
Fourier series, two terms	$X_h = X_v = 0$ $X_m = -1.76P$	$X_v = 0$ $X_h = 0.047P + 0.76Q$ $X_m = -(5.18Q + 1.98P)$

APPLICATION TO FUSELAGE RING

In airplane structures the loads applied to a fuselage ring are not resisted by concentrated forces as in the preceding example problem. Instead, the ring is held in equilibrium under load by the combined action of a series of concentrated forces supplied by the stringers plus a distributed reaction due to shearing forces set up in the skin. To simplify the analysis, the assumption is often made that the effect of the stringers may be accounted for by assuming an effective skin thickness greater than the actual thickness. This approximation will be used here.

EXAMPLE

The problem is illustrated by Fig. 3a. For simplicity, an elliptical ring is used rather than a general oval ring, although the procedure is identical in both cases.

The concentrated load P acting on the elliptical ring is opposed by shearing forces in the skin of effective thickness t. These shearing forces are a result of the longitudinal bending of the fuselage about a horizontal axis and are distributed around the circumference of the ring in some as yet unknown manner. The moment of inertia of the ring cross section is assumed constant. The effect of assuming that the skin shearing forces act at the neutral axis of the ring instead of at the centerline of the skin is regarded as negligible, since the depth of the ring is small as compared to its other dimensions.

The arc length s along the neutral axis of the ring is measured clockwise from the top, and the semicircumference is denoted by c.

Following the method previously described, Fourier analyses may be carried out for the figure formed by the neutral axis of the ring. Since the elliptical ring has two axes of symmetry, all even terms drop out leaving

$$\left.\begin{aligned} y &= a_1 \cos\theta + a_3 \cos 3\theta + a_5 \cos 5\theta + \ldots + a_{11} \cos 11\theta \\ x &= b_1 \sin\theta + b_3 \sin 3\theta + b_5 \sin 5\theta + \ldots + b_{11} \sin 11\theta \end{aligned}\right\} \quad (12)$$

where $\theta = \pi s/c$ and a_n and b_n are the coefficients determined from the Fourier analyses.

The elastic weights method will be used with notation as indicated by Fig. 3b. The initial equation of this method is

$$M = M_0 + X_m + X_v x + X_h y$$

in which the quantities are as previously defined. The first step in solving the problem is to determine an expression for M_0, the bending moment that would exist at any section of the ring if X_m, X_v, and X_h were all zero.

In dealing with thin sections it is convenient to work with the shear flow q, defined as the shearing stress times the section thickness. For the case of longitudinal bending of the fuselage about a horizontal axis, the expression for q may be found from any textbook of aeronautical structures to be (this shear flow develops only if the cross section of the fuselage at the location of the ring does not distort either in the plane of the cross section or perpendicularly to it)

$$q = \frac{V}{I} \int_e^f y \, dA$$

in which q is the shear flow in a fuselage cross section for which the vertical shear is V and at a point whose distance from the bending axis is denoted by e. The

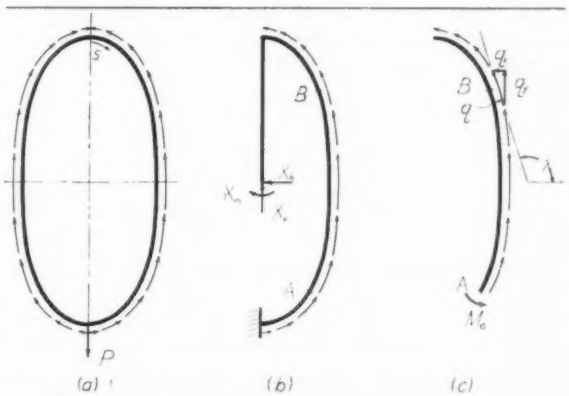

FIG. 3. Problem of elliptical ring with shear forces.

distance to the outer extremity of the section from the bending axis is f, and I is the moment of inertia of the entire fuselage cross section about the bending axis.

For this problem $V = P$ and $dA = t\,ds = (tc/\pi)\,d\theta$. Thus,

$$q = \frac{P}{I}\int_0^{\phi} y\frac{tc}{\pi}\,d\theta$$

where ϕ denotes the particular value of θ at the point in question. Now,

$$I = \int y^2\,dA = t\int_0^c y^2\,ds = \frac{tc}{2}\sum_{n=1,3,5\ldots}^{11} a_n^2$$

as was found in the previous example, and

$$\int_0^{\phi} y\,d\theta = = a_1\sin\phi + \frac{a_3}{3}\sin 3\phi + (a_5/5)\sin 5\phi + \ldots + (a_{11}/11)\sin 11\phi$$

Therefore,

$$q = \frac{2P}{\pi\sum a_n^2}\left(a_1\sin\phi + \frac{a_3}{3}\sin 3\phi + \ldots + \frac{a_{11}}{11}\sin 11\phi\right) \quad (13)$$

Now consider Fig. 3c. Point A $(x_A, y_A, s = s_A)$ is any point on the ring at which we wish to determine the moment M_0 due to the shear forces in the upper portion of the ring. If we can find an expression for the elementary moment produced at A by the skin shear force at any particular point B $(x_B, y_B, s = s_B)$, then an expression for M_0 at A may be obtained by letting the location of the point B vary from A to the free outer end of the half ring and summing the elementary moments by integration.

If we define $\beta = \pi s_A/c$ and $\phi = \pi s_B/c$, then x_A and y_A are functions of β and x_B and y_B are functions of ϕ.

Components of Skin Shear Force

To find the moment of the elementary shear force $q\,ds$ at B about A, it is convenient to resolve this force into horizontal and vertical components, $q_x\,ds$ and $q_y\,ds$, respectively. From Fig. 3c, with the horizontal component positive toward the left and the vertical component positive upward,

$$q_x\,ds = q\,ds\cos\lambda, \quad q_y\,ds = q\,ds\sin\lambda$$

The expressions for sine λ and cosine λ may be obtained from Eq. (12) by differentiation—that is,

$$\sin\lambda = -dy/ds = (\pi/c)(a_1\sin\phi + 3a_3\sin 3\phi + \ldots + 11a_{11}\sin 11\phi)$$

$$\cos\lambda = dx/ds = (\pi/c)(b_1\cos\phi + 3b_3\cos 3\phi + \ldots + 11b_{11}\cos 11\phi)$$

Since q is also represented in series form, the multiplication may be carried out and simplified by trigonometric identities. Disregarding higher harmonics,

$$\left.\begin{aligned} q_x &= \frac{P}{c\sum a_n^2}(B_2\sin 2\phi + B_4\sin 4\phi + \ldots + B_{12}\sin 12\phi) \\ q_y &= \frac{P}{c\sum a_n^2}(A_2\cos 2\phi + A_4\cos 4\phi + \ldots + A_{12}\cos 12\phi) \end{aligned}\right\} \quad (14)$$

where

$$A_i = \sum_{j=1,3,5,\ldots}^{11}\frac{a_j}{j}[(i+j)a_{i+j} - (i-j)a_{i-j}]$$

$$B_i = \sum_{j=1,3,5\ldots}^{11}\frac{a_j}{j}[(i-j)b_{i-j} - (i+j)b_{i+j}]$$

$(i = 2, 4, 6, \ldots, 12)$ subject to the definitions $a_{-n} = a_n$, $b_{-n} = -b_n$, $a_n = b_n = 0$ for $n > 11$. It is to be noted that A_i and B_i are constants dependent only upon the shape of the given ring.

Determination of M_0

Having now expressions for the horizontal and vertical components of the shear force, the value of M_0 at the point A is given by

$$M_0 = \frac{c}{\pi}\int_0^{\beta}[q_x(y_A - y_B) + q_y(x_A - x_B)]d\phi$$

or

$$M_0 = \frac{c}{\pi}\left[\int_0^{\beta} q_x y_A - \int_0^{\beta} q_x y_B + \int_0^{\beta} q_y x_A - \int_0^{\beta} q_y x_B\right]d\phi \quad (15)$$

For any particular point A the value of x_A and y_A are known fixed quantities. Performing the above indicated integration gives, for the first term,

$$\int_0^{\beta} q_x y_A\,d\phi = -\frac{Py_A}{c\sum a_n^2}\left[\frac{B_2}{2}\cos 2\beta + \frac{B_4}{4}\cos 4\beta + \ldots + \frac{B_{12}}{12}\cos 12\beta - \left(\frac{B_2}{2} + \frac{B_4}{4} + \ldots + \frac{B_{12}}{12}\right)\right]$$

The integration of the third term is similar, giving

$$\int_0^{\beta} q_y x_A\,d\phi = \frac{Px_A}{c\sum a_n^2}\left(\frac{A_2}{2}\sin 2\beta + \frac{A_4}{4}\sin 4\beta + \ldots + \frac{A_{12}}{12}\sin 12\beta + \beta\sum a_n^2\right)$$

The second and fourth terms are somewhat more complicated, since x_B and y_B are expressed by Eqs. (14) with θ replaced by ϕ, the specific value of θ at B. However, by multiplying out and simplifying, these two terms

may be integrated. We find

$$\int_0^\beta q_x y_B \, d\phi = -\frac{P}{2c\sum a_n^2}\left[C_1\cos\beta + \frac{C_3}{3}\cos 3\beta + \ldots + \frac{C_{11}}{11}\cos 11\beta - \left(C_1 + \frac{C_3}{3} + \ldots + \frac{C_{11}}{11}\right)\right]$$

$$\int_0^\beta q_y x_B \, d\phi = -\frac{P}{2c\sum a_n^2}\left[D_1\cos\beta + \frac{D_3}{3}\cos 3\beta + \ldots + \frac{D_{11}}{11}\cos 11\beta + \left(D_1 + \frac{D_3}{3} + \ldots + \frac{D_{11}}{11}\right) + 2\sum a_n^2\left(b_1\cos\beta + \frac{b_3}{3}\cos 3\beta + \frac{b_5}{5}\cos 5\beta + \ldots + \frac{b_{11}}{11}\cos 11\beta\right) - 2\sum a_n^2\left(b_1 + \frac{b_3}{3} + \frac{b_5}{5} + \ldots + \frac{b_{11}}{11}\right)\right]$$

C_i and D_i are constants given by

$$C_i = \sum_{j=1,3,5,\ldots}^{11} a_j(B_{i-j} + B_{i+j}), \qquad D_i = \sum_{j=1,3,5,\ldots}^{11} b_j(A_{i-j} - A_{i+j})$$

where we define $B_{-n} = -B_n$, $A_{-n} = A_n$, and $A_n = B_n = 0$ for $n = 0$ and $n > 11$.

Combining the various terms, the expression for M_0 for the section A at which $\theta = \beta$ becomes

$$M_0 = \frac{P}{2\pi\sum a_n^2}\left[(C_1 + D_1)(\cos\beta - 1) + \frac{C_3 + D_3}{3}(\cos 3\beta - 1) + \ldots + \frac{C_{11} + D_{11}}{11}(\cos 11\beta - 1)\right] + \frac{P}{\pi}\left[b_1(\cos\beta - 1) + \frac{b_3}{3}(\cos 3\beta - 1) + \ldots + \frac{b_{11}}{11}(\cos 11\beta - 1)\right] - \frac{Py_A}{\pi\sum a_n^2}\left[\frac{B_2}{2}(\cos 2\beta - 1) + \frac{B_4}{4}(\cos 4\beta - 1) + \ldots + \frac{B_{12}}{12}(\cos 12\beta - 1)\right] + \frac{Px_A}{\pi\sum a_n^2}\left(\frac{A_2}{2}\sin 2\beta + \frac{A_4}{4}\sin 4\beta + \ldots + \frac{A_{12}}{12}\sin 12\beta + \beta\sum a_n^2\right) \quad (16)$$

This represents the bending moment at A in the determinate structure due to the distributed skin reactions. It should be recognized that x_A, y_A, and β are constant for any given section A but change in value as the location of the section is changed. The reason for leaving x_A and y_A in this form rather than using their series expressions is to simplify the computation of M_0. Ordinarily, the coordinates of the point at which the moment is desired will be known and may be substituted directly in Eq. (16).

Now that an expression for M_0 has been determined, the quantities X_m, X_v, and X_h may be found. It is immediately obvious that X_v must be zero due to symmetry.

Evaluation of X_m and X_h

According to the elastic weights method,

$$X_m = -\left(\int_0^c M_0\,ds \Big/ \int_0^c ds\right) = -\left(\int_0^\pi M_0\,d\beta \Big/ \int_0^\pi d\beta\right) = -\frac{1}{\pi}\int_0^\pi M_0\,d\beta$$

Carrying out the integration,

$$X_m = \frac{P}{2\pi\sum a_n^2}\left(C_1 + D_1 + \frac{C_3 + D_3}{3} + \ldots + \frac{C_{11} + D_{11}}{11}\right) \quad (17)$$

Now,

$$X_h = -\left(\int_0^c M_0 y\,ds \Big/ \int_0^c y^2\,ds\right) = -\left(\int_0^\pi M_0 y\,d\beta \Big/ \int_0^\pi y^2\,d\beta\right)$$

Upon multiplying out and integrating, this becomes

$$X_h = -\frac{P}{2\pi(\sum a_n^2)^2}\left[a_1(C_1 + D_1 - E_1) + a_2\left(\frac{C_3 + D_3}{3} - E_3\right) + \ldots + a_{11}\left(\frac{C_{11} + D_{11}}{11} - E_{11}\right) + b_1F_1 + b_3F_3 + \ldots + b_{11}F_{11}\right] - \frac{P}{\pi\sum a_n^2}\left[a_1b_1 + a_3b_3 + \ldots + a_{11}b_{11} + \frac{B_2}{2} + \frac{B_4}{4} + \ldots + \frac{B_{12}}{12} - 2\left(\frac{G_2}{2} + \frac{G_4}{4} + \ldots + \frac{G_{12}}{12}\right)\right] \quad (18)$$

The constants are evaluated as follows:

$$E_i = \sum_{j=1,3,5,\ldots}^{11} a_j\{[B_{i-j}/(i-j)] + [B_{i+j}/(i+j)]\} \qquad (i = 1, 3, 5, \ldots, 11)$$

$$F_i = \sum_{j=1,3,5,\ldots}^{11} b_j\{[A_{i+j}/(i+j)] - [A_{i-j}/(i-j)]\} \qquad (i = 1, 3, 5, \ldots, 11)$$

$$G_i = \sum_{j=1,3,5,\ldots}^{11} a_j(b_{i-j} + b_{i+j}) \qquad (i = 2, 4, 6, \ldots, 12)$$

subject to $B_{-n} = -B_n$, $A_{-n} = A_n$, $b_{-n} = -b_n$, and $B_n = A_n = b_n = 0$ for $n = 0$ and $n > 11$.

The bending moment at any section of the ring may now be found from

$$M = M_0 + X_m + X_h y_0$$

where M_0 for the particular section is found from Eq. (16). X_m and X_h are the values found from Eqs. (17) and (18), and y_0 is the ordinate of the point in question.

The expressions for the normal and shear forces are

$$N = (X_h + \int_0^{s_0} q_x\, ds)\cos\lambda + \int_0^{s_0} q_y\, ds \sin\lambda$$

$$V = (X_h + \int_0^{s_0} q_x\, ds)\sin\lambda + \int_0^{s_0} q_y\, ds \cos\lambda$$

in which s_0 is the value of the arc length at the section under consideration and the other quantities are as previously defined.

The several constants a_i, b_i, A_i, B_i, . . ., G_i are functions only of the shape of the ring and are calculated without reference to any particular section. Once they have been computed, the bending moment at a number of sections may be readily found.

Because of the representation of the shape of the ring by Fourier series, the foregoing analysis is valid not only for a true elliptical ring but also for any ring symmetrical about two axes. The effect of different shapes of rings is merely to change the values of the constants used in the general expressions derived above.

Effect of Higher Terms

As before, the higher terms of the series for x and y may be neglected with but small effect upon the final result. In a particular case, when all six terms of the series were used, the results were found to be

$$X_h = -0.142P, \qquad X_m = 1.39P$$

while, when only the first three terms of the series were used, it was found that

$$X_h = -0.145P, \qquad X_m = 1.41P$$

The error is about 2 per cent, while the amount of computation saved is significant. It is particularly desirable to neglect many of the higher terms in the case of rings having but one axis of symmetry when the series for x and y each contain both odd and even terms.

Conclusions

The method here presented is simple, in itself, and it requires no extensive mathematical background. It is applicable to any ring with at least one axis of symmetry, whether or not the loading is symmetrical. For nonsymmetrical loadings, the entire ring, rather than only one-half, must be considered and the quantity X_v must be evaluated.

It is recognized that the use of Fourier series presents certain disadvantages. The most important of these from the practical point of view is that the process of deriving original solutions is somewhat cumbersome, particularly when distributed skin reactions are considered. However, once a solution has been arrived at for a given oval ring and condition of loading, the bending moment at any number of sections may be quickly determined. Also, the solution may be applied to any other ring with similar loading merely by varying the constants. As was pointed out, the amount of computation required may be considerably reduced by using fewer terms in the original series with but little sacrifice of accuracy.

This method of analysis was originally intended to apply to aircraft fuselage rings. It may, however, be advantageously applied to any ring having one axis of symmetry. Since commonly only concentrated loads will be involved in other than aeronautical applications, the solutions will be simple.

References

[1] Burke, W. F., *Working Charts for the Stress Analysis of Elliptic Rings*, N.A.C.A. T.N. No. 444, 1933.

[2] Miller, R., and Wood, K., *Formulas for the Stress Analysis of Circular Rings in a Monocoque Fuselage*, N.A.C.A. T.N. No. 462, 1933.

[3] Greenwood, E., *A Method of Stress Analysis of Monocoque Fuselage Circular Rings*, Journal of the Aeronautical Sciences, Vol. 3, No. 12, pp. 440–443, October, 1936.

[4] Ruffner, B., *Monocoque Fuselage Circular Ring Analysis*, Journal of the Aeronautical Sciences, Vol. 6, No. 3, pp. 114–116, January, 1939.

(*Concluded on page 608*)

Two-Dimensional Airfoils at Moderate Hypersonic Velocities

WILLIAM H. DORRANCE*

Consolidated Vultee Aircraft Corporation

(I) Summary

Expressions for lift, drag, and pitching moment coefficients are derived for a large number of airfoil sections in two-dimensional hypersonic flow. These expressions, differing from those obtained using linearized, second-order, and third-order theories, can be used throughout a moderate range of hypersonic Mach Numbers. The fundamental parameter of these formulas is the two-dimensional hypersonic flow similarity parameter, $K = M_0\delta$. To obtain these expressions, the shock-wave and expansion-wave equations for pressure ratios across such waves are expanded in powers of K. Following this, it is shown that the first three terms so obtained for both wave types are practically identical for values of K less than about 1.0. Further, it is shown that they closely approach the exact pressure-ratio expressions. The application of the expressions thus derived to various airfoil sections is then demonstrated, and a table of airfoil coefficients is presented. It is shown that the airfoil formulas can be applied to finite wings with reasonable accuracy for design estimations.

(II) Symbols and Nomenclature

A = plan-form area
A.R. = aspect ratio
C_D = drag/ql = drag coefficient per unit span
C_p = pressure coefficient
C_x = F_x/ql = chordwise force coefficient per unit span
C_y = F_y/ql = normal force coefficient per unit span
C_θ = M_θ/ql^2 = pitching moment coefficient per unit span (positive in stall)
f = $f(\xi, \beta)$ = thickness distribution function [see Eqs. (3) and (4)]
F_x, F_y = chordwise and normal force components
H = stagnation pressure
i, j = indices [see Eq. (49)]
K = $M_0\delta$, hypersonic similarity parameter
l = chord length
M = Mach Number
M_θ = pitching moment, positive in stall
p = static pressure
q = dynamic pressure
R = area ratio (see Fig. 8)
s = span
t = thickness
x_a = chordwise location of pitching moment center
x, y = body coordinates (see Fig. 1)

Greek Symbols

α = angle of attack
β = α/δ
γ = ratio of specific heats
δ = t/l, thickness ratio
η = $2y/t$, dimensionless coordinate (see Fig. 1)
λ = shock-wave angle
ξ = $2x/l$, dimensionless coordinate (see Fig. 1)
ω = flow deflection angle, positive "into" a corner, negative "around" a corner

Subscripts

0 = free stream when used with Mach umber; origin when used with pitching moment
1 = local
l = lower surface
u = upper surface

The symbol $O[\ ]$ denotes "order of" term within brackets.

Received February 26, 1952.

* Senior Aerodynamics Engineer, San Diego Division.

(III) Discussion

It has been demonstrated that long-range missiles require hypersonic† Mach Numbers for efficient operation.[1, 2] To date, considerable work has been devoted to the aerothermodynamics of hypersonic flight in the upper atmosphere. In this region the molecular mean free paths are comparable to or exceed the significant dimensions of a missile and its external flow field, and the concepts of the kinetic theory of gases apparently apply.[3–9] This paper, however, is concerned with the aerodynamics of hypersonic flight at altitudes wherein the laws of continuum flow theory apply.

Ivey, Klunker, and Bowen[10] proposed a method of treating the continuum flow about simple bodies at extreme hypersonic Mach Numbers. This method, based on Newtonian flow concepts, might be expected to apply at Mach Numbers of the order of 10 to 15 (say) or higher if the effects of viscosity and molecular vibration and dissociation in the flow field do not modify the flow behavior appreciably. Since linearized theory is of dubious value above Mach Numbers of about 3, the missile designer is left with a void in the continuum flow region between Mach Numbers of about 3 and 10. Here he must either apply lengthy numerical methods, such as the method of characteristics, or make use of extrapolations to obtain pressure distributions and force and moment coefficients. It is the purpose of this paper to present a method of obtaining such aerodynamic coefficients for two-dimensional airfoils in this Mach Number region. The method appears to be applicable for airfoils of sensible thicknesses and angles of attack at Mach Numbers between about 3.0 and 12. The coefficients obtained using this method compare well with those obtained

† For the purposes of identification it will be assumed that hypersonic Mach Numbers refer to Mach Numbers of 3 and above. This definition is admittedly arbitrary.

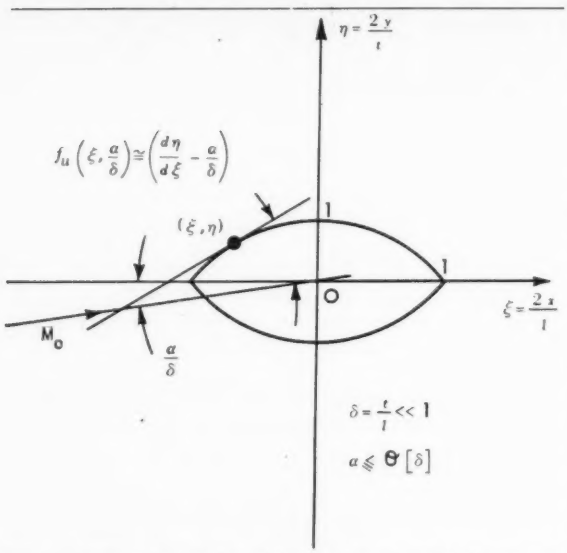

FIG. 1. Orientation of thin airfoil and relative velocity vector within dimensionless coordinate system (ξ, η).

using the shock-wave and expansion-wave equations in the customary piecewise manner.

In 1946 Tsien, using the equation of motion for two-dimensional compressible flow about slender and thin bodies, found a similarity parameter relating hypersonic flows about families of similar bodies.[11] This similarity parameter, when properly used, relates the pressure distribution and force and moment coefficients due to pressure stresses on a given body at a given hypersonic Mach Number to the pressure distribution and force and moment coefficients for bodies of the same thickness distribution at different hypersonic Mach Numbers related to the given Mach Number by the similarity rule. Indeed, if δ is defined as being the thickness ratio of the airfoil, if

$$\xi = 2x/l, \qquad -1 \leq \xi \leq 1 \tag{1}$$

$$\eta = 2y/t, \qquad -1 \leq \eta \leq 1 \tag{2}$$

are defined as being dimensionless coordinates of the airfoil (Fig. 1), and if

$$f_u(\xi, \beta) = (d\eta/d\xi)_u - \beta \tag{3}$$

$$f_l(\xi, \beta) = -(d\eta/d\xi)_l + \beta \tag{4}$$

where

$$\beta = \alpha/\delta \tag{5}$$

then, as will be demonstrated subsequently,

$$C_p/\delta^2 = P(K, \beta, \xi) \tag{6}$$

therefore,

$$C_y/\delta^2 = Y(K, \beta) \tag{7}$$

$$C_x/\delta^3 = X(K, \beta) \tag{8}$$

$$C_\theta/\delta^2 = \Theta(K, \beta) \tag{9}$$

where

$$K = M_0\delta \tag{10}$$

is the hypersonic similarity parameter.

Linnell has utilized this similarity parameter to derive and present expressions for pressure, force, and moment coefficients for two-dimensional airfoils in hypersonic flows.[12] His expressions for pressure coefficient, however, were different for flow fields behind compression waves and expansion waves and, as such, precluded the obtaining of force and moment coefficients for airfoil sections in closed form. Nevertheless, Linnell's method represented some saving in labor over the application of shock-wave and expansion-wave formulas to two-dimensional airfoils when K was of the order of 1 or less. Smelt showed that, for hypersonic flows of low values of K, one expression for the pressure ratios across shock waves and expansion waves could be derived which approximated the full Rankine-Hugoniot and Prandtl-Meyer pressure ratios accurately.[13] In obtaining these expressions, Smelt used a slightly different similarity parameter not intrinsically different from Tsien's. In essence, this removed the dependency of the pressure ratio for any point on the surface of a two-dimensional airfoil on the number and type of wave fronts between the point and the undisturbed free stream. Airfoil coefficients in closed form could then be obtained.

The present paper derives expansions in powers of K from the Rankine-Hugoniot and Prandtl-Meyer pressure coefficient ratios. Because Tsien's K is the parameter of the expansion, the expressions obtained differ from Smelt's expressions. The two expressions derived in this manner are shown to be almost identical and closely approximated by one three-term equation for $K \leq 1.0$. Using the three-term approximation, general and particular expressions for the aerodynamic coefficients of two-dimensional airfoils are obtained in closed form.

(IV) Presentation of the Theory

(*a*) *The Expansion-Wave Equation for Pressure Coefficient*

The Prandtl-Meyer equation relating Mach Numbers across a supersonic isentropic expansion through an angle ω can be written [see reference 14, making use of Eq. (13.10b)] as

$$-\omega = \left(\frac{\gamma+1}{\gamma-1}\right)^{1/2} \tan^{-1}\left[\left(\frac{\gamma-1}{\gamma+1}\right)^{1/2}(M_1^2-1)^{1/2}\right] - \tan^{-1}\left[\left(\frac{\gamma-1}{\gamma+1}\right)^{1/2}(M_0^2-1)^{1/2}\right]\Bigg\} - \left\{\tan^{-1}[M_1^2-1]^{1/2} - \tan^{-1}[M_1^2-1]^{1/2}\right\} \tag{11}$$

The symbols in Eq. (11) are illustrated in Fig. 2a. For $M_0^2[(\gamma-1)/(\gamma+1)] > 1$, $M_1 > M_0$, Eq. (11) can be approximated by

$$-\omega = \frac{2}{\gamma - 1}\left\{\left(\frac{1}{M_0} - \frac{1}{M_1}\right) + O\left[\frac{4\gamma}{3(\gamma - 1)^2}\left(\frac{M_0^3 - M_1^3}{M_1^3 M_0^3}\right)\right]\right\} \quad (12)$$

Now, for isentropic flow, we can write [Eq. (45) reference 15]

$$\frac{p_1}{p_0} = \left\{\frac{M_0^2\,1 + [2/(\gamma - 1)M_0^2]}{M_1^2\,1 + [2/(\gamma - 1)M_1^2]}\right\}^{\gamma/\gamma - 1} \quad (13)$$

and, for $M_0 > [2/(\gamma - 1)]^{1/2}$,

$$\frac{p_1}{p_0} = \left(\frac{M_0}{M_1}\right)^{2\gamma/\gamma - 1}\left\{1 + O\left[\frac{4}{(\gamma - 1)^2 M_0^2 M_1^2}\right]\right\}^{\gamma/\gamma - 1} \quad (14)$$

or, neglecting terms of the second order in the brackets and combining the first term of Eq. (12) with Eq. (14) yields

$$C_p = \left(\frac{p_1}{p_0} - 1\right)\frac{2}{\gamma M_0^2} = \frac{2}{\gamma M_0^2}\left\{\left[1 + \left(\frac{\gamma - 1}{2}\right)M_0\omega\right]^{2\gamma/\gamma - 1} - 1\right\} \quad (15)$$

Further expansion yields, for $|[(\gamma - 1)/2]M_0\omega| < 1$,

$$C_p = \frac{2\omega}{M_0} + \frac{\gamma + 1}{2}\omega^2 + \frac{\gamma + 1}{6}M_0\omega^3 + O\left[\frac{(\gamma + 1)(3 - \gamma)M_0^2\omega^4}{48}\right] \quad (16)$$

Now, from Fig. 1,

$$\omega = f(\xi, \beta)\delta$$

therefore, from Eq. (16),

$$\frac{C_p}{\delta^2} = \frac{2}{K}f + \frac{\gamma + 1}{2}f^2 + \frac{(\gamma + 1)K}{6}f^3 + O\left[\frac{(\gamma + 1)(3 - \gamma)K^2 f^4}{48}\right] \quad (17)$$

where, from the limit of convergence for Eq. (16), if $\gamma = 1.4$,

$$|fK| < 5 \quad (18)$$

The expression corresponding to Eq. (17) for pressure coefficient for surfaces behind oblique shock waves will now be derived.

(b) *The Shock-Wave Equation for Pressure Coefficient*

The Rankine-Hugoniot equation for pressure ratio across an oblique shock wave can be written [see reference 14, Eq. (4.29)] as

$$\frac{p_1}{p_0} = \frac{2\gamma}{\gamma + 1}M_0^2 \sin^2\lambda - \frac{\gamma - 1}{\gamma + 1} \quad (19)$$

Further [from reference 14 Eq. (4.27)],

$$\sin^2\lambda - \frac{\gamma + 1}{2}\frac{\sin\lambda \sin\omega}{\cos(\lambda - \omega)} - \frac{1}{M_0^2} = 0 \quad (20)$$

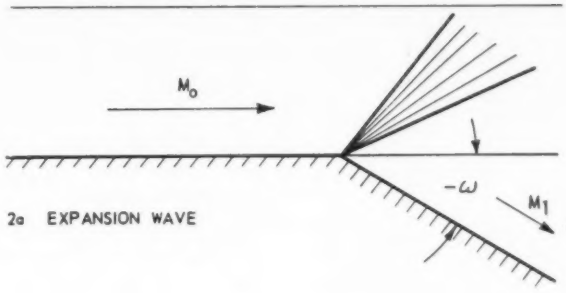

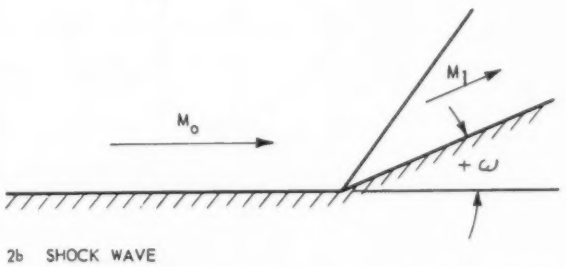

FIG. 2. Definition of angles used in shock- and expansion-wave equations.

The symbols appearing in Eqs. (19) and (20) are illustrated in Fig. 2b. Combination of Eqs. (19) and (20) yields

$$C_p = \frac{4}{\gamma + 1}\sin^2\lambda - \frac{4}{M_0^2(\gamma + 1)} \quad (21)$$

Now,

$$\frac{\sin\omega}{\cos(\lambda - \omega)} = \left\{\omega - \frac{\omega^3}{6} + \frac{\omega}{2}(\lambda - \omega)^2 + O\left[\frac{\omega^5}{120}\right]\right\} \quad (22)$$

Combining Eqs. (20) and (22) and solving for roots of $\sin\lambda$ yields

$$\sin\lambda = \frac{\gamma + 1}{4}\omega\left\{1 - \frac{\omega^2}{6} + \frac{(\lambda - \omega)^2}{2} + O\left[\frac{\omega^4}{120}\right]\right\} \pm \frac{1}{2}\left\{\left[\frac{\gamma + 1}{2}\omega\right]^2\left[1 - O\left[\frac{\omega^2}{6}\right]\right]^2 + \frac{4}{M_0^2}\right\}^{1/2} \quad (23)$$

where the positive sign is used since $\sin\lambda > 0$. For $\omega \ll \pi/2$ and $\lambda < 1$,

$$\sin\lambda = \frac{\gamma + 1}{4}\omega\left\{1 + \left[1 + \frac{16}{(\gamma + 1)^2 M_0^2\omega^2}\right]^{1/2}\right\} \quad (24)$$

If Eqs. (21) and (24) are combined, there results

$$C_p = \frac{\gamma + 1}{2}\omega^2 + \omega^2\left[\left(\frac{\gamma + 1}{2}\right)^2 + \left(\frac{2}{M_0\omega}\right)^2\right]^{1/2} \quad (25)$$

This equation agrees with expressions presented by Linnell[12] and Ivey and Cline.[16] Again, if, from Fig. 1, $\omega = f(\xi, \beta)\delta$ and if $K = M_0\delta$, then for

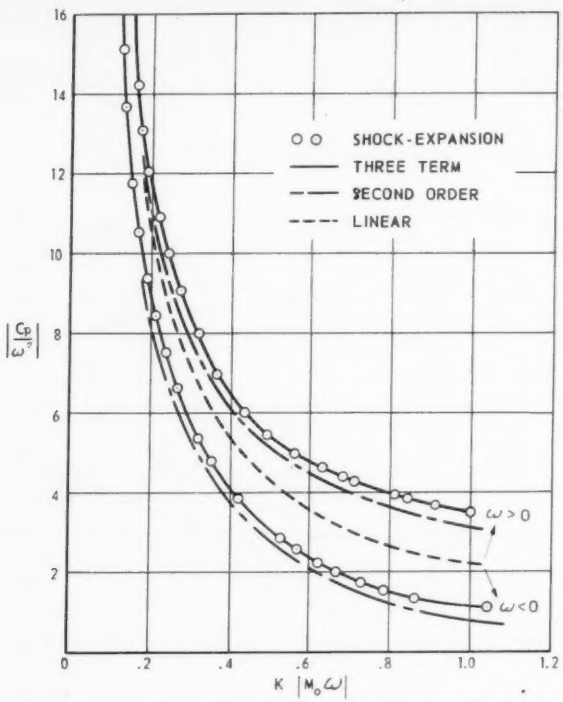

FIG. 3. $C_p\omega^{-2}$ versus $K = |M_0\omega|$ for compressions and expansions using exact, three-term approximation, second order, and linear theories.

$$\left|\frac{(\gamma+1)Kf}{4}\right| \equiv \left|\frac{(\gamma+1)M_0\omega}{4}\right| <$$

Eq. (25) can be expanded into

$$\frac{C_p}{\delta^2} = \frac{2}{K}f + \frac{\gamma+1}{2}f^2 + \frac{(\gamma+1)^2K}{16}f^3 + O\left[\frac{(\gamma+1)^4K^2f^5}{1{,}024}\right] \quad (26)$$

where, from the limit of convergence for Eq. (26), if $\gamma = 1.4$,

$$|fK| < 1.66 \quad (27)$$

and, as can be shown for $\omega \to 0$ and $(\lambda - \omega)^2 < 0.10$, using Eqs. (20) and (22),

$$M_0 \geq 3.19 \quad (28)$$

Eq. (26) completes the derivation of the basic expansion and shock-wave equations for pressure coefficient.

(c) *The Equation for Isentropic Low Pressure Coefficients*

It is apparent that Eqs. (17) and (26) are identical up to the third term. In fact, if it is assumed that Eq. (17) holds for both shock- and expansion-wave processes, the error introduced by the assumption is 10 per cent or less of the third term of Eq. (26) in the interval of convergence of Eq. (26) for $\gamma = 1.4$. Essentially, this implies that compressions at wedge angles satisfying inequalities (27) and (28) are isentropic for all practical purposes. Laitone[17] and others have pointed out that oblique shocks with small flow deflection angles and normal shocks at low supersonic Mach Numbers are essentially isentropic as is illustrated by the small loss in total pressure across such waves. The total pressure loss across an oblique shock wave of inclination angle λ is identical to the total pressure loss through a normal shock with free-stream Mach Number $M_0 \sin\lambda$. Therefore, the maximum total pressure loss for the shock waves concerned within this paper can be calculated using Eq. (24) to obtain maximum $M_0 \sin\lambda$ by substituting $Kf = M_0\omega \equiv 1$. For this case $M_0 \sin\lambda = 1.766$, and, from Table III of reference 15, $H_1/H_0 = 0.829$. This is a relatively small increase in entropy when compared to the entropy increase possible with larger flow deflections even at the lower range of Mach Numbers in the range of inequality (28).

Because both expansions and compressions are essentially isentropic within the interval

$$|fK| \leq 1.0, \quad M_0 > 3.19$$

the three-term approximation derived from Eq. (17) will be used to represent both compression and expansion-wave pressure coefficients. That is,

$$\frac{C_p}{\delta^2} = \frac{2}{K}f + \frac{\gamma+1}{2}f^2 + \frac{(\gamma+1)K}{6}f^3 \quad (29)$$

Fig. 3 presents the pressure coefficients for the hypersonic flow over the upper and lower surfaces of a flat plate. For the case of the flat plate $\delta \equiv 0$ and from Eqs. (3) and (4), $f\delta = \mp\omega$, where the negative sign applies to the upper surface. As can be seen from Fig. 3, the three-term approximation agrees very well with shock-expansion theory.[18] Linear theory and second-order theory expressions are also presented in Fig. 3. The three-term approximation exhibits better agreement with the shock-expansion theory than does either of the other two theories. Third-order theory, while not plotted in Fig. 3, would agree substantially with the three-term approximation.

Fig. 4 illustrates the region of validity of the three-term approximation in the M_0, $|\omega|$ plane. The region of validity of the linear theory has been superimposed on this plot for comparison purposes. This somewhat arbitrary region was obtained from the linear theory bounding inequality

$$|C_p| \cong \left|\frac{2\omega}{[M_0^2 - 1]^{1/2}}\right| << \frac{1}{M_0^2}$$

or, being liberal with this inequality and letting $K = M_0\omega$,

$$|K| < 0.125\,[1 - (1/M^2)]_0^{1/2}$$

As can be seen in Fig. 3, Eq. (29) has a relatively wide region of applicability when compared with the region of applicability of the linear theory shown on the same plot. It is interesting to note that the lower Mach Number limit of the three-term approximation is in the

vicinity of the practical upper Mach Number limit of the linear theory.

(V) Two-Dimensional Airfoil Coefficients

(a) *Derivation of Airfoil Coefficients*

Eq. (29) presents an expression for pressure coefficient which is an explicit function of thickness ratio, δ; chordwise dimensionless coordinate, ξ; normalized angle of attack, β; hypersonic flow similarity parameter, K; and the ratio of specific heats, γ. Because it has been shown that this equation will adequately represent the pressure coefficient at any point (ξ, η) on the surface of an airfoil without reference to the number and type of wave fronts between the point and the free stream, it is possible to obtain expressions for the common airfoil coefficients in closed form for any section shape for which the locus of the surface can be expressed in algebraic form. The resulting expressions, of course, can only be expected to be valid for values of M_0 greater than 3.19 and for $|fK| \leq 1.0$. Equations for chordwise force, drag, normal force, and pitching moment coefficients of a large number of airfoil sections are presented in this section following the derivation of the general expressions suitable for any airfoil section.

If an airfoil is situated in an x, y coordinate system such that the chord lies along the x axis and the midchord point is the origin, it can be shown that

$$C_x = \frac{1}{l}\int_{-l/2}^{l/2}\left[C_{p_u}\left(\frac{dy}{dx}\right)_u - C_{p_l}\left(\frac{dy}{dx}\right)_l\right]dx \tag{30}$$

$$C_y = \frac{1}{l}\int_{-l/2}^{l/2}(C_{p_l} - C_{p_u})\,dx \tag{31}$$

$$C_D = C_x + \alpha C_y \tag{32}$$

$$C_{\theta_0} = \frac{1}{l^2}\int_{-l/2}^{l/2}(C_{p_u} - C_{p_l})x\,dx \tag{33}$$

$$C_{\theta_a} = C_{\theta_0} + (x_a/l)C_y \tag{34}$$

for thin airfoils and small angles of attack. Referring to Fig. 1 and using the dimensionless coordinates ξ, η defined by Eqs. (1) and (2), Eqs. (30)–(34) become

$$C_x/\delta^3 = (1/2)\int_{-1}^{-1}(P_u f_u + P_l f_l)\,d\xi - (\alpha/\xi^3)C_y \tag{35}$$

$$C_y/\delta^2 = (1/2)\int_{-1}^{-1}(P_l - P_u)\,d\xi \tag{36}$$

$$C_D/\delta^3 = (1/2)\int_{-1}^{-1}(P_u f_u + P_l f_l)\,d\xi \tag{37}$$

$$C_{\theta_0}/\delta^2 = (1/4)\int_{-1}^{1}(P_u - P_l)\xi/d\xi \tag{38}$$

$$C_{\theta_a}/\delta^2 = (C_{\theta_0}/\delta^2) + (\xi_a/2\delta^2)C_y \tag{39}$$

If we define

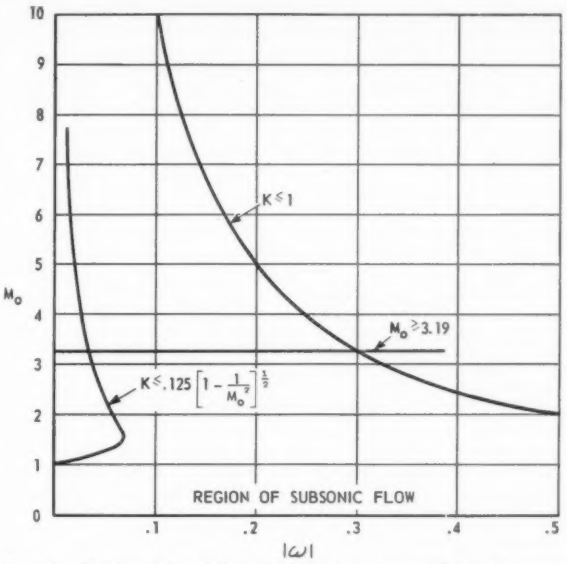

FIG. 4. Region of validity of three-term approximation compared with region of validity of linear theory.

$$C_1 = \frac{2}{K}, \quad C_2 = \frac{\gamma + 1}{2}, \quad C_3 = \frac{\gamma + 1}{6}K \tag{40}$$

then Eq. (29) becomes,

$$P(\xi, B) = C_1 f + C_2 f^2 + C_3 f^3 \tag{41}$$

Further, defining a recurring integral I_{ij} as

$$I_{ij} = \left(\frac{1}{2}\right)^{i+1}\int_{-1}^{1}\xi^i f^j d\xi \quad \begin{Bmatrix} i = 0, 1 \\ j = 1, 2, 3, 4 \end{Bmatrix} \tag{42}$$

Eqs. (36)–(38) can be written, using Eqs. (41) and (42),

$$C_y/\delta^2 = \sum_{j=1}^{3}[(I_{0j})_l - (I_{0j})_u]C_j \tag{43}$$

$$(C_x/\delta^3) + (\alpha C_y/\delta^3) = \sum_{j=2}^{4}[(I_{0j})_u + (I_{0j})_l]C_{j-1} = C_D/\delta^3 \tag{44}$$

$$C_{\theta_0}/\delta^2 = \sum_{j=1}^{3}[(I_{1j})_u - (I_{1j})_l]C_j = C_{\theta_a}/\delta^2 - \frac{\xi_a C_y}{2\delta^2} \tag{45}$$

Once the functions $f_u(\xi, \beta)$ and $f_l(\xi, \beta)$ are expressed in algebraic form for any airfoil, the integrals (43) can be evaluated and the airfoil coefficients obtained from Eqs. (43), (44), and (45). The limit $fK \leq 1.0$ can be expressed, using Eqs. (3) and (4), and solving for the limiting value of angle of attack,

$$|\alpha_{max.}| \leq (1.0/M_0) - |(dy/dx)_{max.}| \tag{46}$$

where $M_0 \geq 3.19$. These inequalities define the range of validity of the airfoil coefficients obtained using Eqs. (43), (44), and (45).

Table 1 presents airfoil coefficients for some common supersonic sections using these equations. Once values

TABLE 1

All equations are based on a dimensionless coordinate system (ξ, η) with origin at midchord. See Figure 1. Equations are valid for $M_\infty \geq 3.19$ and $|\alpha_{max}| \leq \frac{1}{M_\infty} - \left|\left(\frac{dz}{dx}\right)_{max}\right|$ where $\beta = \frac{1}{\delta}$, $K = M_\infty \beta$, $\beta = \frac{d}{\delta}$, t = maximum thickness, l = chord length, $\xi = \frac{2x}{l}$, $\eta = \frac{2z}{l}$, $C_1 = \frac{2}{K}$, $C_2 = \frac{(\gamma+1)}{2}$, $C_3 = \frac{(\gamma+1)K}{6}$

PROFILE		
Flat Plate	$\frac{C_\gamma}{\alpha} = 2(C_1 + C_2)$; $\frac{C_{\theta_0}}{\alpha^2} = 0$; $\frac{C_D}{\alpha} = 2(C_1 + C_2)$	
Symmetrical Double Wedge	$\frac{C_\gamma}{\delta^2}$	$2\beta\left\{C_1 + C_2(3+\beta^2)\right\}$
	$\frac{C_{\theta_0}}{\delta^2}$	βC_2
	$\frac{C_D}{\delta^2}$	$2C_1(\beta^2+1) + 2C_2(\beta^4+6\beta^2+1)$
Double Wedge n – Asymmetry $0 \leq \xi_1 < 1$	$\frac{C_\gamma}{\delta^2}$	$2\beta C_1 + 2\beta C_2\left\{\beta^2 + \frac{3}{1-\xi_1}\right\}$
	$\frac{C_{\theta_0}}{\delta^2}$	$\beta C_2 - \frac{3}{4}\beta C_3\left\{\frac{1+\xi_1}{1-\xi_1} - \frac{1-\xi_1}{1+\xi_1}\right\}$
	$\frac{C_D}{\delta^2}$	$2C_1\left\{\beta^2 + \frac{1}{1-\xi_1^2}\right\} + C_2\left\{\frac{1}{(1+\xi_1)^2} - \frac{1}{(1-\xi_1)^2}\right\} +$ $+ C_3\left\{\frac{1}{(1+\xi_1)^3} + \frac{1}{(1-\xi_1)^3} + 2\beta^4 + 6\beta^2\left[\frac{1}{1+\xi_1} + \frac{1}{1-\xi_1}\right]\right\}$
Modified Double Wedge	$\frac{C_\gamma}{\delta^2}$	$2\beta C_1 + 2\beta C_2\left\{\beta^2 + \frac{3}{2}\frac{1}{1-\xi_1} + \frac{3}{2}\frac{1}{1-\xi_2}\right\}$
	$\frac{C_{\theta_0}}{\delta^2}$	$\frac{1}{2}\beta C_2(\xi_1+\xi_2+2) - \frac{3}{4}\beta C_3\left\{\frac{1+\xi_1}{\xi_1-1} + \frac{1+\xi_2}{1-\xi_2}\right\}$
	$\frac{C_D}{\delta^2}$	$C_1\left\{2\beta^2 + \frac{1}{1-\xi_1} + \frac{1}{1-\xi_2}\right\} + C_2\left\{\frac{1}{(1-\xi_1)^2} - \frac{1}{(1-\xi_2)^2}\right\} +$ $+ C_3\left\{2\beta^4 + \frac{1}{(1-\xi_1)^2} + \frac{1}{(1-\xi_2)^2} + 6\beta^2\left(\frac{1}{1-\xi_1} + \frac{1}{1-\xi_2}\right)\right\}$
Flat Bottom Single Wedge	$\frac{C_\gamma}{\delta^2}$	$2\beta C_1 - 4C_2 + 2\beta C_3(6+\beta^2)$
	$\frac{C_{\theta_0}}{\delta^2}$	$-\frac{1}{2}C_1 + \beta C_2 - C_3\left(2+\frac{3}{2}\beta^2\right)$
	$\frac{C_D}{\delta^2}$	$2C_1(2+\beta^2) - 12\beta C_2 + 2C_3(\beta^4+12\beta^2+8)$

TABLE 1 (*Concluded*)

PROFILE		
Blunt T.E. Double Parabolic Arc	$\frac{C_\gamma}{\delta^2}$	$2\beta C_1 + 8\beta\xi_1\frac{C_2}{(1+\xi_1)^2} + 2\beta C_3\left\{\beta^2 + \frac{4(1+3\xi_1^2)}{(1+\xi_1)^2}\right\}$
	$\frac{C_{\theta_0}}{\delta^2}$	$\frac{4}{3}\beta C_2\frac{1}{(1+\xi_1)^2} + 8\beta\xi_1 C_3\frac{1}{(1+\xi_1)^3}$
	$\frac{C_D}{\delta^2}$	$\frac{2C_1}{(1+\xi_1)^2}\left\{\frac{4}{3}\cdot\beta^2(1-\xi_1)^4 + 3\xi_1^2\right\} + \frac{4C_2}{(1+\xi_1)^6}\left\{3\xi_1\beta^2(1-\xi_1)^4 + \right.$ $\left. + 4\xi_1(1-\xi_1^2)\right\} + 2\frac{C_3}{(1+\xi_1)^4}\left\{\beta^4(1-\xi_1)^8 + \right.$ $\left. + 8\beta^2(1+3\xi_1^2)(1-\xi_1)^4 + 16\left(\xi_1^4 + 2\xi_1^2 + \frac{1}{5}\right)\right\}$
Flat Bottom Blunt T.E. Single Parabolic Arc	$\frac{C_\gamma}{\delta^2}$	$2C_1\left\{\beta - \frac{2\xi_1}{(1+\xi_1)^2}\right\} + \frac{8C_2}{(1+\xi_1)^2}\left\{\beta\xi_1 - \frac{2(\frac{1}{3}-\xi_1^2)}{(1+\xi_1)^2}\right\} +$ $+ 2C_3\left\{\beta^2 - \frac{6\beta^2\xi_1}{(1+\xi_1)^2} + \frac{8\beta^2(1+3\xi_1^2)}{(1+\xi_1)^4} - \frac{32\xi_1(1+\xi_1^2)}{(1+\xi_1)^6}\right\}$
	$\frac{C_{\theta_0}}{\delta^2}$	$-\frac{2}{3}\frac{C_1}{(1+\xi_1)^2} - \frac{4}{3}\frac{C_2}{(1+\xi_1)^4}\left\{4\xi_1 - \beta(1+\xi_1)^2\right\} -$ $- \frac{2C_3}{(1+\xi_1)^6}\left\{16\left(\frac{1}{5}+\xi_1^2\right) - 8\beta\xi_1(1+\xi_1)^2 - \beta^2(1+\xi_1)^4\right\}$
	$\frac{C_D}{\delta^2}$	$2C_1\left\{\beta^2 + \frac{8(\frac{1}{3}+\xi_1^2)}{(1+\xi_1)^4} - \frac{4\beta\xi_1}{(1+\xi_1)^2}\right\} + \frac{8C_2}{(1+\xi_1)^2}\left\{\frac{3}{2}\beta^2\xi_1 - \right.$ $\left. - \frac{2\beta(1+3\xi_1^2)}{(1+\xi_1)^2} + \frac{8\xi_1(1+\xi_1^2)}{(1+\xi_1)^4}\right\} + 2C_3\left\{\beta^4 + \frac{128(\frac{1}{15}+2\xi_1^2+\xi_1^4)}{(1+\xi_1)^8} - \right.$ $\left. - \frac{128\beta\xi_1(1+\xi_1^2)}{(1+\xi_1)^6} + \frac{16\beta^2(1+3\xi_1^2)}{(1+\xi_1)^4} + \frac{8\beta^2\xi_1}{(1+\xi_1)^2}\right\}$

PROFILES		
Blunt T.E. Double Wedge	$\frac{C_\gamma}{\delta^2}$	$2\beta(C_1 + C_2) + \beta C_3\left(\frac{1}{2} + 2\beta^2\right)$
	$\frac{C_{\theta_0}}{\delta^2}$	0
	$\frac{C_D}{\delta^2}$	$C_1\left(\frac{1}{2} + 2\beta^2\right) + C_2\left(\frac{1}{4} + 3\beta^2\right) + C_3\left(\frac{1}{16} + 3\beta^2 + 2\beta^4\right)$
Symmetrical Biconvex	$\frac{C_\gamma}{\delta^2}$	$2\beta C_1 + 2\beta C_2\left\{\beta^2 + 4 + \frac{8}{5}\delta^2\right\}$
	$\frac{C_{\theta_0}}{\delta^2}$	$2\beta C_2\left(\frac{1}{3} + \frac{2}{15}\delta^2\right)$
	$\frac{C_D}{\delta^2}$	$2C_1\left(\frac{1}{3} + \beta^2 + \frac{8}{15}\delta^2\right) + 2C_2\left\{8\beta^2 + \frac{16}{5} + \beta^4 + \frac{16}{5}\beta^2\left(\beta^2 + \frac{12}{7}\right)\right\}$
Double Circular Arc, ξ – Asymmetry $\eta_1 = \frac{2t_1}{l}$, $\eta_2 = \frac{-2t_2}{l}$, $t = t_1 + t_2$	$\frac{C_\gamma}{\delta^2}$	$2\beta C_1 + \frac{8}{3}C_2(\eta_2+\eta_1) + 2\beta^2 C_2 + 4\beta C_3(\eta_1^2+\eta_2^2)$
	$\frac{C_{\theta_0}}{\delta^2}$	$\frac{1}{3}\beta C_2 - \frac{1}{3}C_3(\eta_2+\eta_1) - \frac{4}{5}C_3(\eta_2^3+\eta_1^3) - \beta^2 C_3(\eta_2+\eta_1)$
	$\frac{C_D}{\delta^2}$	$2C_1\left\{\beta^2 + \frac{2}{3}(\eta_1^2+\eta_2^2)\right\} + 8\beta C_2(\eta_1+\eta_2) +$ $+ 2C_3\left\{\beta^4 + 4\beta^2(\eta_1^2+\eta_2^2) + \frac{8}{5}(\eta_1^4+\eta_2^4)\right\}$
Modified Circular Arc	$\frac{C_\gamma}{\delta^2}$	$2C_1\beta + 2\beta C_2\left\{\beta^2 + 4\frac{(1-\xi_1^2)}{(1-\xi_1^2)^2}\right\}$
	$\frac{C_{\theta_0}}{\delta^2}$	$\frac{1}{3}\beta C_2\frac{(1-\xi_1^2)}{(1-\xi_1^2)}$
	$\frac{C_D}{\delta^2}$	$2C_1\left\{\beta^2 + \frac{4}{3}\frac{(1-\xi_1^2)}{(1-\xi_1^2)^2}\right\} + 2C_2\left\{\beta^4 + 8\beta^2\frac{(1-\xi_1^2)}{(1-\xi_1^2)^2} + \frac{16}{5}\frac{(1-\xi_1^2)}{(1-\xi_1^2)^4}\right\}$
Double Parabolic Arc	$\frac{C_\gamma}{\delta^2}$	$2\beta\left\{C_1 + C_2(4+\beta^2)\right\}$
	$\frac{C_{\theta_0}}{\delta^2}$	$\frac{4}{3}\beta C_2$
	$\frac{C_D}{\delta^2}$	$2C_1\left(\frac{1}{3} + \beta^2\right) + 2C_2\left(\beta^4 + 8\beta^2 + \frac{16}{5}\right)$
Flat Bottom Single Parabolic Arc	$\frac{C_\gamma}{\delta^2}$	$2\beta C_1 - \frac{16}{3}C_2 + 2\beta C_3(8+\beta^2)$
	$\frac{C_{\theta_0}}{\delta^2}$	$-\frac{2}{3}C_1 + \frac{4}{3}\beta C_2 - C_3\left(2\beta^2 + \frac{32}{5}\right)$
	$\frac{C_D}{\delta^2}$	$2C_1\left(\frac{8}{3} + \beta^2\right) - 16\beta C_2 + 2C_3\left(\beta^4 + 16\beta^2 + \frac{128}{5}\right)$

(*Table 1 concluded in next column*)

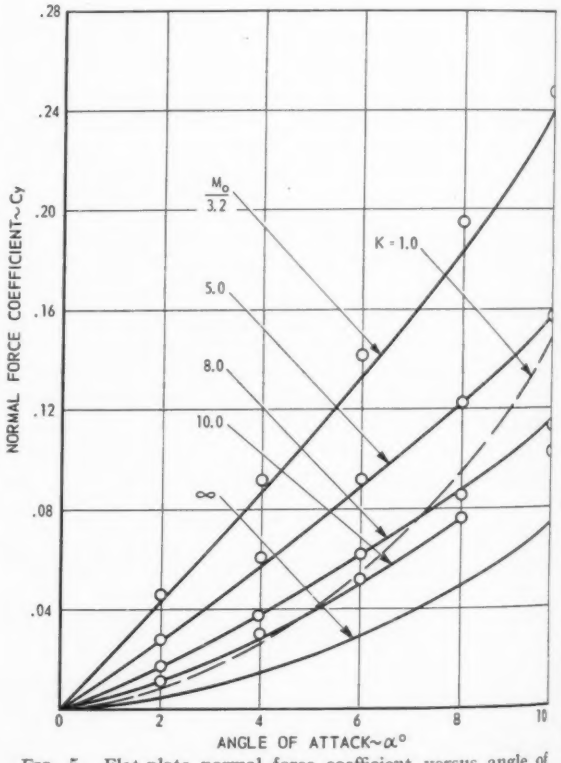

FIG. 5. Flat-plate normal force coefficient versus angle of attack. ——, Three-term approximation; ○ ○, shock-expansion theory.

of the C_j are determined by the thickness ratio, Mach Number, and ratio of specific heats, the coefficients are obtained as functions of β from Table 1.

(b) *Numerical Examples and Comparison with Theory*

Fig. 5 represents normal force coefficient versus angle of attack for a flat plate in the region of validity of inequalities (46). Also shown is the Newtonian flow[10,12,17] result applicable for $M_0 \to \infty$ obtained from Eqs. (15), (25), and (31)

$$C_y = (\gamma + 1)\alpha^2$$

Since the expression for normal force coefficient obtained using the three-term approximation is valid up to Mach Numbers of about 10 or 12, Fig. 5 suggests that shock-expansion theory be used for Mach Numbers between about 10 and those Mach Numbers where the theory of reference 10 is adequate.

Reference 19 presents experimentally determined values of normal force, pitching moment, and drag coefficient on a 5 per cent thick double-wedge rectangular plan-form wing at Mach Number 6.9. Figs. 6 and 7 present a comparison between the experimentally and theoretically determined values of normal force coefficient, center of pressure location, and drag coefficient, respectively. Inspection of Figs. 6 and 7 reveals that the present theory appears to agree with the experimental evidence even though the wing tested had an aspect ratio of 1 and the present theory applies to infinite aspect ratio wings.

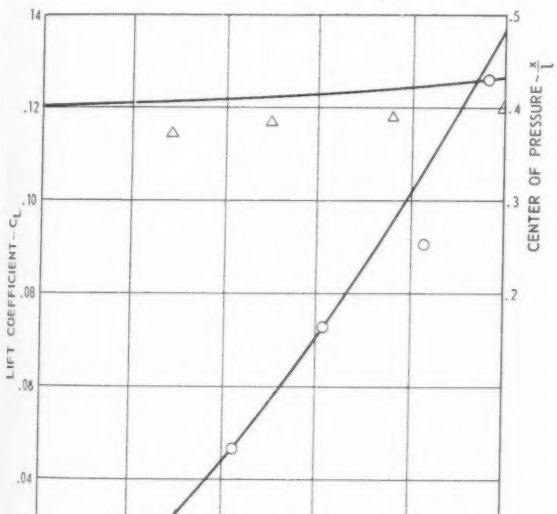

FIG. 6. Lift coefficient and center of pressure location versus angle of attack for symmetrical double-wedge airfoil at $M = 6.9$, A.R. = 1.0, and $\delta = 0.05$. ——, Three-term approximation; ○, Δ experiment (reference 19).

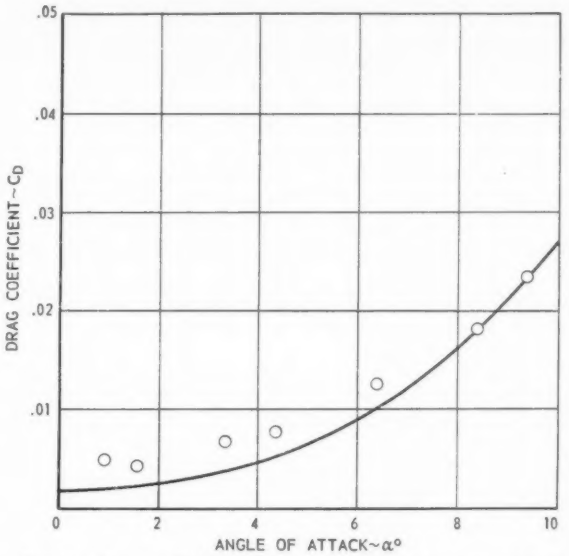

FIG. 7. Drag coefficient versus angle of attack for symmetrical double-wedge airfoil at $M = 6.9$, A.R. = 1.0, and $\delta = 0.05$. ——, Three-term approximation; ○ ○, experiment (reference 19). The addition of a skin-friction drag increment equal to 0.0028 brings theory and experiment into better agreement.

The agreement between the three-term approximation for infinite aspect ratio wings with measurements on a wing of finite aspect ratio is not surprising considering that the region of three-dimensional flow is confined to the region shaded on the plan form of Fig. 8. For a flat-plate rectangular plan-form airfoil, the ratio of the area of three-dimensional flow to the total plan-form area is, approximately,

$$R = [M_0^2 - 1]^{-1/2}(\text{A.R.})^{-1}$$

This ratio is plotted versus A.R.$[M_0^2 - 1]^{1/2}$ in Fig. 8 for M_0 greater than 3.19. As can be seen from Fig. 8, this ratio is less than 0.33 for plan forms of aspect ratios equal to or greater than 1.0. Since the lift in the three-dimensional flow is somewhere near one-half that indicated by two-dimensional theories such as that presented in this paper, the error introduced by using two-dimensional theory is somewhat less than 33 per cent for aspect ratios less than or equal to 1. This consideration indicates that two-dimensional theory can be used for three-dimensional thin wings for engineering estimates with small error.

(VI) Conclusions

(1) An expression for pressure coefficient as a function of the hypersonic similarity parameter and flow deflection angle has been derived suitable for use in the region $M_0 \geq 3.19$ and $|fK| \leq 1$ with reasonable accuracy.

(2) General and particular equations for lift, normal force, drag, chord force, and pitching moment co-

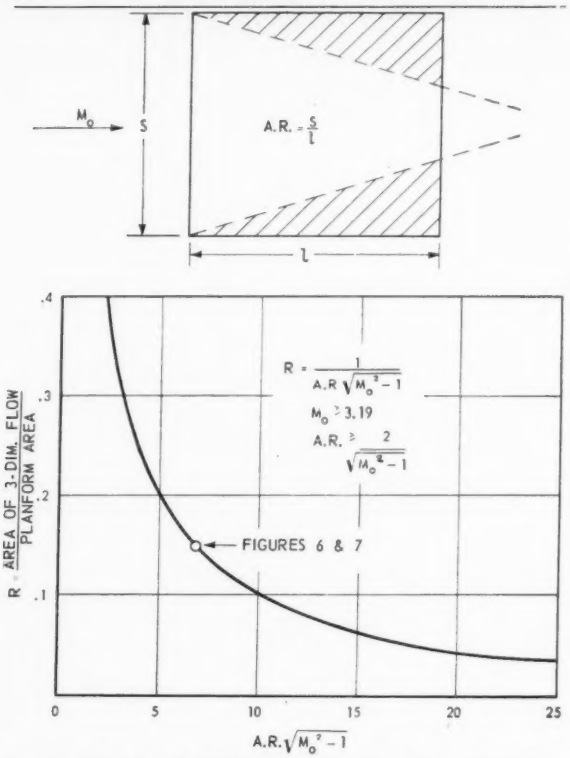

FIG. 8. Fraction of plan-form area in three-dimensional flow region for rectangular flat plate, $M_0 \geq 3.19$.

efficients of two-dimensional airfoil sections are derived and presented in closed form for use when $M_0 \geq 3.19$ and $|fK| \leq 1.0$.

(3) It is shown that the airfoil section formulas can be used for finite wings in the region of applicability of the theory for design estimates.

(4) The comparatively simple expression for the airfoil section coefficients can be used to determine profiles optimum with respect to aerodynamic characteristics, bending strength, torsional strength, etc.

REFERENCES

[1] Ivey, H. R., Bowen, E. N., Jr., and Oborny, L. F., *Introduction to the Problem of Rocket-Powered Aircraft Performance*, N.A.C.A. T.N. No. 1401, December, 1947.

[2] Ley, W., *The Upper Atmosphere—Its Exploration and Exploitation*, Aeronautical Engineering Review, Vol. 10, No. 2, p. 20, February, 1951.

[3] Zahm, A. F., *Superaerodynamics*, Journal of the Franklin Institute, Vol. 217, pp. 153–166, 1934.

[4] Sanger, E., *The Gas Kinetics of Very High Flight Speeds*, translation of ZWB Forschungskericht M. 972, May, 1938; N.A.C.A. T.M. No. 1270, May, 1950.

[5] Tsien, H. S., *Superaerodynamics, Mechanics of Rarefied Gases*, Journal of the Aeronautical Sciences, Vol. 13, No. 12, pp. 653–664, December, 1946.

[6] Snow, R. M., *Aerodynamics in a Highly Attenuated Atmosphere*, U.S. Navy Publication RLA-4.

[7] Ashley, H., *Applications of the Theory of Free Molecule Flow to Aeronautics*, Institute of the Aeronautical Sciences, Fairchild Fund Paper No. 164.

[8] Stalder, J. R., and Jukoff, D., *Heat Transfer to Bodies Traveling at High Speed in the Upper Atmosphere*, N.A.C.A. T.N. No. 1682, 1948.

[9] Heineman, M., *Theory of Drag in Highly Rarefied Gases*, Communications on Pure and Applied Mathematics, Vol. 1, No. 3, pp. 259–273, September, 1948.

[10] Ivey, H. R., Klunker, E. B., and Bowen, E. N., *A Method for Determining the Aerodynamic Characteristics of Two and Three Dimensional Shapes at Hypersonic Speeds*, N.A.C.A. T.N. No. 1613, July, 1948.

[11] Tsien, H. S., *Similarity Laws of Hypersonic Flows*, Journal of Mathematics and Physics, Vol. XXV, No. 3, p. 247, October, 1946.

[12] Linnell, R. D., *Two-Dimensional Airfoils in Hypersonic Flows*, Journal of the Aeronautical Sciences, Vol. 16, No. 1, p. 22, January, 1949.

[13] Smelt, R., *Problems of Missiles at Extreme Speeds*, Naval Ordnance Laboratory Report No. 1131, Symposium on Ordnance Aeroballistics, June, 1949.

[14] Liepman, H. W., and Puckett, A. E., *Introduction to the Aerodynamics of a Compressible Fluid;* John Wiley & Sons, Inc., New York, 1947.

[15] Anon., *Notes and Tables for Use in the Analysis of Supersonic Flow*, N.A.C.A. T.N. No. 1428, December, 1947.

[16] Ivey, H. R., and Cline, C. W., *Effect of Heat-Capacity Lag on the Flow Through Oblique Shock Waves*, N.A.C.A. T.N. No. 2196, October, 1950.

[17] Laitone, E. V., *Exact and Approximate Solutions of Two-Dimensional Oblique Shock Flow*, Journal of the Aeronautical Sciences, Vol. 14, No. 1, p. 25, January, 1947.

[18] Ivey, H. R., Stickle, G. W., and Schuettler, A., *Charts for Determining the Characteristics of Sharp Nosed Airfoils in Two-Dimensional Flow at Supersonic Speeds*, N.A.C.A. T.N. No. 1143, January, 1947.

[19] McLellan, C. H., *Exploratory Wind-Tunnel Investigation of Wings and Bodies at $M = 6.9$*, Journal of the Aeronautical Sciences, Vol. 18, No. 10, p. 641, October, 1951.

The Effects on Dynamic Lateral Stability and Controllability of Large Artificial Variations in the Rotary Stability Derivatives

ROBERT O. SCHADE,* ORDWAY B. GATES, JR.,† AND JAMES L. HASSELL, JR.‡

Langley Aeronautical Laboratory, N.A.C.A.

SUMMARY

This paper presents the results of a theroetical and experimental investigation of the effects of large artificial variations of several stability derivatives on dynamic lateral stability and controllability. The derivatives considered were the yawing-moment-due-to-yawing velocity C_{n_r}, the rolling-moment-due-to-rolling velocity C_{l_p}, the yawing-moment-due-to-rolling velocity C_{n_p}, the rolling-moment-due-to-yawing velocity C_{l_r}, and the yawing-moment-due-to-rolling acceleration $C_{n_{\dot{p}}}$. Although the results do not apply directly to airplanes or flight conditions other than the two herein investigated, it is believed that the trends obtained might give an indication of the general effects of artificial stabilizing devices that cause changes in these derivatives. It was found that increases in oscillatory stability could be obtained by changes in any of the derivatives, but in some cases these increases in oscillatory stability were accompanied by detrimental effects on controllability and on the stability of the aperiodic modes. It appears from the results that the simultaneous change in two of the derivatives might be more satisfactory than a change in a single derivative for improving the damping of the oscillation without impairing the other flight characteristics.

INTRODUCTION

RECENTLY, MUCH INTEREST has been shown in artificial stabilization devices as a means for improving the damping of the lateral oscillation of airplanes. Such devices have been used on a number of airplanes in the form of yaw dampers. The yaw damper is essentially a gyroscope sensitive to the yawing velocity with its output used to control a servomechanism that operates the rudder to damp the yawing motion of the airplane. In an idealized system, such a device produces a variation in the stability derivative C_{n_r}, the yawing moment due to yawing; similar devices can be used to vary the damping-in-roll derivative C_{l_p}, the yawing-moment-due-to-rolling derivative C_{n_p}, or the rolling-moment-due-to-yawing derivative C_{l_r}.

In order to study the effects of large variations of these four rotary stability derivatives on the dynamic stability and control characteristics of airplanes, an investigation is being conducted at the Langley Aeronautical Laboratory of the N.A.C.A. The effect of another parameter, $C_{n_{\dot{p}}}$, the yawing-moment-due-to-rolling acceleration, has also been studied, since it affects the stability of an airplane in a manner similar to the product-of-inertia parameter that is known to have a powerful effect on the lateral oscillation.

Increasing the value of either of the damping derivatives C_{n_r} or C_{l_p} increases the total damping of the airplane, while changing the value of either of the cross derivatives C_{n_p} or C_{l_r} or the acceleration derivative $C_{n_{\dot{p}}}$ primarily causes a redistribution of the natural damping of the system among the various modes of motion. Because of the cross coupling between the rolling and yawing motions in a lateral oscillation, it is possible to increase the damping of both of these motions by the use of any one of the five derivatives under consideration. This point is emphasized because some groups working with automatic stabilization systems have the erroneous conception that an airplane must be stabilized independently about the rolling and yawing axes.

One phase of the investigation involved the correlation of dynamic lateral stability calculations for a 45° sweptback wing airplane (hereafter referred to as airplane A) with experimental results obtained in the Langley free-flight tunnel from a $^1/_9$-scale model of this airplane through a wide range of values of C_{n_r}, C_{l_p}, C_{n_p}, and C_{l_r}. These calculations and tests were made for a low-speed condition. The second phase of the investigation involved a theoretical analysis of the effect of several artificial stabilization devices on the lateral stability and controllability of a straight-wing airplane (hereafter referred to as airplane B) for a high-speed flight condition. This phase of the investigation included studies of the effects of wide variations of C_{n_r}, C_{n_p}, and $C_{n_{\dot{p}}}$.**

Presented at the Aerodynamics Session, Twentieth Annual Meeting, I.A.S., New York, January 28–31, February 1, 1952.

* Aeronautical Engineer.

† Aeronautical Research Scientist.

‡ Aeronautical Research Scientist.

** In order to simplify the analysis, most of the calculations were made assuming idealized artificial-stabilization systems, but a few check calculations were made taking into account the small constant time lag of the stabilization device used in the tests. Extensive calculations were not made by this method, however, because of the extremely laborious process involved and because a systematic determination of the effect of time lag on stability throughout the variation of the four derivatives was considered beyond the scope of the present investigation.

Although the results do not apply directly to airplanes or flight conditions other than those investigated, it is believed that the trends presented might give a qualitative indication of the general effects of large variations of these stability derivatives.

Symbols and Coefficients

The forces and moments are referred to the stability axes, which are defined as an orthogonal system of axes intersecting at the airplane center of gravity in which the Z-axis is in the plane of symmetry and perpendicular to the relative wind, the X-axis is in the plane of symmetry and perpendicular to the Z-axis, and the Y-axis is perpendicular to the plane of symmetry. The symbols and coefficients are defined as follows:

ϕ = angle of roll, rad.
ψ = angle of yaw, rad.
β = angle of sideslip, rad.
r = yawing angular velocity, rad. per sec. or deg. per sec. $(d\psi/dt)$
p = rolling angular velocity, rad. per sec. or deg. per sec. $(d\phi/dt)$
$\dot{p}$ = rolling angular acceleration, rad. per sec. per sec. $(d^2\phi/dt^2)$
V = air speed, ft. per sec.
ρ = mass density of air, slugs per cu.ft.
q = dynamic pressure, lbs. per sq.ft. $[(1/2)\rho V^2]$
b = wing span, ft.
S = wing area, sq.ft.
A = aspect ratio (b^2/S)
t = time, sec.
s_b = nondimensional time parameter based on span (Vt/b)
N = yawing moment, ft.lbs.
D_b = differential operator (d/ds_b)
$1/T_{1/2}$ = damping factor, reciprocal of the time to damp to half amplitude (positive values indicate stability and negative values indicate instability or time to double amplitude), 1/sec.
W = weight of airplane, lbs.
W/S = wing loading, lbs. per sq.ft.
m = mass of airplane, slugs (W/g)
g = acceleration due to gravity, ft. per sec. per sec.
μ_b = relative-density factor $(m/\rho Sb)$
η = inclination of principal longitudinal axis of airplane with respect to flight path, positive when principal axis is above flight path at the nose, deg.
γ = angle of flight path to horizontal axis, positive in a climb, deg.
k_{X_0} = radius of gyration in roll about principal longitudinal axis, ft.
k_{Z_0} = radius of gyration in yaw about principal vertical axis, ft.
K_{X_0} = nondimensional radius of gyration in roll about principal longitudinal axis (k_{X_0}/b)
K_{Z_0} = nondimensional radius of gyration in yaw about principal vertical axis (k_{Z_0}/b)
K_X = nondimensional radius of gyration in roll about longitudinal stability axis $(\sqrt{K_{X_0}^2 \cos^2\eta + K_{Z_0}^2 \sin^2\eta})$
K_Z = nondimensional radius of gyration in yaw about vertical stability axis $(\sqrt{K_{Z_0}^2 \cos^2\eta + K_{X_0}^2 \sin^2\eta})$
k_{XZ} = product-of-inertia factor $[k_{Z_0}^2 - k_{X_0}^2 \sin\eta \cos\eta]$
K_{XZ} = nondimensional product-of-inertia parameter $[K_{Z_0}^2 - K_{X_0}^2 \sin\eta \cos\eta]$
C_L = trim lift coefficient $(W \cos\gamma/qS)$
C_l = rolling-moment coefficient (rolling moment$/qSb$)
C_n = yawing-moment coefficient (yawing moment$/qSb$)
C_Y = lateral-force coefficient (lateral force$/qS$)

$C_{l_\beta} = \partial C_l/\partial\beta$
$C_{n_\beta} = \partial C_n/\partial\beta$
$C_{Y_\beta} = \partial C_Y/\partial\beta$
$C_{n_r} = \partial C_n/\partial(rb/2V)$
$C_{n_p} = \partial C_n/\partial(pb/2V)$
$C_{l_p} = \partial C_l/\partial(pb/2V)$
$C_{l_r} = \partial C_l/\partial(rb/2V)$
$C_{n_{\dot{p}}} = \partial C_n/\partial(\dot{p}b^2/4V^2)$
$C_{Y_p} = \partial C_Y/\partial(pb/2V)$
$C_{Y_r} = \partial C_Y/\partial(rb/2V)$
$C_{n_{\delta_r}} = \partial C_n/\partial\delta_r$
δ_r = rudder deflection, rad.
$|\delta_r/r|$ = gearing ratio, rate of change of rudder deflection with yawing angular velocity
$|\delta_r/p|$ = gearing ratio, rate of change of rudder deflection with rolling angular velocity
$|\delta_r/\dot{p}|$ = gearing ratio, rate of change of rudder deflection with rolling angular acceleration

Scope of the Investigation

The basic aerodynamic and mass characteristics of the two airplanes for the conditions chosen for this investigation are presented in Table 1, and, unless otherwise noted, all calculations were based on these values. The dynamic lateral stability characteristics of each of these airplanes were calculated by the conventional methods of reference 1. This investigation was made to study the trends of the various rotary stability derivatives which may be useful in artificial stabilization systems, and, in order to simplify the study, idealized artificial stabilization devices were assumed. In practical application, of course, the effect of the actual characteristics of the artificial stabilization system should also be considered.

Large variations of each of the rotary derivatives C_{n_r}, C_{l_p}, C_{n_p}, and C_{l_r} were accomplished in the tests of the free-flight tunnel model of airplane A by having the response signal from a small rate gyro located in the model operate the servomechanisms that moved the rudder or ailerons. With the particular artificial stabilizing devices used in these tests, it was possible to obtain essentially pure derivative changes because of the relatively small phase lag compared with the natural frequencies of the oscillations, because the gyro was mounted so that it would respond to either a pure yawing velocity or a pure rolling velocity about the stability axes, and because the rudder and ailerons were interconnected to produce either pure yawing moments or pure rolling moments.*

The geometric and mass characteristics of airplane A were adjusted to produce a neutrally stable oscillation for the basic condition. The flight tests of the

* Deflection of the all-movable vertical tail to produce the rolling and yawing moment derivatives also produced changes in the lateral force derivatives, C_{Y_p}, the lateral force due to rolling, and C_{Y_r}, the lateral force due to yawing. In the calculations, however, these changes in C_{Y_p} and C_{Y_r} were neglected because preliminary calculations indicated that even the largest changes in these derivatives did not appreciably affect the calculated results.

1/9-scale model were made for exactly the same condition for which calculations were made. In order to provide a direct comparison with the calculated oscillatory stability, the period and damping values obtained from these experiments have been scaled up to represent those of the full-scale airplane.

Since damping of the lateral oscillation is the primary function of any artificial stabilization system, only derivative variations in the directions that produce improvement in oscillatory stability will be discussed. More detailed studies of the effects of artificial stabilization on each of the airplanes herein discussed are to be found in references 2–4.

Results and Discussion

Effect of C_{n_r}

Airplane A.—The effect of large variations of C_{n_r} on the dynamic lateral stability of airplane A is presented in Fig. 1. These data are in the form of period and damping of the lateral oscillation and damping of the aperiodic or nonoscillatory modes of motion. The damping of both the oscillatory motion and the aperiodic motion is expressed in terms of the damping factor $1/T_{1/2}$, the reciprocal of the time to damp to half amplitude. Positive values of this damping factor indicate stability, and negative values indicate instability (time to double amplitude). Experimental values of the period and damping of the short-period lateral oscillation determined from flights of the model with various values of C_{n_r} are indicated by the symbols on Fig. 1. These values of period and damping were scaled up from values obtained from time histories of flights of the model such as the typical time histories presented in Fig. 2.

A comparison of the calculated and experimental values of period and damping of the lateral oscillation indicates good agreement for the various values of C_{n_r} tested. In the basic condition with a C_{n_r} value of -0.2 (indicated by the solid symbol on Fig. 1) the airplane had neutral oscillatory stability. Moderate increases in the value of C_{n_r} in the negative direction caused a marked improvement in damping of the short-period lateral oscillation. Maximum damping of the oscillation was obtained with a C_{n_r} value of about -2.0. Further increases in the value of C_{n_r} caused a reduction in damping of the lateral oscillation. In fact, oscillatory instability was obtained for values of C_{n_r} above -6.0. It is therefore apparent from both the flight-test results and the calculations that there exists some optimum value of C_{n_r} for best damping of the lateral oscillation. For the higher values of C_{n_r} (-3.0 to -7.0) the flight tests indicated that the lateral motion of the model progressively changed from the normal "dutch-roll" oscillation to a pendulum type of oscillation which was predominantly roll and sidewise displacement. The time histories of Fig. 2 show that, at a C_{n_r} value of

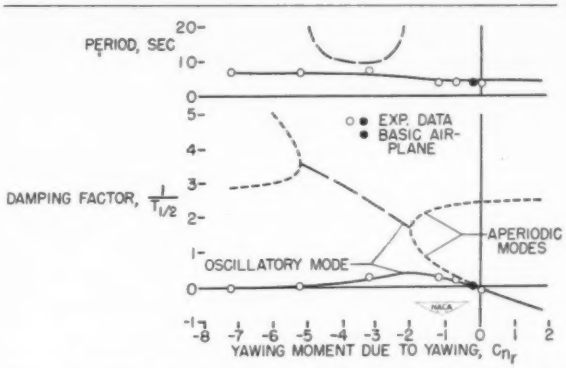

FIG. 1. Calculated effect of C_{n_r} on stability and comparison with experimental data for airplane A.

-7.2, the ratio of yaw to roll is approximately one-half the value obtained in the basic condition. This decrease in the ratio of yaw to roll is attributed to the fact that increasing the damping in yaw causes partial restraint of the yawing motions.

In order to determine the significance of the increase in the damping of the lateral oscillation obtainable by varying C_{n_r}, the results were compared with the Air Force and Navy requirements for damping of the lateral oscillation. This comparison shows that airplane A would meet the requirements with values of C_{n_r} between -0.7 and -4.6. The flight behavior in this range of C_{n_r} was very good, and there was no indication of the decreased maneuverability or "stiffness" in making turns, which has been experienced with some airplanes equipped with yaw dampers. Steady turning maneuvers to determine the effect of C_{n_r} on the maneuverability could not be made in the free-flight tunnel because of the restrictions imposed by the size of the test section.

The calculated stability in the negative C_{n_r} range indicates that the aperiodic modes of motion merge and form a second oscillation for C_{n_r} values between -2.0

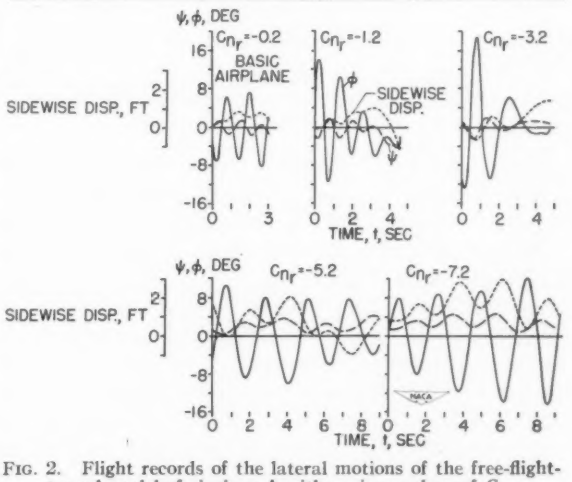

FIG. 2. Flight records of the lateral motions of the free-flight-tunnel model of airplane A with various values of C_{n_r}.

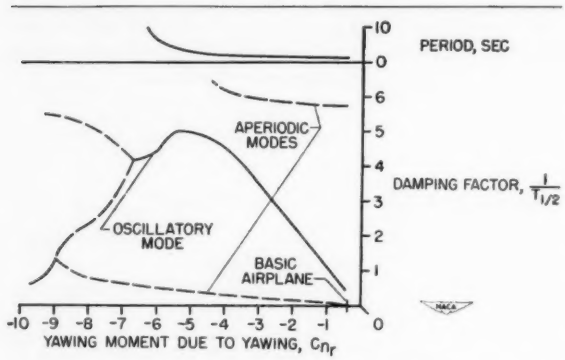

FIG. 3. Calculated effect of C_{n_r} on stability for airplane B.

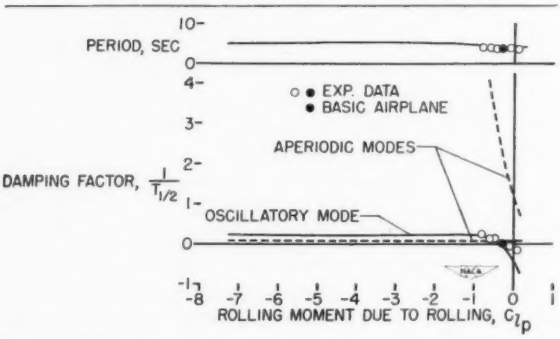

FIG. 4. Calculated effect of C_{l_p} on stability and comparison with experimental data for airplane A.

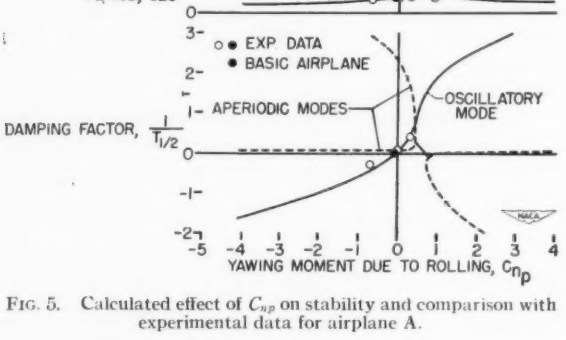

FIG. 5. Calculated effect of C_{n_p} on stability and comparison with experimental data for airplane A.

and -5.2. This oscillation was so heavily damped that it was never observed in the model flights. Although it was not possible to measure the damping of the aperiodic modes of motion from the flight tests, the pilot was aware of the increasingly good spiral stability of the model as the value of C_{n_r} was increased negatively, since the model had an increasingly strong tendency to fly uncontrolled along the centerline of the tunnel test section despite the natural gustiness of the airflow. This increase in spiral stability is shown by the flight records of Fig. 2 which indicate that it was possible to obtain longer uncontrolled flight records as C_{n_r} was increased negatively despite the lightly damped or unstable oscillations at the higher values of C_{n_r}.

Airplane B.—Calculations of the effect of large variations of C_{n_r} on the dynamic lateral stability for airplane B are presented in Fig. 3. Increasing C_{n_r} from the basic airplane value of -0.4 caused definite improvement in the damping of the lateral oscillation up to a value of C_{n_r} of approximately -5.4. Further increases in C_{n_r} above this value caused a reduction in damping of the lateral oscillation.

Above a C_{n_r} value of -6.7, the oscillatory mode broke down to form two more aperiodic modes. One of these aperiodic modes merged with the mode originally designated as the spiral mode at a C_{n_r} value of -9.0 to form a second oscillation. This second oscillation became increasingly less stable as C_{n_r} was increased beyond -9.0.

It may be noted that airplane B met the damping requirements from a C_{n_r} value of -0.7 up to the highest values investigated.

Generally speaking, the trends produced by varying C_{n_r} with airplane B were comparable to those for airplane A. That is, as C_{n_r} was varied negatively for both airplanes, the damping of the oscillatory modes increased up to some optimum value and then decreased, while the aperiodic modes showed increases in damping.

Effect of C_{l_p} Variation

The effect of large variations of the damping-in-roll derivative C_{l_p} on the dynamic lateral stability characteristics of airplane A are presented in Fig. 4. The experimental period and damping values indicated by the symbols on the figure were obtained from flight records similar to those previously presented for C_{n_r}. A comparison of the limited amount of experimental data with the calculated oscillatory stability for small values of C_{l_p} shows fairly good agreement. The damping of the oscillation with high negative values of C_{l_p} could not be determined experimentally because of the abnormal flight behavior of the model in that range. The rolling mode of motion was so heavily damped that the model was essentially restrained from rolling. This tendency toward restraint imposed by high negative C_{l_p} values, although undesirable from the standpoint of maneuverability, resulted in flights requiring little corrective control when the model was flown in a steady wing-level attitude. The restraint in roll experienced in the flight tests is indicated in the calculated results that show that one of the aperiodic modes of motion (the rolling mode) became increasingly stable as C_{l_p} was increased negatively.

As C_{l_p} was increased in the negative direction from the basic value of -0.3 (indicated by the solid symbol on Fig. 4), the damping of the short-period oscillation rapidly improved for values of C_{l_p} up to about -0.7. Further negative increases of C_{l_p} (to -7.3) produced

no further damping of the lateral oscillation. The airplane would just barely meet the damping requirements for values of C_{l_p} between -0.7 and -7.3. It is apparent from these results that almost all of the damping added to the system by increasing the damping-in-roll derivative C_{l_p} is absorbed by the aperiodic rolling mode of motion, while only a small part of the added damping goes into the damping of the oscillation.

Effect of C_{n_p}

Airplane A.—The dynamic lateral stability characteristics of airplane A as affected by large variations of the yawing-moment-due-to-rolling derivative C_{n_p} are presented in Fig. 5. Model flights were possible only for a limited range of C_{n_p} because, as will be discussed later, excessive amounts of aperiodic instability were encountered. The experimentally determined values of the period and damping of the oscillation are in fairly good agreement with the calculated characteristics.

These results indicate that, as C_{n_p} was varied in the positive direction from the basic condition, there was a rapid improvement in the damping of the lateral oscillation and that the damping requirements were satisfied with all C_{n_p} values greater than 0.1. This improvement in damping, however, was not obtained without a loss in stability elsewhere in the system. The calculations for values of C_{n_p} between 0 and 0.4 reveal that this improvement in oscillatory stability was obtained at the expense of the normally well-damped rolling mode. Even though this mode of motion remained stable up to the point of its merger with the other aperiodic mode at a C_{n_p} value of about 0.4, it was considerably less damped than in any other flight condition experienced in these tests.

The model of airplane A became touchy to fly as C_{n_p} was increased up to 0.4 and became extremely difficult to control for values of C_{n_p} greater than 0.4. Sustained flight was impossible for C_{n_p} values greater than 1.0. As the value of C_{n_p} was varied through this range (-0.1 to 1.0), the pilot complained of an increasingly strong tendency for the model to go into a tight turn in response to normal aileron control. To the pilot, this tendency appeared to be a severe case of spiral instability. The results of calculations, however, show that the stability of the spiral mode of motion remained unchanged up to a C_{n_p} value of 0.6, while there was a rapid decrease in stability of the rolling mode of motion. It appears, therefore, that a decrease in stability of the rolling mode of motion might sometimes be mistaken for spiral instability.

The two aperiodic modes merged to form a long-period oscillation that became unstable at a C_{n_p} value of 0.6. This oscillation was not observed in the flight tests because of its extremely long period of over 40 sec. Immediately after it became unstable, the long-period oscillation broke up to form two new aperiodic modes of motion, one of which became increasingly unstable as C_{n_p} was increased further.

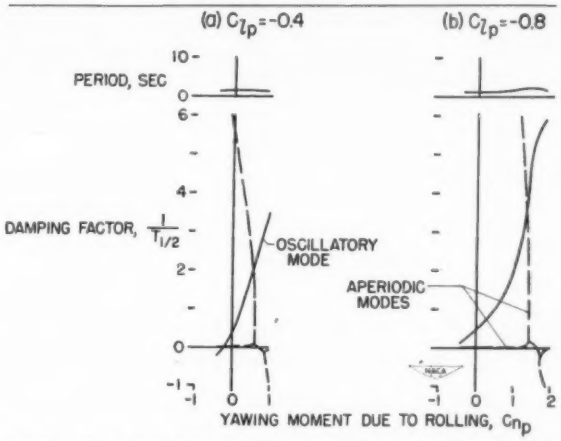

FIG. 6. Calculated effect of C_{n_p} on stability for airplane B with two values of C_{l_p}.

The results of these tests and calculations indicate that the derivative C_{n_p} might possibly be useful for redistributing the natural damping of an airplane so as to obtain a well-damped lateral oscillation and, at the the same time, obtain more maneuverability in roll. It is obvious, however, that the use of C_{n_p} is limited to values less than those that would cause the undesirable aperiodic motions experienced in these tests.

Airplane B.—The calculated dynamic lateral stability characteristics of airplane B, as affected by large variations of C_{n_p} for two values of C_{l_p} are presented in Fig. 6. The results of the calculations with the basic value of C_{l_p} (-0.40) are shown in Fig. 6a, and the results with C_{l_p} increased to -0.80 are shown in Fig. 6b.

As in the case of airplane A, the results of the calculations with the basic value of C_{l_p} show that, as C_{n_p} is increased positively, the damping of the lateral oscillation improves rapidly and the rolling mode becomes less stable. The damping requirements are satisfied for all values of C_{n_p} greater than 0.1.

It should be pointed out that for this airplane an increment of C_{n_p} of 0.62 resulted in the same damping of the oscillation as did an increment to C_{n_r} of -1.6. Physically, this indicates that the gearing ratio $|\delta r/r|$ required to obtain this damping with a C_{n_r} device is approximately 2.5 times as great as the gearing ratio $|\delta r/p|$ required with a C_{n_p} device. In many cases, however, the rudder motion required by the C_{n_p} device will be larger than that required by the C_{n_r} device because the rate of roll will often be more than 2.5 times as great as the rate of yaw.

The results previously presented for airplane A indicated that varying the stability derivative C_{l_p} had little effect on the damping of the lateral oscillation but caused large increases in the damping of the rolling mode. From these results it appeared probable that, if C_{l_p} were increased simultaneously with C_{n_p}, greater damping of the short-period oscillation might be obtained before the rolling mode had become too lightly

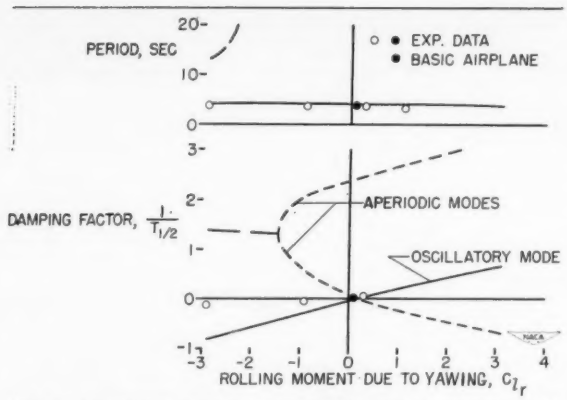

FIG. 7. Calculated effect of C_{l_r} on stability and comparison with experimental data for airplane A.

damped. Therefore, a case in which both C_{n_p} and C_{l_p} were increased was investigated. The effect of C_{n_p} on the stability of the lateral modes of motion when C_{l_p} was increased to -0.80 is shown in Fig. 6b. The results of these calculations show that, for a C_{n_p} value of 1.1, the damping of the short-period oscillation was appreciably increased when the damping of the rolling mode was the same as for the basic condition. Formation of the long-period oscillation was delayed to a higher value of C_{n_p}. These results indicate that, by increasing C_{n_p} and C_{l_p} simultaneously, it might be possible to increase the damping of the lateral oscillation without adversely affecting the lateral motions in other respects.

Effect of C_{l_r}

Airplane A.—The effect of large variations of C_{l_r} on the dynamic lateral stability characteristics of airplane A is shown in Fig. 7. The calculations indicate that increasing the value of C_{l_r} in a positive direction improved the damping of the lateral oscillation. The requirements for damping of the lateral oscillation were satisfied with values of C_{l_r} greater than 0.8, but, for these cases, the spiral mode of motion was so unstable that the overall flight behavior was unsatisfactory. Attempts to measure the damping of the oscillation in the positive C_{l_r} region were not successful, because the spiral instability, which resulted from the increase in C_{l_r}, required that the pilot apply corrective control immediately after a disturbance to prevent the model from crashing.

Qualitatively, the theory is in agreement with experimental results in that it correctly predicts the existence of stability or instability, but quantitatively the agreement is poor. The reason for this poor quantitative agreement has not been established.*

* The calculated values of the damping in the negative C_{l_r} range are not in agreement with the experimental results. Calculations were made including a constant time lag of 0.05 sec. in an effort to explain this discrepancy. These calculations were in much better agreement with the experimental results, indicating that the discrepancy between the measured and calculated values of damping may therefore be attributed, at least partly, to the effect of time lag in the stabilization device.

The flight tests showed that there was a slight improvement in the damping of the lateral oscillation when C_{l_r} was increased to 0.3, but the model became more difficult to fly despite this increase in damping. Both the calculated results and the flight-test results indicate that spiral instability occurred at a C_{l_r} value of 0.3 and became more severe as C_{l_r} was further increased. The aperiodic instability observed in the flight tests with positive C_{l_r} appeared to the pilot to be similar to the difficulty experienced with small positive values of C_{n_p} (up to 0.6). It is interesting to note from the calculations, however, that the spiral mode became unstable when C_{l_r} was increased, whereas it was the rolling mode that became less stable when C_{n_p} was increased.

It appears from these results that variation of the derivative C_{l_r} offers little hope for improving the flight characteristics of an airplane. This derivative, however, may be used to redistribute the damping between the oscillatory and spiral modes if surplus damping of the spiral mode is initially present. Preliminary calculations for this airplane have indicated that the damping obtained with C_{n_r} alone could be improved appreciably by utilizing C_{l_r} to redistribute part of the excess damping of the spiral mode to the oscillatory mode of motion.

Effect of $C_{n_{\dot{p}}}$

The possibility of increasing the damping of the lateral oscillation of airplane B through use of an artificial stabilization system sensitive to rolling acceleration and geared to the rudder was considered. This system introduces into the yawing moment equation the term

$$-(\partial N/\partial \delta_r)\ [\partial \delta_r/\partial (d^2\phi/dt_2)]\ (d^2\phi/dt^2)$$

which may be considered as an increment to the term $mk_{XZ}\ (d^2\phi/dt^2)$ in that equation. This system was investigated as a consequence of the results presented in references 5 and 6, which indicated that the product-of-inertia parameter k_{XZ} has a stabilizing effect on damping of the lateral oscillation if the principal longitudinal axis is above the flight path at the nose of the airplane. The results of reference 5 also indicated that the term involving k_{XZ} in the yawing equation was primarily responsible for the stabilizing effect. Therefore, it was believed that, if the rudder were deflected in proportion to the rolling acceleration, an improvement in damping of the lateral oscillation would result, since the aerodynamic forces produced by the movement of the rudder would have the same effect as increasing the value of k_{XZ} in the yawing-moment equation. The parameter added to yawing-moment equation may be expressed in nondimensional stability derivative form as $-(1/4)C_{n_{\dot{p}}}D_b{}^2\phi$.

The effect on the stability of the lateral modes of motion as the parameter $C_{n_{\dot{p}}}$ is increased from 0 to -0.08 is presented in Fig. 8. The damping of the lateral oscillation increases rapidly as $C_{n_{\dot{p}}}$ is increased,

but the period becomes increasingly shorter. The spiral mode is essentially insensitive to changes in $C_{n_{\dot{p}}}$, whereas the rolling mode becomes considerably less damped as this parameter is increased. For a value of $C_{n_{\dot{r}}}$ of -0.009, the lateral oscillation has approximately the same damping as for the cases considered previously for airplane B with a C_{n_r} value of -2.0 or a C_{n_p} value of 0.6. A point of interest, however, is that the gearing ratio $|\delta_r/\dot{p}|$ necessary to obtain this value of $C_{n_{\dot{p}}}$ is of the order of 1/20 the gearing ratio required for the C_{n_r} and C_{n_p} cases.

The use of $C_{n_{\dot{p}}}$ produced good damping of the lateral oscillation, but, as will be shown later, this derivative, like some of the other derivatives, also produced undesirable effects on controllability.

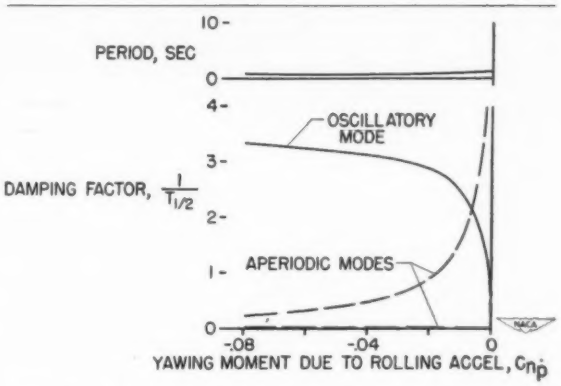

FIG. 8. Calculated effect of $C_{n_{\dot{p}}}$ on stability for airplane B.

Effect of C_{n_r}, C_{n_p}, and $C_{n_{\dot{p}}}$ on Controllability

Each of the artificial stabilization devices discussed in conjunction with airplane B appears capable of improving considerably the damping of the lateral oscillation. The acceptability of each of the devices investigated, however, would depend to a large extent on the response of the artificially stabilized airplanes. The lateral motions subsequent to application of a rolling moment coefficient of 0.01 were therefore calculated for the case of the basic airplane and for the cases of the airplane equipped with three different artificial stabilization devices. Each of these stabilizing devices increased the value of one of the following stability derivatives to the values: $C_{n_r} = -1.20$, $C_{n_p} = 0.60$, $C_{n_{\dot{p}}} = -0.005$. The motions were obtained by the conventional methods described in reference 1 and are presented in the form of time histories of the rolling and yawing velocities in Fig. 9.

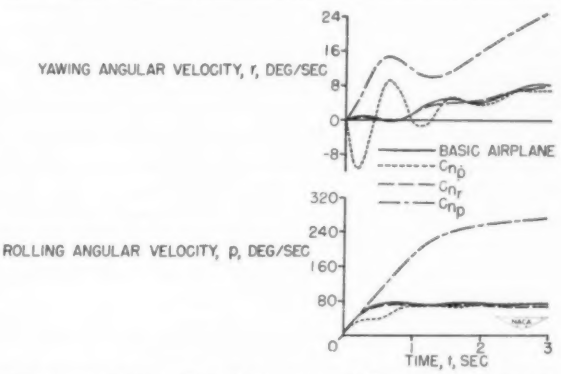

FIG. 9. Calculated effect of C_{n_r}, $C_{n_{\dot{p}}}$, and C_{n_p} on the response of airplane B to the applied rolling moment.

A comparison of the motions obtained with the basic airplane and the motions with the C_{n_r} device indicates that there is practically no change in the response characteristics. These results may appear to conflict with the previously mentioned results obtained with some full-scale airplanes equipped with yaw dampers in that no appreciable decrease in yawing velocity with increased C_{n_r} is predicted by the calculations. The results shown, however, are for an aileron rolling maneuver, and, consequently, the stiffness in yaw should not be expected to be as evident as in a turning maneuver.

With the C_{n_p} device, there is a large increase in the rolling velocity which is attributed partly to the lower damping of the rolling mode and partly to the large favorable yawing motion produced by this derivative.

With the $C_{n_{\dot{p}}}$ device, there is a large adverse yawing motion that greatly reduces the rolling velocity during the initial portion of the maneuver and which apparently causes the final rolling velocity to be about the same as that for the basic condition, even though the damping of the rolling mode is less than half of that for the basic condition. It is interesting to note that C_{n_p} and $C_{n_{\dot{p}}}$, the yawing moments produced by rolling velocity and acceleration, produce opposite effects on controllability, even though both increase the damping of the lateral oscillation.

CONCLUSIONS

Although the following results do not apply directly to airplanes or flight conditions other than those investigated, it is believed that they provide a qualitative indication of the general effects of large variations of the stability derivatives:

(1) The only single derivative that provided a large increase in damping of the lateral oscillation without adversely affecting other flight characteristics was C_{n_r}. Flight tests of some full-scale airplanes, however, have indicated that even this derivative might result in unsatisfactory stiffness in turning maneuvers.

(2) Increases in C_{n_p} or C_{l_r} caused undesirable spiral tendencies before adding a substantial amount of damping to the lateral oscillation. Increases in $-C_{l_p}$ caused objectionable stiffness in roll, and increases in $-C_{n_{\dot{p}}}$ caused objectionable adverse yawing with a consequent reduction in rolling velocity in aileron rolls.

TABLE 1

Characteristics Used in Calculations for Basic Airplane Conditions

	Airplane A	Airplane B
C_L	1.00	0.23
V	169	797
Altitude	0	30,000
W/S	34.6	65.0
S	432	130
b	36	28
A	3.0	6.0
ρ	0.002378	0.000889
γ	12.50	0
μ_b	12.6	80.7
K_X^2	0.0225	0.00967
K_Z^2	0.1439	0.0513
K_{XZ}	0.010	−0.00145
η	4.68	−2.00
C_{l_p}	−0.32	−0.40
C_{l_r}	0.13	0.08
C_{n_p}	−0.07	−0.02
C_{n_r}	−0.21	−0.40
C_{Y_p}	0.31	0
C_{Y_r}	0.43	0
C_{Y_β}	−0.78	−1.00
C_{n_β}	0.206	0.250
C_{l_β}	−0.218	−0.126

(3) There are some indications that the use of combinations of derivatives such as C_{n_p} and C_{l_p} or C_{n_r} and C_{l_r} will be more satisfactory than the use of single derivatives for increasing the damping of the oscillation without impairing flight characteristics.

REFERENCES

[1] Campbell, John P., and McKinney, Marion O., *Summary of Methods for Calculating Dynamic Lateral Stability and Response and for Estimating Lateral Stability Derivatives*, N.A.C.A. T.N. No. 2409, 1951.

[2] Schade, Robert O., and Hassell, James L., Jr., *The Effects on Dynamic Lateral Stability and Controllability of Large Artificial Variations in the Rotary Stability Derivatives*, proposed N.A.C.A. T.N.

[3] Gates, Ordway B., Jr., *Theoretical Analysis of the Effect of Several Auxiliary Damping Devices on Lateral Stability and Controllability of a High-Speed Aircraft*, N.A.C.A. T.N., No. 2565, 1951.

[4] Sternfield, Leonard, *Effect of Automatic Stabilization on Lateral Oscillatory Stability of a Hypothetical Airplane at Supersonic Speeds*, N.A.C.A. T.N. No. 1818, 1949.

[5] Sternfield, Leonard, *Effect of Product of Inertia on Lateral Stability*, N.A.C.A. T.N. No. 1193, 1947.

[6] Sternfield, Leonard, *Some Considerations of the Lateral Stability of High-Speed Aircraft*, N.A.C.A. T.N., No. 1282, 1947.

Analysis of Oval Rings by Fourier Series

(*Concluded from page 592*)

[5] Wise, J., *Analysis of Circular Rings for Monocoque Fuselages*, Journal of the Aeronautical Sciences, Vol. 6, No. 11, pp. 460–463, September, 1939.

[6] Liepmann, H. P., *General Stress Analysis for Rings with One Axis of Symmetry*, Journal of the Aeronautical Sciences, Vol. 7 No. 12, pp. 509–512, October, 1940.

[7] Hoff, N. J., *Stress Analysis of Rings for Monocoque Fuselages*, Journal of the Aeronautical Sciences, Vol. 9, No. 7, pp. 245–251, May, 1942.

[8] Wang, C., and Ramamritham, S., *Stress Analysis of Non-circular Rings for Monocoque Fuselages*, Journal of the Aeronautical Sciences, Vol. 14, No. 12, pp. 707–712, December, 1947.

[9] Den Hartog, J. P., *Mechanical Vibrations*, 2nd ed., p. 19; McGraw-Hill Book Company, Inc., New York, 1940.

Investigation into the Operating Cycle of a Two-Dimensional Supersonic Wind Tunnel*

G. V. BULL†

Institute of Aerophysics, University of Toronto

SUMMARY

The operating cycle of an intermittent supersonic wind tunnel, while probably recognized, has never been defined rigorously. In this paper, the wind-tunnel operating cycle is divided into five distinct phases based on the character of the flow along the wind-tunnel axis. These phases are, in cyclic order, the nonstationary starting phase, the quasi-stationary starting phase, the stationary phase, the quasi-stationary closing phase, and the nonstationary closing phase. The first of the starting phases is treated both theoretically and experimentally for the case of the opening valve located downstream from the working section and experimentally for the case of the valve located upstream from the nozzle throat. These theoretical studies are based on an assumed wave pattern (subsequent to the breaking of the diaphragm) determined from results of shock-tube investigations and by application of an approximate theory for the solution of two-dimensional nonstationary flow problems due to Guderley. The quasi-stationary starting phase is studied theoretically by extending the stationary supersonic-subsonic jet theory in which the jet exit static pressure is less than the pressure in the region into which the jet is issuing. The theoretically postulated state of affairs during these phases is verified by obtaining experimentally a measured series of shadowgraphs and, thereby, determining the time history of the wind-tunnel starting process. The effect of condensation of water vapor on these phases is studied experimentally.

INTRODUCTION

THE STANDARD METHOD OF TREATING the theory of intermittent supersonic wind tunnels of the type shown in Fig. 1a is based on application of isentropic steady-state equations to channel flow. In this manner the state conditions at the end of the Laval nozzle (that is, in the working section) can be related to the inlet stagnation state conditions, and the Mach Number can be determined as a function of the throat-to-working-section area ratio. For any specified Mach Number, the ratio of the inlet stagnation pressure to reservoir stagnation pressure determines the horsepower requirements of the tunnel and/or the duration of supersonic flow in the working section. With no recompression downstream of the working section, the pressure ratios inlet stagnation pressure to working-section static pressure and inlet stagnation pressure to reservoir stagnation pressure would be equal. However, in practice, pressure recovery between the working section and vacuum reservoir is accomplished by means of shock phenomena, and the critical reservoir stagnation pressure (that is, the reservoir stagnation pressure that just maintains supersonic flow in the working section) is less than the inlet stagnation pressure by the amount of pressure loss (or entropy increase) through the shock system. By assuming recompression through a normal shock wave (i.e., assuming no supersonic diffuser) the required pressure ratio for any working-section Mach Number can readily be found.[1]

In this paper it is desired to consider the complete operating cycle of this type of wind tunnel and to consider in detail the starting processes.

WIND-TUNNEL OPERATING CYCLE

It is customary to divide the wind-tunnel operating cycle into three parts—viz., the starting processes, the steady-state processes, and the closing processes. For purposes of theoretical analysis it is desirable to subdivide the wind-tunnel operating cycle into phases based on the character of the flow along the tunnel axis (see Fig. 1c). With this division the operating cycle consists of five phases: (1) the nonstationary starting phase; (2) the quasi-stationary starting phase; (3) the stationary phase; (4) the quasi-stationary closing phase; and (5) the nonstationary closing phase. The nonstationary starting phase (during which flow conditions are varying with time along the whole tunnel axis) commences with the opening of the valve and terminates with choking of the Laval nozzle throat. The quasi-stationary starting phase (during which flow conditions are constant over part of the tunnel axis) commences with choking of the nozzle throat and is considered to terminate when flow conditions have become steady along the tunnel axis up to the entry throat to the vacuum reservoir. With the termination of the quasi-stationary starting phase, the tunnel operation enters the stationary phase, which is usually many orders of magnitude greater in duration than

Received January 22, 1952.

* The work presented in this paper constitutes the thesis submitted to the University of Toronto for the Degree of Doctor of Philosophy. The experimental investigations reported herein were conducted at the Institute of Aerophysics of the University of Toronto under the supervision of the Director, Dr. G. N. Patterson, and reported in their report, UTIA No. 12. The author wishes to thank Dr. Patterson for his interest and helpful suggestions throughout the course of this work. He also wishes to thank the other members of the Institute for their interest in the work, especially Dr. C. I. H. Nicholl for his assistance in electronic trouble-shooting and Dr. D. H. Henshaw for his aid with the numerical calculations. Thanks are also due to N. Tucker for preparing the figures.

† Now, Chief Aerodynamicist, Canadian Armament Research and Development Establishment, Quebec, Canada.

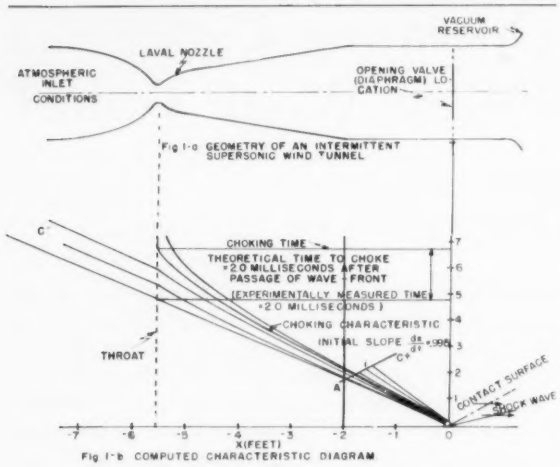

Fig 1-a GEOMETRY OF AN INTERMITTENT SUPERSONIC WIND TUNNEL

Fig 1-b COMPUTED CHARACTERISTIC DIAGRAM

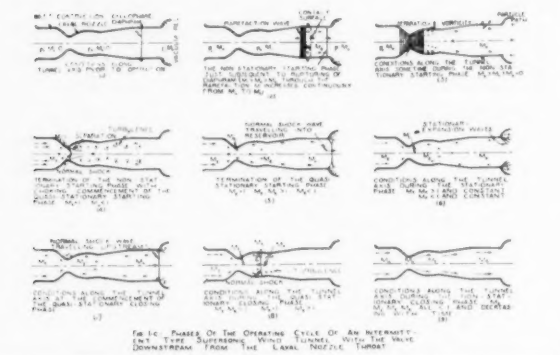

Fig 1-c PHASES OF THE OPERATING CYCLE OF AN INTERMITTENT TYPE SUPERSONIC WIND TUNNEL WITH THE VALVE DOWNSTREAM FROM THE LAVAL NOZZLE THROAT

any of the previous phases. This stationary phase is terminated when the stagnation pressure in the vacuum reservoir has risen to such a value that the flow is sonic at the entry to, and subsonic inside, the reservoir. In this case a normal shock wave appears at the entry throat, and with further rises in reservoir stagnation pressure the shock moves upstream into the working section and is finally dissipated in the nozzle throat. The quasi-stationary closing phase is considered to commence with the termination of the stationary phase and to terminate with the dissipation of the shock wave at the nozzle throat. The nonstationary closing phase is the final phase of tunnel operation during which the flow all along the tunnel axis is purely subsonic and not steady with time. This phase terminates when the stagnation conditions of the reservoir and inlet become equalized. The stationary and closing phases have been dealt with in the literature. The remainder of this paper will consider only the nonstationary starting phase and the quasi-stationary starting phase.

The Nonstationary Starting Phase

The nature of the phenomena associated with this phase depends on the location of the opening valve with respect to the throat. Hence, we must consider two possible cases.

(*1*) *Valve Located Downstream from the Throat*

If the valve is located as shown in Fig. 1a and can be assumed to open instantaneously (in practice achieved by using a cellophane diaphragm), then it is possible to treat this phase by using the shock-tube wave model[2] shown in Fig. 1b. This wave model postulates that, subsequent to rupturing of the diaphragm, a centered rarefaction wave proceeds upstream through the working section and Laval nozzle and a shock wave and contact surface proceed downstream into the vacuum reservoir. It is evident that these two phenomena will be dissipated in the vacuum reservoir and require no further consideration. Consequently, the nature of the axial distribution of flow parameters can be determined by constructing the nonstationary characteristic diagram. This construction (Fig. 1b) can be carried out using a method due to Guderley,[3] provided the flow can be assumed isentropic and that across any cross section the flow parameters are constant. Under these assumptions the equations of the characteristics may be written as. C^+,

$$\frac{1}{\rho a}\frac{dp}{dt} + \frac{du}{dt} = -au\left(\frac{d \ln F}{dx}\right) \text{ along } \frac{dx}{dt} = u + a \quad (1)$$

and C^-,

$$\frac{1}{\rho a}\frac{dp}{dt} - \frac{du}{dt} = -au\left(\frac{d \ln F}{dx}\right) \text{ along } \frac{dx}{dt} = u - a \quad (2)$$

With the tunnel geometry shown in Fig. 1a, the characteristic field bounded by the C^- characteristic OA and the C^+ characteristic through A may be treated as one-dimensional so that within this region Eqs. (1) and (2) become: C^+,

$$\lambda = \frac{2}{\gamma - 1}\left(\frac{a}{a_0} - 1\right) + \frac{u}{a_0} = \text{const. along } \frac{dx}{dt} = u + a \quad (3)$$

and C^-,

$$\mu = \frac{2}{\gamma - 1}\left(\frac{a}{a_0} - 1\right) - \frac{u}{a_0} = \text{const. along } \frac{dx}{dt} = u - a \quad (4)$$

Along the C^- characteristic OA,

$$\frac{2}{\gamma - 1}\left(\frac{a}{a_0} - 1\right) - \frac{u}{a_0} = 0$$

Along the C^+ characteristic Ai,

$$\frac{2}{\gamma - 1}\left(\frac{a_i}{a_0} - 1\right) + \frac{u_i}{a_0} = 0$$

Thus, for any point i (on OA) using the relationship for the C^- characteristic,

$$(dx/dt)_{-i} = u_i - a_i$$

we can write

$$a_i = \frac{2}{\gamma + 1} a_0 - \frac{\gamma - 1}{\gamma + 1}\left(\frac{dx}{dt}\right)_i$$

$$U_i = (dx/dt)_{-i} + a_i$$

Thus, by choosing any arbitrary slope $(dx/dt)_{-i}$ for the C^- characteristic, we can find the values of the flow parameters at i, the point of intersection of the C^+ characteristic through A, and the selected C^- characteristic. By choosing the appropriate C^- slope, we can evaluate any point on the C^+ characteristic through A. Eqs. (1) and (2) may be written in the form

$$d\lambda/dt = -(au/a_0F)\,(dF/dx)$$

$$d\mu/dt = -(au/a_0F)\,(dF/dx)$$

and then can be put in difference form

$$\lambda_C - \lambda_A = -\frac{au}{a_0F}\frac{dF}{dx}(t_C - t_A) \qquad (5)$$

$$\mu_C - \mu_A = -\frac{au}{a_0F}\frac{dF}{dx}(t_C - t_B) \qquad (6)$$

(A is a known point on a C^+ characteristic, B is a known point on a C^- characteristic, C is the point of intersection of the C^+ characteristic through A with the C^- characteristic through B.)

Using the initial conditions and applying Eqs. (5) and (6), the remainder of the characteristic diagram can be constructed by extrapolation along the characteristics; the characteristic diagram for the case investigated is presented in Fig. 1b. From this characteristic diagram it is seen that the effect of converging walls is to decrease the absolute value of the C^- characteristic slope $(dx/dt)_-$ as the characteristic is extended into the convergent duct; the slope of any such characteristic is a minimum at the throat and decreases in the divergent section. From the characteristic relationships of Eqs. (2), it is seen that u (the induced particle velocity) must increase as the characteristic proceeds into the convergent section. From energy considerations if u increases, the velocity of sound decreases and, since the flow has been assumed isentropic,

$$p = p_0(a/a_0)^{\gamma/(\gamma-1)}$$

and therefore the pressure must decrease. We can state then that each characteristic traveling upstream causes a negative pressure gradient upstream and positive pressure gradient downstream of the throat, in both cases the gradient being considered in the direction of particle travel. Consequently, separation will occur at the throat, and the induced mass flow will issue from the nozzle throat as a jet bounded by free stream lines. The gas flow contained between the tunnel walls and the free stream lines will be characterized by rotationality or vorticity. The induced mass flow is continually increasing with time. This unsteady phenomenon is termed the "nonstationary jet effect" and in

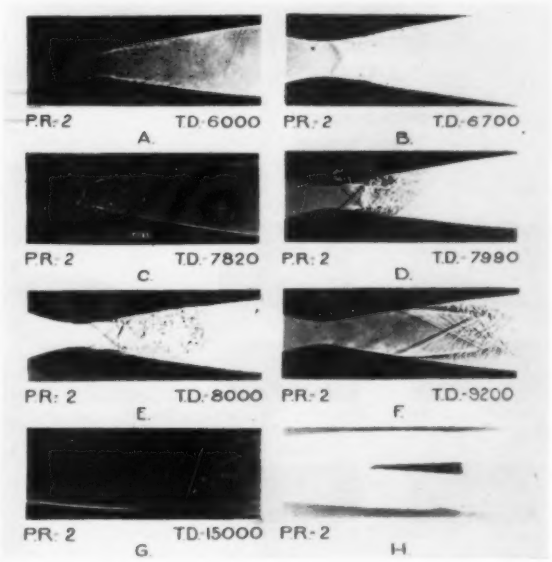

FIG. 2. Shadowgraphs of the flow in a Laval nozzle during the nonstationary and quasi-stationary starting phases with the diaphragm downstream from the throat. NOTE: P.R. is the pressure ratio across the diaphragm before rupture. T.D. is the time delay in microseconds before shadowgraph was taken.

Fig. 2a a shadowgraph taken about halfway through the nonstationary phase shows this effect in the throat of a Laval nozzle designed to produce Mach Number 2.9 flow in a 5- by 5-cm. working section. These effects are cumulative; after a small portion of the rarefaction wave has passed the velocity of sound is reached in the throat and choking occurs. Once the nozzle has choked, the pressure and particle velocity remain constant in and upstream from the throat—that is, the steady state has been reached along part of the tunnel axis so that the overall axial character of the flow may be considered quasi-stationary.

(2) *Valve Located Upstream from the Throat*

When the opening valve (or diaphragm) is located upstream from the nozzle throat, the phenomenon associated with the nonstationary phase changes from an isentropic rarefaction to a discontinuous shock phe-

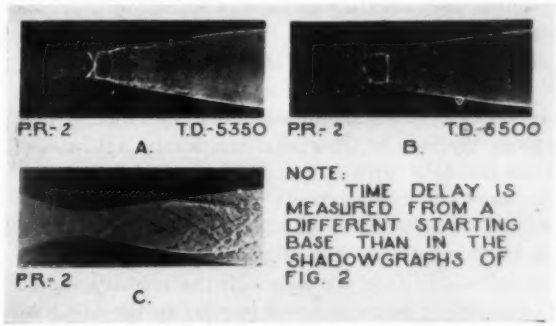

FIG. 3. Shadowgraphs showing the effect of condensation on the quasi-stationary phase.

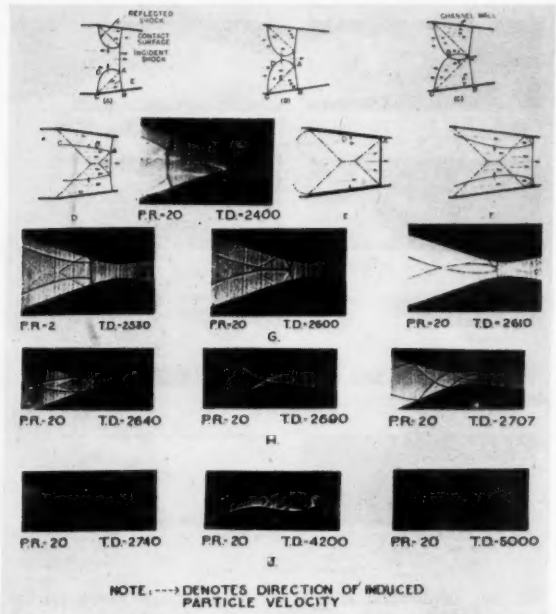

FIG. 4. Shadowgraphs of the flow in a Laval nozzle during the nonstationary and quasi-stationary starting phase with the diaphragm located upstream from the throat.

nomenon. If the valve is located in a portion of the duct with parallel walls and opens instantaneously (again achieved by the use of a cellophane diaphragm), then subsequent to opening a normal shock wave is formed[4] which travels downstream at a velocity in excess of the velocity of sound and is followed by a contact surface traveling downstream at the induced particle velocity.

When the normal shock enters the converging subsonic portion of the Laval nozzle, it will suffer a series of regular or Mach reflections depending on the initial pressure ratio. If the conditions are such that Mach reflection occurs, then the following qualitative discussion (determined experimentally) applies. The initial plane shock on entering the convergent channel suffers Mach reflection from each wall giving rise to a reflected shock and contact surface as depicted in Fig. 4a. The induced particle velocity direction is indicated neglecting any curvature of the legs of the Mach shock. It must be remembered that the contact surface represents a surface across which there is a discontinuity in the tangential velocity component, and, hence, the particle velocity vector is not necessarily parallel to this surface. In Fig. 4a the region interior to ABC is assumed constant with a flow velocity parallel to the boundary; the region exterior to the shock ACD is also assumed to be a region of constant flow, but in this case the flow velocity is parallel to the axis; the region interior to $AECD$ is one in which the velocity vector lies somewhere between being parallel to the axis and being parallel to the wall. As the initial shock travels through the converging duct, the point of reflection (the so-called triple point) moves away from the reflecting wall and the contact surface gets larger—i.e., the regions $ABCE$ and $AECD$ get larger (Fig. 4b). The triple points thus approach each other and eventually coincide (Fig. 4c). During coincidence, since perfect symmetry is assumed, a contact surface of zero strength will be generated. This condition of symmetry (coincidence of triple points) will persist for a short period of time during which the shock front will have traveled downstream. Clearly, then, a contact surface of zero strength will be generated parallel to the axis, the length of which will be determined by the magnitude of the excess forward velocity of the wave front over the relative cross velocity of the triple points. (If the wave-front velocity was equal in magnitude to the relative cross velocity of the triple points, then this zero strength contact surface would be a point.) These conditions of symmetry will be destroyed when the triple points pass through each other and continue to travel in their original direction—that is, toward the wall opposite to the one from which they originally started. This condition is shown in Fig. 4d. It should be noted in this case that, once the reflected shock ADC crosses over the axis of symmetry, it cancels out the induced particle velocity due to the wave originating at the other wall so that the flow velocity vector behind it is again parallel to the tunnel axis. When the triple points collide with the wall (Fig. 4e), inverted Mach reflection occurs and the triple points again move toward the axis of symmetry (Fig. 4f) and the process

FIG. 5.

is repeated (Fig. 4g), the number of reflections and inversions being determined by the strength of the initial shock and the length and slope of the converging walls. After the shock front passes the throat, reflection no longer occurs, but rather (as recently shown by shock tube interferograms taken at Princeton) an expansion wave causes the shock front to be curved. The reflected shock and contact phenomena break down because of dissipation beyond the throat (Fig. 4h). After the passage downstream of the initial wave front, the mass flow continues to increase (due to the rarefaction wave upstream of the throat) until choking occurs. The quasi-stationary phase is then entered.

The case of regular reflection occurring was not studied in detail; however, the results achieved indicated that this phenomenon was similar to the Mach reflection case. Some shadowgraphs for this case are presented in Fig. 5.

The Quasi-Stationary Phase

(1) *Valve Downstream from the Working Section*

During this phase, the nonstationary flow downstream from the throat will develop into stationary flow. When the induced particle velocity in the throat has attained the sonic value, stationary flow will be established here and just downstream a slight expansion will make the flow supersonic. Since there is no stable shock-free transonic deceleration, recompression must be accomplished by some shock process. From the standard theory of supersonic-subsonic jets, in which the exit static pressure of the jet is less than the region into which the jet is impinging,[5] it is seen that this shock process can consist of either a single normal shock wave or a pair of oblique shocks reflecting from a centerpoint of symmetry (cross shocks). However, reflection from the centerpoint of symmetry can occur only if the shock waves, recompressing from the exit jet pressure to the impinged region pressure and causing a flow deflection toward the axis, produce behind them a region of gas flow at a Mach Number sufficiently high to permit the existence of another shock capable of deflecting the flow back parallel to the axis. Since the Mach Number behind a shock (M_2) decreases as the shock strength increases and is always less than the Mach Number ahead of the shock (M_1), then, as M_1 approaches unity, the strength of the shock must approach unity if M_2 is to be greater than 1. But during the nonstationary phase already discussed, a finite pressure difference has already been established prior to choking. Consequently, immediately subsequent to choking, M_1 will differ only infinitesimally from unity (because of expansion adjacent to and on the downstream side of the sonic line), while a finite pressure difference will exist. Thus, reflection cannot occur from a central point of symmetry, and some form of curved normal shock (assuming the sonic line to be curved) must be formed slightly downstream from the throat just subsequent to choking. That this state of affairs exists experimentally is shown in Fig. 2b, which is a shadowgraph taken about 700 microsec. after Fig. 2a. It is evident that, after choking, the pressure downstream from the nozzle throat will start to fall because of the inequality of the fixed mass flow through the nozzle throat and the increasing mass flow into the vacuum reservoir. (The mass flow into the reservoir increases until the entry throat into the vacuum reservoir chokes.)

Thus, as the back pressure falls and approaches the pressure ahead of the shock, reflection from the central point of symmetry will occur—that is, the initial single normal shock will develop into a pair of crossed oblique shocks. The developed cross-shock pattern is shown experimentally in Fig. 2c (taken 1,100 microsec. after Fig. 2b) and Fig. 2d (taken 200 microsec. after Fig. 2c).

In Fig. 2d, the oblique shocks have rotated toward the Mach angle from the position they occupied at Fig. 2c. This is, of course, what is to be expected as the back pressure continues to fall; when the pressures on either side of the shock wave become equal, the shock becomes a Mach wave across which expansion will occur because of the divergence of the nozzle walls. Since this expansion can be considered to occur simultaneously with the equalization of pressures on either side of the shocks, the pressure on the downstream side of the expansion wave will drop below the back pressure, and, hence, at this point equilibrium is destroyed and a pair of shocks must be formed—i.e., the shock system can be considered to have moved downstream.

It is evident that this system, once established, will never depart far from equilibrium—that is, the oblique shock waves will always lie near the Mach wave. This is shown in Figs. 2d, 2e, and 2f, in which the development of the cross-shock pattern downstream can be traced. Another point, not shown experimentally but which emerges directly from this analysis, is that the rate at which the cross-shock system moves downstream depends not only on the rate of fall of back pressure but also on the rate of fall of the pressure ahead of the system due to the expanding walls. Only when the walls are parallel will the rate of development downstream depend solely on the rate of fall of back pressure. Figs. 2g and 2h show the development of the jet through the working section and the establishment of steady flow in this region.

(2) *Valve Located Upstream from the Throat*

No attempt has been made to treat this case in a theoretical fashion; however, experimentally it was observed (Fig. 4j) that, subsequent to choking, a cross-shock jet existed and developed downstream in an identical manner to that previously discussed.

The Effect of Condensation Phenomena

Condensation of water vapor due to the falling pressure and temperature does not alter the nonstationary phase discussion because the critical conditions are not reached until after choking occurs. The quasi-stationary phase is altered insomuch as, in addition to the jet shocks, there exist condensation shock waves through which some recompression is accomplished. The condensation shock phenomena occur almost simultaneously with choking, as shown in Figs. 3a and 3b, and the resultant standard X-shock pattern moves downstream into the expansion part of the nozzle as the jet develops downstream (Fig. 3c). Hermann[6] has shown the condensation phenomena in a Laval nozzle for the case of stationary flow.

Concluding Discussion

The work presented here provides an insight into the unsteady part of intermittent supersonic wind-tunnel operation. The overall picture has been established and the starting phases investigated. The division of the operating cycle into five distinct phases permits systematic treatment of the problem. It is interesting to observe that it is possible to calculate the required pressure ratio across the diaphragm prior to rupture in order to permit operation in any one of these phases. The most interesting cases are the initial diaphragm pressure ratio required to choke the nozzle throat and the initial pressure ratio required to establish supersonic flow in the working section. The latter has been dealt with previously in the literature. The initial diaphragm pressure ratio, in order to choke, can be calculated by measuring the initial slope of the choking characteristic from Fig. 1b and calculating (using this measured value) the velocity of sound and induced particle velocity on this characteristic (by the method outlined previously). Knowing these values, the shock-tube equation[7] can be solved to find the required initial diaphragm pressure ratio. For this particular case the required initial pressure ratio was calculated[8] to be 1.06. Experimental verification of this value was not achieved because of the impossibility of obtaining a diaphragm rupture at such a low pressure difference across it. (Choking was experimentally observed with an initial pressure ratio as low as 1.25.)

References

[1] Liepmann and Puckett, *Aerodynamics of a Compressible Fluid*, pp. 23–37; John Wiley & Sons, Inc., New York, 1947.

[2] Patterson, G. N., *Theory of the Shock Tube*, UTIA Report No. 2, 1948.

[3] Guderley, G., *Non-Stationary Gas Flow in Thin Pipes of Variable Cross Section*, N.A.C.A. T.M. No. 1196, 1942.

[4] Lobb, R. K., *A Study of Supersonic Flows in a Shock Tube*, UTIA Report No. 8, 1951.

[5] Ferri, A., *Elements of Aerodynamics of Supersonic Flows*, Chapt. 8; John Wiley & Sons, Inc., New York, 1948.

[6] Hermann, R., *Condensation Shock Waves in Supersonic Wind Tunnel Nozzles*, Luftfahrtforschung, Vol. 19, No. 6, pp. 201–209, June 20, 1942.

[7] See Eq. (23) of reference 2.

[8] For calculations see page 27 of *Starting Processes in an Intermittent Supersonic Wind Tunnel*, UTIA Report No. 12, February, 1951.

Changes of Address

Since the Post Office Department does not as a rule forward magazines to forwarding addresses, it is important that the Institute be notified of changes in address 30 days in advance of publishing date to ensure receipt of every issue of the JOURNAL and REVIEW.

Notices should be printed legibly and sent directly to:

Institute of the Aeronautical Sciences, Inc.

2 East 64th Street, New York 21, New York

A Review of Certain Analysis Methods for Swept-Wing Structures

M. L. WILLIAMS*

California Institute of Technology

SUMMARY

Several proposed methods for swept-wing static structural analysis are reviewed with the aim of consolidating the knowledge currently available to the structural engineer faced with the problem of a swept-wing aircraft or missile design. In addition a fairly comprehensive bibliography on swept-wing analysis is included.

Three common types of construction—stiffened sheet, solid, and thick-walled shell structures—are discussed with respect to exact and approximate solutions for deflections and stresses. The main analytical deficiencies lie in evaluating the effect of wing support conditions, particularly for the thick-skin wing.

It is concluded that, if the structure is specified and is one of the above three types, it can in most cases be analyzed by applying or extending analysis methods now available. Nevertheless, important work yet remains to be accomplished in the field of comparative design before the optimum swept-wing structure itself can be specified.

INTRODUCTION

DURING THE PAST SEVERAL YEARS, the practical importance of methods for the structural analysis of swept wings has been indicated by the growing number of papers relating to this problem. While GALCIT has been primarily concerned with the fundamental problems in thick-skin and solid-wing analysis,† it has been necessary to examine and investigate to some extent the more prevalent stiffened sheet construction. On the basis of this combined experience, it seemed desirable to review the published work in this field to date and attempt to point out the major analysis deficiencies that are believed still to exist.

While the ensuing discussion is restricted to static analysis, it is impossible to avoid the dynamic effects that are closely allied to the deformation of the structure. In previous years, the structural engineer was primarily concerned with strength, whereas, at the present time, deflection criteria are becoming of such importance for the structures that operate in the region where swept wings might be used that, often, the importance of strength criteria becomes secondary. In some of the the most recent designs based on deformation design, the structure has been operating at as low as 50 per cent of the permissible 1.0g design load from a strength standpoint. Therefore, while the important field of dynamic analysis as such is omitted, this paper will consider static analysis methods for both deformation and strength with respect to three types of wing structures: (1) stiffened sheet, (2) solid sections, and (3) thick-walled shell structures.

Presented at the Structures Session, Twentieth Annual Meeting, I.A.S., New York, January 28–31, February 1, 1952.

* Assistant Professor, Guggenheim Aeronautical Laboratory.

† It is a pleasure to acknowledge the Air Materiel Command (U.S.A.F.) sponsorship of the GALCIT investigations in this field under W-33-038-ac-16961, administered by the Aircraft Laboratory, Wright-Patterson Air Force Base.

STIFFENED SHEET CONSTRUCTION

One of the first authors to consider the problem of a skewed sheet element with stringers was S. Levy,[1] who in 1947 included such a case as one of his illustrative examples in a basic paper dealing with the application of energy methods to the finding of influence coefficients in stiffened sheet structures. In Levy's approximation of the energy in a skewed panel, it was assumed that the axial component of the edge shear, when resolved to an equivalent rectangular panel, contributed to the sheet energy. Islinger[2] pointed out that this approximation violated the assumption that the thin sheet carried only shear stresses; he proposed, for the case of sheet supported by stringers, that the axial force be divided between the stringers and, hence, contribute to the energy of the stringers. This modification was found to agree well with test data.

Levy's method has been extended and applied by the McDonnell Aircraft Corporation in two reports by Islinger[2] and Goran and Goetsch[3] and by Bisplinghoff and Lang,[4, 5] of the Massachusetts Institute of Technology Aeroelastic Laboratory. Either method leads to sets of simultaneous equations which can be handled in a manner fairly satisfactory for practical applications to a specified structure. One of the more interesting results of the Lang-Bisplinghoff paper[5] is shown in Figs. 1 and 2, where the effect of sweep angle on tip deflection, rotation, and rear spar stress is indicated.

A second approach has been proposed by Bisch,[6, 7] who has set up the general equations for the consistent deformations of an arbitrarily shaped wing in terms of many tetrahedral panels. The solution hinges upon solving very large numbers of simultaneous equations by automatic calculating equipment and, in its present stage, is probably not suited for engineering application.

Dixon[25] has recently presented an analysis of swept and unswept wing structures which is based upon a direct numerical solution of the partial differential equations governing the elastic behavior of orthogonal

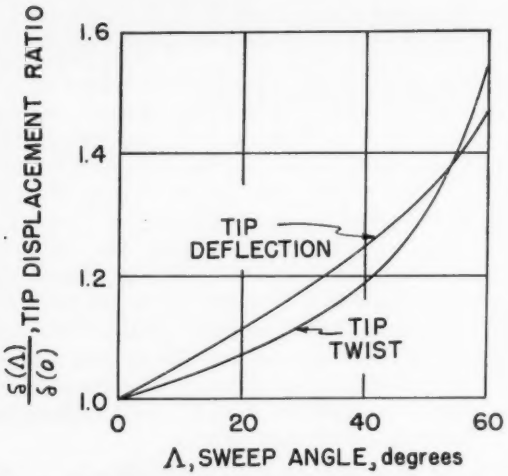

FIG. 1. Variation of tip deflection and twist with sweep angle under a tip shear load and torque for the M.I.T. experimental wing. (See Fig. 18 of reference 5.)

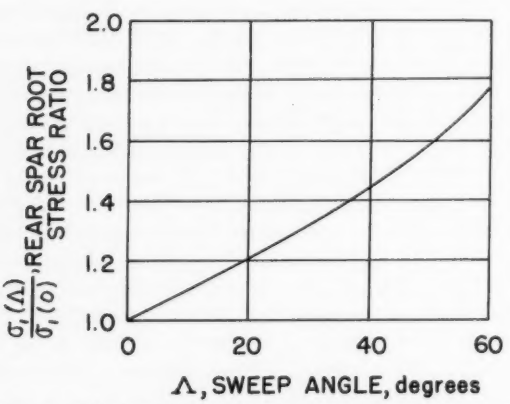

FIG. 2. Principal stress variation with sweep angle for the M.I.T. experimental wing of reference 4 under a tip shear load. (See also Fig. 17 of reference 5.)

shells. The degree of complexity of the solution depends upon the number of elements in the idealized structure. In calculating stresses and deflections to compare with N.A.C.A. experimental data,[8] Dixon applied a relaxation technique to the solution of the finite difference equations using desk calculators and considered a wing idealized to four, six, and ten spar caps or stringers. As would be expected, he found progressively better agreement with the test data, some of which are reproduced in Figs. 3 and 4. While the results were relatively easy to obtain using relaxation, especially for the four-element approximation, Dixon suggests the application of automatic calculating equipment in actual engineering applications.

Because the Dixon solution was based on the formulation of the orthogonal shell equations given by Benscoter,[9] no cutouts in the structure were considered. The method itself—i.e., working directly from the differential equation—is not invalidated, however, if the equations contain the effect of cutouts. For the cases in which it can be used, the Dixon method is thought to offer a more efficient solution for a specified structure than either the energy or consistent deformation method.

It will be noted that all of the three methods briefly discussed above have one common deficiency—they are analysis methods for a specified structure and thus have a relatively low degree of flexibility with respect to evaluating the effect of small changes in the structural configuration upon the stresses and deflections. For this reason it is desirable to have approximate methods available to evaluate the gross effects. One attempt in this direction has been proposed by D. B. Hall[10] who has treated the wing outboard of the first rib as a cantilever, thus arbitrarily reducing the redundancy to the root triangle. D. B. Hall has emphasized that his work was applied to a specific wing, and, hence, great care should be exercised in using this idea as a general approach for any arbitrary wing of any type of construction. Another simple analysis procedure has been proposed by Bisch[11] based upon a "slice" concept, in which the actual wing is represented by a series of independent spanwise beams whose end conditions are determined by the rib or support restraint at these points. While the comparison with experimental data shows only fair agreement, the method may have applications in preliminary design before the wing structure is completely defined.

There are some other experimental data available, besides those already mentioned, which may be used to check either approximate or exact theories. Zender and Libove[8] and Zender and Heldenfels[12] have reported N.A.C.A. stress and deflection data for a 45° swept box wing with a dog-leg; symmetrical and antisymmetrical bending and torsion loading were used. Grossman and Forsberg[13] obtained the stresses under symmetrical bending for a 35° half-scale swept wing.

One of the conclusions of the latter investigators, when using various combinations of tip loads, was that they found no spanwise locus of points along which there was pure bending and no torsional deflections and vice versa. While this conclusion probably depends on the wing configuration, it is nevertheless interesting in view of a relatively common assumption that an effective length or apparent elastic axis exists.

A somewhat different experimental approach has been taken by Redshaw and Palmer[14] and A. H. Hall,[15] who have tested plastic swept-wing models. The former paper is an enlightening exposition of the pitfalls of plastic experimentation. The material actually used was Xylonite, a cellulose nitrate, while Hall's work was based on a cellulose acetate. Two main difficulties were in controlling the test conditions with respect to temperature and obtaining a satisfactory value of Young's modulus and Poisson's ratio. Aside from the fact that plastic specimens may well prove to be a powerful experimental tool at comparatively low cost, certainly for qualitative investigations, the

data contained in these two reports are quite interesting. Redshaw and Palmer have found the changes in resonant mode position and frequency with variation in fuel load in the wings. Agreement of the fundamental mode and frequency for the model agreed well with the full-scale wing. A. H. Hall confined his work mainly to the static loading of the structure, a 45° built-up swept cantilever box section, and furnishes additional evidence (e.g., references 2 and 3) that wing rib orientation affects the stress and deflection distribution very little. One of Hall's main objectives was to verify the validity of plastic experimentation before extending his efforts to dynamic loadings. These two papers are strongly recommended to experimental structural engineers.

In concluding this abbreviated discussion relating to stiffened sheet construction, it appears that adequate basic analysis methods exist for swept wings if the structure is specified. Two major deficiencies arise. (1) It is often difficult to apply a given analysis method to a practical structure, one with cutouts being a typical example. (2) A simple way of evaluating the changes in deflection and stress due to a small structural modification is needed. At the present time, it appears that, at least, methods of swept-wing analysis for stiffened sheet construction are now at about the same stage of development as those for unswept wing structures.

Solid Sections

In the field of solid wing sections of varying chord and thickness distributions, the majority of the published work has been concentrated upon the cantilever plate problem for a specimen having a constant chord and uniform thickness. As in most analysis problems, the solutions that have been tried vary from exact to approximate representations of the physical behavior. A short discussion of the various methods will first be given and will then be followed by a quantitative comparison of the various theories and experimental data.

Exact Solutions

Some of the first work was done by Fung[16, 17] and concurrently by Young,[55] with the former author extending the formulation to the swept configurations. Their procedure, as reported earlier,[41] consisted of expanding the deflection function in a product series made up of a linear combination of the normal modes of free-free and clamped-free beams. The coefficients were determined following the Rayleigh-Ritz procedure. Fung concluded that the method was not practical because of the slow rate of convergence of the approximating series, especially at the larger sweep angles. Nevertheless, the calculated centerline deflections given in reference 17 for the case of an end load if plotted on Fig. 5 would agree almost exactly with the experimental data up to 40° of sweep. The chordwise slopes in the air-stream direction are, however, comparatively

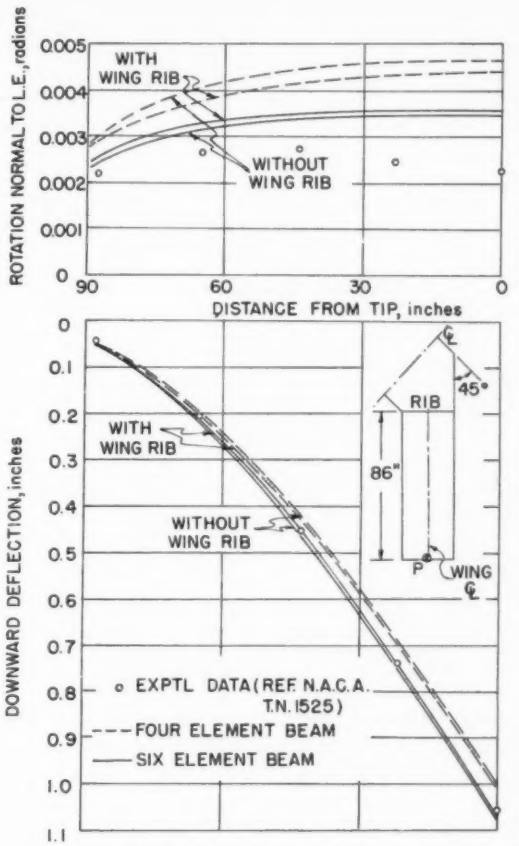

FIG. 3. Comparison of the Dixon solution for rotations and centerline deflections with the N.A.C.A. test data of reference 8.

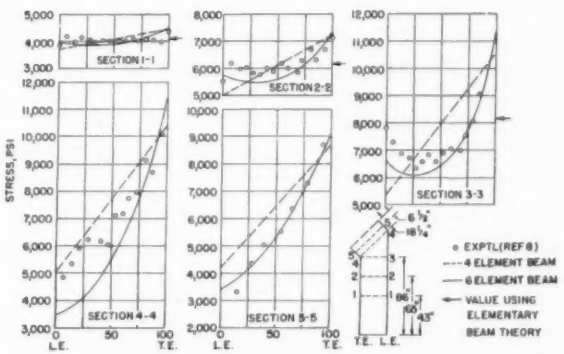

FIG. 4. Comparison of the Dixon solution for normal spanwise stresses with the N. A. C. A. test data of reference 8.

low, and the stresses are probably in further disagreement.

A sector plan form has been investigated by the author[21] following the suggestions of H. Wagner as reported by Zahorski.[39] An infinite set of exact solutions, matched to a corresponding set of infinite characteristic loading conditions for a sector plate of uniform thickness clamped along one radial edge, was ob-

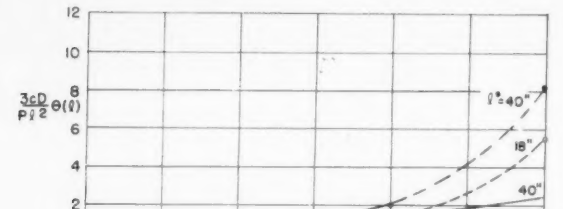

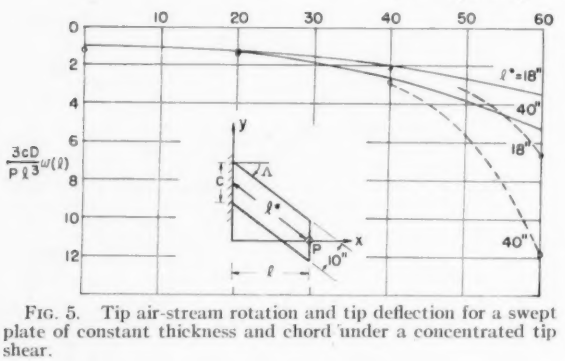

FIG. 5. Tip air-stream rotation and tip deflection for a swept plate of constant thickness and chord under a concentrated tip shear.

tained. Unfortunately, from an engineering standpoint, the inverse problem is usually posed—i.e., given some arbitrary loading, find the deflection and stresses. While it proved possible to obtain a representation of the deflection and stresses for this latter problem in terms of the infinite set of (nonorthogonal) characteristic deflection functions, the results, while of theoretical interest, are probably not easily enough applied to be of direct practical use. On the other hand, because each individual solution was exact (for the corresponding characteristic load), there was an interesting by-product believed to be of some practical importance in calculating stresses. There also seems to be some basis for extending the results to plates of variable thickness.

The primary purpose in mentioning these results at this point is to indicate the possibility of using this root-stress variation in conjunction with the Schuerch-Reissner-Stein results discussed below to save, in practical work, the necessity for a higher order approximation of the chordwise deflection. Some comparisons illustrating this point are given subsequently.

In another approach, which may possibly be termed an "exact" solution (in the sense that an orderly method for obtaining successive approximations is developed), and a method that appears powerful for obtaining the deflection of cantilever plates, Schuerch[34] derived from physical considerations a set of equations for plates of arbitrary thickness and plan form, subject to the conditions that the plate was thin and its middle plane deformed in such a manner that the chordwise deflection varied linearly.* Reissner and Stein[37] arrived at the same equations in possibly a more elegant manner by first assuming the chordwise linearity and then determining the spanwise variation by using the variational calculus upon the energy integral to obtain the governing total differential equations, which could, in many cases, be integrated directly. The Reissner and Stein approach can be extended with increasing ease to permit parabolic, cubic, or higher degree chordwise representations, while the Schuerch method is more amenable to considering a cubic variation directly, for example, without first carrying through the first- and second-order approximations. The latter physical approach is therefore of value if high-order approximation to the chordwise bending is required.

For the cases in which the linear theory was compared with existing data for swept plates of constant chord and thickness, it appears that the linear approximation gives an adequate representation of the deflection up to approximately 40° with an order of magnitude check on the root stresses. As will be illustrated shortly, certain plan forms are more favorable to the method than others, and it seems likely that at least the parabolic term will have to be employed to obtain satisfactory results for deflections of variable thickness plates with sweptback trailing edges and even a cubic term if one wishes to obtain quantitative data on the stresses by this method. This Schuerch-Reissner-Stein method (abbreviated to SRS in the ensuing comparison), with its flexibility in thickness, plan form, boundary conditions, and application to dynamic loading, offers a most promising method for attacking swept-plate structures.

A numerical solution, and exact in the limiting sense, has been proposed by Fung, who has formulated the problem as one in relaxation techniques employing the ideas of Southwell.[46] In the conventional biharmonic formulation of the cantilever plate problem, the deflection function and its derivative are specified along the clamped boundary, and higher derivative requirements (which cause the difficulty in the problem) are prescribed along the free edges. The alternative formulation introduces two new "stress" functions, U and V, which assume specified boundary values on free edges and satisfy certain relations between their first derivatives on clamped edges. The relaxation technique is fairly rapid and can be applied to arbitrary plan forms and thicknesses. As in the case of Dixon's work for the stiffened sheet construction, it suffers the usual drawbacks of numerical methods but may be adapted to certain cases such as the dog-leg structure,[24] for example, which is not easily handled by the analytical method.

* Schuerch's formulation in reference 34 is not restricted to a homogeneous thickness distribution but is developed for hollow boxes and sandwich construction. The examples worked out in references 35 and 36 are, however, for solid homogeneous plates.

Comparison of Theoretical Solutions

As an indication of the degree of accuracy obtainable with present theories, three quantities have been selected for comparison with experimental data. These are the centerline deflection, the slope in the direction parallel to the support edge (which is designated the air-stream rotation), and the stresses along the support edge (called the root stresses). It may be assumed that the degree of agreement in any of these three quantities with the experimental data gives a measure of the overall acceptability of the theoretical prediction. The major comparisons have been assembled for two plan forms—a swept rectangular plate of constant chord and thickness, and a delta plate.

In Fig. 5, the tip deflection and rotation are shown as a function of sweep angle for a specimen of constant chord and thickness. As there is an aspect ratio effect, data are shown for two values of l/c. Considering Reissner-Stein's statement that the assumption of linear chordwise deflection variation should be considered only a first approximation, the deflection is seen to be good up to approximately 40°; however, the rotations agree closely only up to 20°.

As 60° of sweep is probably the highest value of interest, the deflections and rotations have been examined spanwise in Fig. 6. In this example, both the SRS (linear) and Fung's relaxation solution are low, with the latter, while yielding a considerably closer result still underestimating the deflection and slope by approximately 20 per cent. The other curves on the graph are from approximate theories to be discussed presently.

A further comparison of the SRS (linear) theory with experimental data from reference 23 is shown in Fig. 9 for a delta plate having a varying trailing-edge angle. It is seen that, when the trailing edge is swept back, the theoretical and experimental data diverge. For this reason it is expected that at least a parabolic chordwise deflection will be required to represent the actual behavior.

One remark upon experimental technique may be mentioned at this point. It has been found that the deflection of "clamped" specimens is strongly affected by the clamping pressure. As in the case of beams, it is difficult to match the theoretical boundary conditions that are imposed on the mid-plane of the plate with the experimental boundary conditions that are imposed on the surfaces of the plate. The two become more compatible as the thickness to chord ratio decreases. This conclusion is substantiated by Ashwell[47] and Gerard[48] in their discussion of plate and beam rigidities, where it is found that plates develop their true rigidities only for large values of $\epsilon_0(c/t)^2$. (ϵ_0 is the outer fiber strains.) It will be noticed that the deflection data reported in references 18, 20, and 23 consistently lie above the theoretical predictions and, in the case of the 1-in. specimen, give somewhat higher deflections

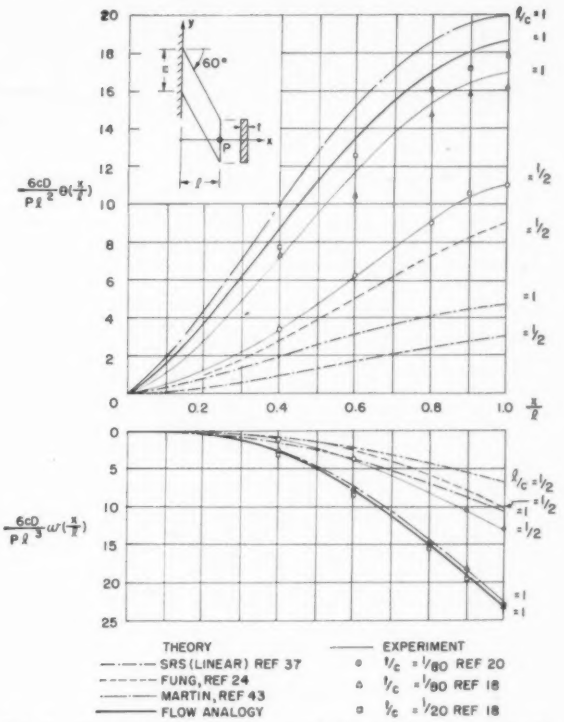

FIG. 6. Correlation of various centerline deflections and air-stream rotations for a 60° swept plate under a tip shear load.

than beam theory instead of $(1 - \mu^2)$ less which would be expected from plate theory. It was furthermore found that, as the clamping pressure was increased or the plate thickness decreased, the deflections approached the beam deflection values. The fact that, when the trailing edge is swept, the corner may yield also complicates the problem. As it may prove impossible to match the zero deflection and slope conditions exactly, theoretical data might be expected to have an inherent deficiency of up to 10 per cent of the experimental values, depending upon the thickness to chord ratio and the outer fiber strain.

Approximate Solutions

Having obtained some idea of the accuracy of the relaxation solution and the range of validity of the linear chordwise deflection assumption by examining the extreme case of 60° swept rectangular plate, some approximate theories will now be considered. The first stemmed from experimental evidence obtained by Martin and Gursahaney,[42, 43] showing for various sweep angles the existence of an apparent elastic axis for uniformly thick cantilever plates of delta and swept rectangular plan form. Recent unpublished data by Zender and Heldenfels, of the N.A.C.A., indicate that the position of the effective root varies not only with sweep angle but with aspect ratio. This latter conclusion is supported by the form of the theoretical solution of Schuerch-Reissner-Stein. The main utility of

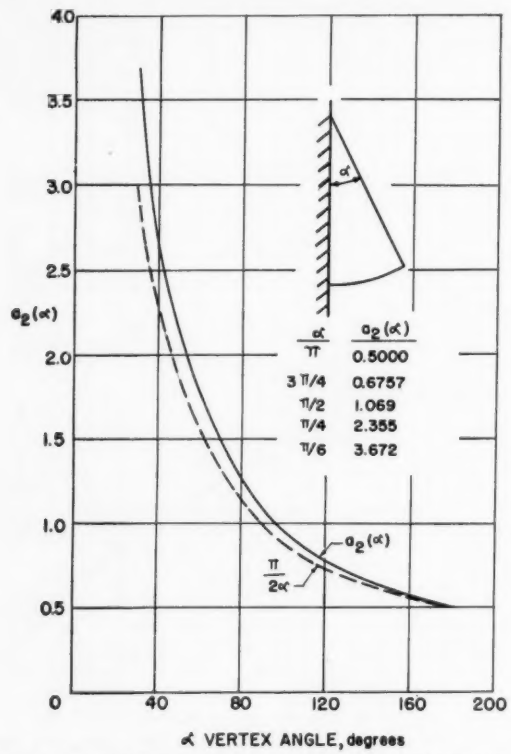

FIG. 7. Lowest eigenvalue variation with the opening angle, α.

this concept lies in its application to high aspect ratio plates, inasmuch as the deflection in the vicinity of the root when using a straight elastic axis is undefined. Using the location of the apparent elastic axis determined by a line parallel to the leading edge and intersecting the root 18 per cent forward of the trailing edge—read from Martin and Gursahaney's experimental curve (Fig. 1 of reference 43)—the deflection and air-stream rotations were calculated and plotted in Fig. 6. The results are seen to be in excellent agreement. As the method is so easy to employ, it will be particularly interesting to see whether or not an apparent elastic axis can also be found for variable thickness plates. The variation of its location with aspect ratio should also be further investigated.

A second method of approximating the deflection of swept plates arose from an intuitive approach associating the flow of stress with the flow of an incompressible fluid. That such an analogy may exist follows immediately from the two-dimensional similarity of the hydrodynamical continuity and irrotationality equations to those governing the equilibrium of an elastic solid subjected to plane stress or strain when the latter equations are written in terms of the dilitation and rotation of an element.* The connection between the extensional problems in plane elasticity to plate bending follows from the fact that the field equation is the same —the Airy stress function and the deflection function are both biharmonic. This fact was first used in a practical way by photoelasticians seeking experimental solutions to plate bending problems. Southwell[45] has recently presented a compact association of the boundary conditions in the two cases.

The basis for a consideration of the analogy stems from a somewhat different approach to the variables involved. Ordinarily, it is customary to consider two normal stresses and a shear stress on an element. Indeed, three quantities are required to determine the surface stress on a plate. Inasmuch as there are only two equilibrium equations, this means (in an approximate sense neglecting compatibility) that some additional condition must be used, such as minimizing the complementary or potential energy. Other common assumptions eliminate one of the variables by assumption, such as neglecting the cross stress (chordwise normal stress in the swept-wing case) for example. The alternative, which is suggested for certain cases, deals with three different quantities—the two principal stresses and their direction. An approximation is

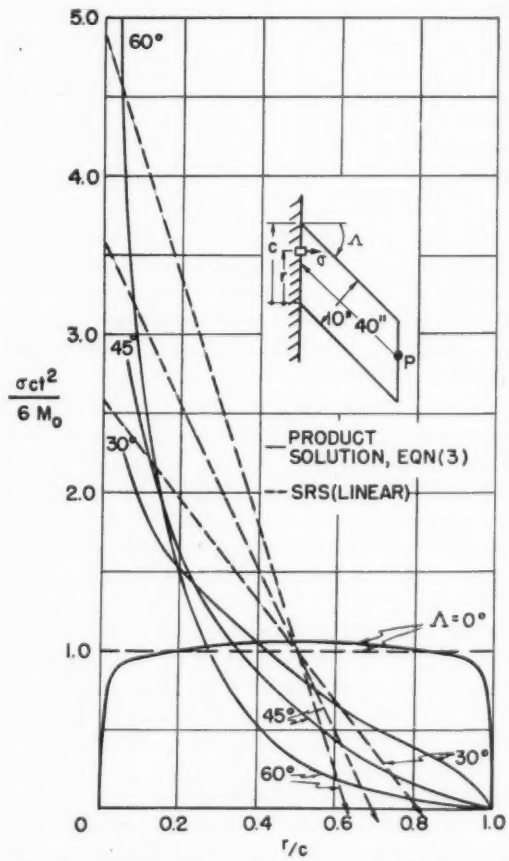

FIG. 8. Root stress variation with sweep angle for a constant chord and thickness plate under a tip shear load.

* See, for example, Hetényi, M., "On Similarities Between Stress and Flow Patterns," *Journal of Applied Physics*, Vol. 12, p. 592, 1941, where existence theorems for the analogy for two-dimensional plane stress systems are discussed.

then made to the principal stress direction. As a convenient and intuitively correct way of defining the set of orthogonal lines of principal stress directions for certain cases, the potential and stream lines of incompressible flow in a channel of the same shape as the plan form are chosen. The primary advantage gained as a direct consequence of dealing with principal stresses is that the shear stress vanishes on (curved) sections coinciding with the mesh, and, hence, the interaction of shear and normal stress is eliminated. The shear and direct bending stresses are thus separated in a convenient manner, and each individual stream line may be considered separately and treated as a curved beam. The assumption of this type of flow network is approximately equivalent to taking Poisson's ratio equal to zero and, considering each stream line as a beam, neglects the normal stress between them. However, the essential character of the curved stream lines which causes the elastic axis to move to the trailing edge has been preserved. Some additional comments and theoretical justification will be reserved until later when stresses are discussed.

The center stream line, which, in the limit, checks the zero sweep case, is then chosen as an equivalent (curved) beam and the plate forces and moments established in relation to this curved beam, using the orthogonal network to give a spanwise moment distribution from which the deflection and rotation of the equivalent beam can be obtained. The results for the 60° swept plate of constant chord and thickness are shown in Fig. 6. These check the deflection but slightly overestimate the rotation. A brief summary of the steps leading to the flow analogy solution is shown in outline form on Fig. 19. The coordinates of the center stream line for 45° and 60° swept rectangular plates and a 30°–120° delta plate are given in Fig. 20.

While not so clean a method as the SRS analytical presentation and somewhat more detailed than the apparent elastic axis of Martin and Gursahaney, it does give fairly accurate representations of stresses and deflections, including the root region and at the higher sweep angles. The major drawback is the need for reestablishing a new orthogonal mesh for each loading condition, although for cantilever plates of constant thickness this is not believed too serious for reasonable loadings. Conceptually, the method is not restricted to rectangular plan forms* and may possibly be extended to variable thickness and hollow plates and, as a final suggestion, may indicate the optimum arrangement of ribs and spars with respect to alignment in the stiffened sheet type of wing construction. It should be emphasized that, at present, it is suggested as a way of thinking and one possible means of at least semianalytical approach in the event difficulties occur

* The symmetric, tip-loaded delta plate shown in Fig. 20, for example, may be treated as a diverging channel symmetrical about the root line, with a source and sink located at opposite vertices (points of load application).

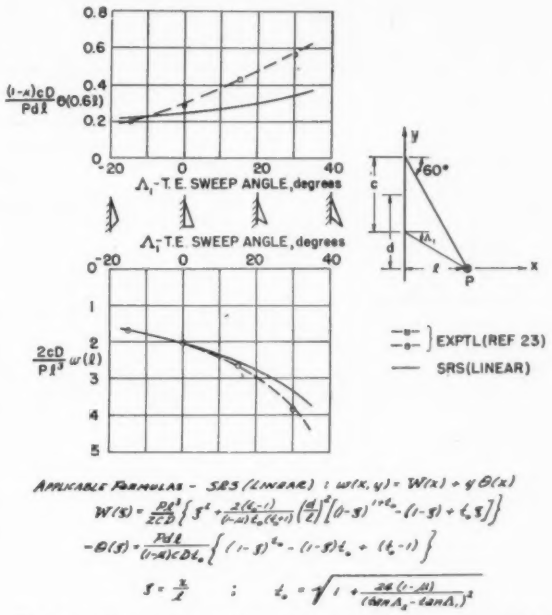

FIG. 9. Air-stream rotation and tip deflection for a variable trailing-edge delta plate of uniform thickness under a concentrated tip load. ($\Lambda_2 = 60°$.)

in other methods at the higher sweep angles. In conclusion, it should be mentioned that it may be possible to modify the straight apparent elastic axis by curving it along one of the stream lines to give better deflection, and possibly even stress, results in the root region.

Stress Formulas

It is a well-known fact that, when the deflection is approximated, the stresses calculated by differentiation are in greater error than corresponding deflection. With one exception, the previous solutions have been obtained for deflections and slopes. As may be expected, the stresses are somewhat in error. Inasmuch as deformations have recently been of considerable interest because of the aeroelastic implications, no particular emphasis has been placed on stress calculations. Nevertheless, it seems desirable also to check their accuracy.

Root stresses using the SRS (linear) theory have been calculated for a tip-loaded swept rectangular plate as a function of sweep angle and have been plotted in Fig. 8. In the notation of reference 37, the following formula applies where μ is Poisson's ratio,

$$\lambda = (l/c)\sqrt{3(1-\mu)/2}$$

and the other quantities are obvious from Fig. 5.

$$-\frac{M_x(o,\,y)}{P(l/c)} = 1 + \frac{\tan\Lambda}{1-\mu} \times \left(1 - 4\lambda\tanh 4\lambda - \frac{1}{\cosh 4\lambda}\right)\left(\frac{y}{l} - \tan\Lambda\right) \quad (1)$$

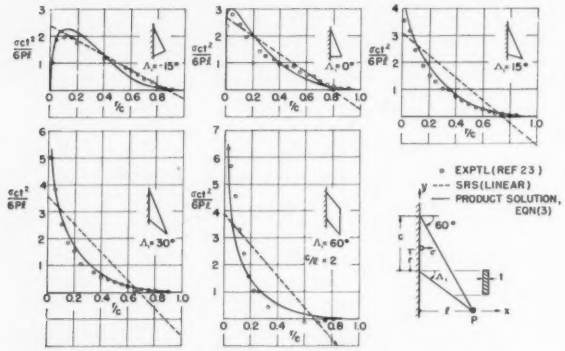

Fig. 10. Root stress variation for a constant thickness delta plate having a variable trailing-edge sweep under a tip load.

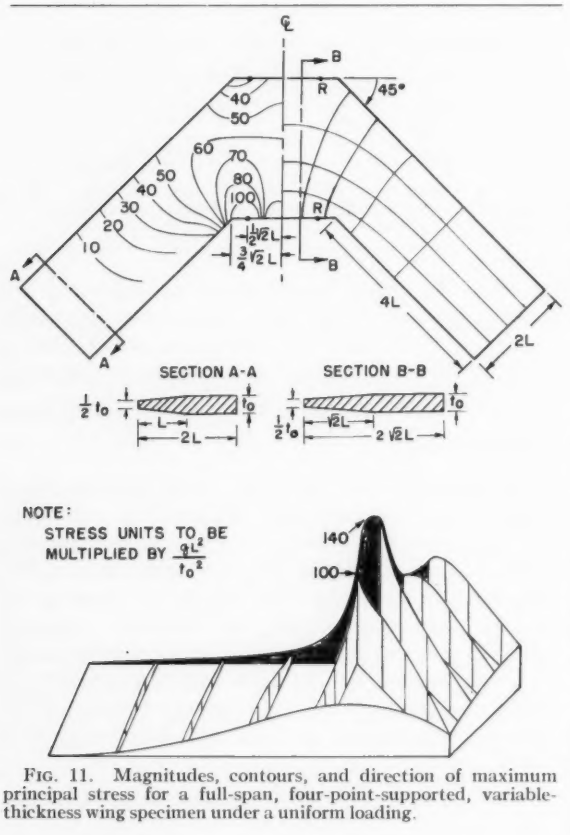

FIG. 11. Magnitudes, contours, and direction of maximum principal stress for a full-span, four-point-supported, variable-thickness wing specimen under a uniform loading.

The case of a delta plate with swept trailing edge has also been considered, and the SRS (linear) results have been plotted and compared in Fig. 10 with experimental data.[23] For reference, the SRS formulas applicable to this case are shown on Fig. 9.

The comparisons shown in Figs. 8 and 10 indicate a relatively poor correlation, and, aside from considering a parabolic (or higher) variation in the chordwise deflection, a better method for approximating the stresses is indicated. Fung[17] has given a direct approximation to the stress field by writing stress equations, containing unknown coefficients, which satisfy the equations of equilibrium of a swept rectangular plate, and then determining the constants by applying the principle of minimum complementary energy.[65] This procedure led to the stress rise curve given in reference 17 or 41, which satisfactorily estimates the gross effects. On the other hand, it is known that, for plates in bending, the stress tends to a mathematical infinity at the junction of a clamped and free edge if the enclosed angle exceeds approximately 90°.[21] Such a tendency may be noted in Fig. 10. It seems reasonable, therefore, that an estimate of the stress behavior should include this singular behavior.

In the earlier discussion dealing with the deflection of sector plates, it was noted that an infinite set of exact solutions had been found. Any of these N solutions of the plate equation which satisfy the boundary condition of zero deflection and slope along one radial edge $\theta = 0$, and zero moment and shear along the other radial edge $\theta = \alpha$, may be written in the form

$$W_n(r, \theta) = \gamma_n r^{\lambda_n(\alpha)+1} F_n[\theta; \lambda_n(\alpha)] \qquad (2)$$

where r is the distance from the vertex of the sector. Because the deflection and slope must be finite at the origin, $\lambda_n > 0$; the moment, which is directly proportional to the stress for constant thickness plates, is essentially the second derivative of the deflection, which means

$$\sigma \sim r^{\lambda_n - 1} f(\theta; \lambda_n)$$

It is then seen that, if any of the N values of λ_n are $0 < \lambda_n(\alpha) < 1$, the stress can attain mathematically infinite values at the origin. The minimum values of

$$Re\ \lambda_2(\alpha) \equiv a_2(\alpha)$$

are plotted against the vertex angle, α, in Fig. 7, and it is seen that these infinite stresses can occur if $\alpha \gtrsim 90°$. It is in this connection that further substantiation of the flow analogy arises. As can be seen in Fig. 7, the curve of $\pi/(2\alpha)$ lies close to the actual variation of $a_2(\alpha)$. The value $\pi/(2\alpha)$, however, is the exponent of the conformal transformation of rectilinear flow to flow around a corner 2α. The velocity is thus proportional to $r^{[(\pi/2\alpha)-1]}$, whereas the stress varies as $r^{a_2(\alpha)-1}$. It is then easily seen that the flow velocity becomes infinite as α exceeds 90°, which is the same tendency present in the stress.

The observation of this fact led to the postulation[40, 21] of the following approximate expression for the stresses along the root line of a uniformly thick plate of fairly arbitrary plan form:

$$\sigma_\theta(r, 0) = \frac{6M_0}{ct^2} \frac{\Gamma[a_2(\alpha_1) + a_2(\alpha_2)]}{\Gamma[a_2(\alpha_1)]\,\Gamma[a_2(\alpha_2)]} \times \left(\frac{r}{c}\right)^{a_2(\alpha_1)-1} \left(1 - \frac{r}{c}\right)^{a_2(\alpha_2)-1} \qquad (3)$$

The notation is similar to Fig. 9, where r is measured

from the vertex of the angle, $\alpha_1 \equiv \Lambda_1 + 90°$, $\alpha_2 \equiv 90° - \Lambda_2$; M_0 is the moment of the applied load on the plate about the root line; and $a_2(\alpha_i)$ is given in Fig. 7. The main restriction on the use of this expression seems to be that no large irregular loadings be imposed in the vicinity of the clamped edge. The infinity at the origin may be dealt with by cutting off the curve at the yield stress. These latter two points are more fully discussed in reference 21.

Eq. (3) was used to compute the root stress for a swept rectangular plate and for a delta plate with varying trailing-edge angle, and the results are shown in Figs. 8 and 10, respectively. In both cases it is seen that the SRS (linear) values are qualitatively correct but do not give results so close to the correct distribution as the product solution. With regard to the agreement with the experimental data of Hrebec[23] in Fig. 10, it should be noted that the product solution cannot change sign and, hence, cannot predict the negative stresses arising in the case of $\Lambda_1 = 60°$. In this sense, the formula gives a bound that is satisfactory only for single-signed stress variations. As the constant containing the Gamma functions is based upon equating the applied and reacting moments if the area under the moment curve is not made up entirely of positive contributions, an error proportional to the amount of reversed stress will result. For most loadings, this error will be slight.

In examining the experimental data, it is encouraging to see how the inclusion of the proper singular behavior aids in representing the stress variation. In particular, it should be noted that, for $\Lambda_1 < 90°$, the stress returns to zero at the origin.

Variable Thickness Plates

So far, the remarks upon solid plates have been confined to those of uniform thickness which, while of considerable theoretical interest, are not of particularly direct practical use. In this connection, the SRS solution should be most useful, because it is not restricted in thickness variation. On the other hand, it remains to be determined just what degree of approximation—linear, parabolic, etc.—will be necessary to represent the plate behavior for various thickness distributions. Some work along this line has already been carried out by Stein, Anderson, and Hedgepeth[38] for delta plates of double-wedge cross section and unswept trailing edge.

For comparison purposes, some of the N.A.C.A. data from reference 38 for the 45° delta has been reproduced in Figs. 12 and 13. In the first of these the plate is of uniform thickness, while in the second a double-wedge cross section of constant thickness ratio is considered. Inasmuch as the normalizing parameter in Fig. 13 is based on the average plate thickness, these two specimens are directly comparable on a weight basis. Regarding the deflections, it is seen, first of all,

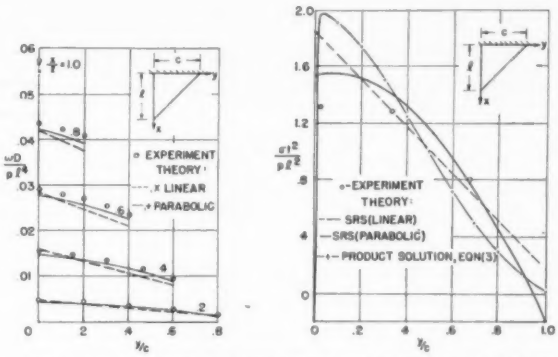

FIG. 12. Deflection and root stress variation for a 45° delta plate of uniform thickness under a uniform load. (See reference 38.)

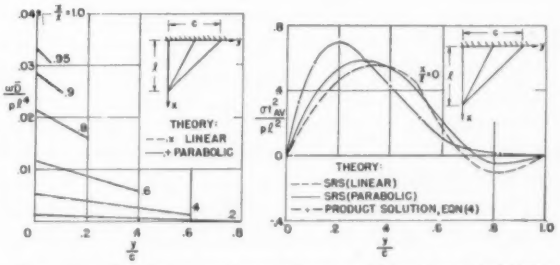

FIG. 13. Deflection and root stress variation for a 45° delta plate of double-wedge cross section under a uniform load. (See reference 38.)

that the effect of increasing the chordwise deflection approximation from linear to parabolic is small, although the effect on the rotations is somewhat more important. In the second place, the deflection of the double wedge is about two-thirds of the constant thickness section. Unfortunately, no test data are available to check the validity of the theoretical results shown in Fig. 13, although a partial check may be made using some data recorded in reference 36.

In the stresses, the change in approximation affects the distribution to a slightly greater degree, but in neither case does the approximation permit the stress to return to zero at the trailing edge. The pertinent fact to note in evaluating the effect of thickness variation is that the maximum stress for the double wedge is approximately one-third that of the constant thickness plate.

In view of the possible change in character of the stress in variable thickness plates with trailing-edge sweep angle (which fortunately is not expected to be so serious as for plates of uniform thickness), it would be extremely valuable to make a check similar to that above for double wedges of the plan forms shown in Fig. 10. Considering the surprising success of the product solution for the uniform thickness case, a semiempirical extension of its applicability to variable thicknesses was suggested for qualitative work.[30] The bending moment about the root line, M_0 $(r, 0)$, assuming the flexural rigidity,

$$(D = Et^3/12(1 - \mu^2)$$

varied according to the cube of the thickness distribution along the root line, was represented by

$$M_\theta(r, 0) = \frac{M_0}{c}\frac{\Gamma[n_1 + a_2(\alpha_1) + n_2 + a_2(\alpha_2)]}{\Gamma[n_1 + a_2(\alpha_1)]\,\Gamma[n_2 + a_2(\alpha_2)]} \times \left(\frac{r}{c}\right)^{n_1 + a_2(\alpha_1) - 1}\left(1 - \frac{r}{c}\right)^{n_2 + a_2(\alpha_2) - 1} \quad (4)$$

where, again, M_0 is the total moment of the applied load about the root line. The values of n_1, n_2 are related to the root thickness distribution in the vicinity of α_1 and α_2, respectively, such that

$$t_1(r/c, 0) \backsimeq 6\, t_{av.}\,(r/c)^{n_1/2}$$

$$t_2[(1 - r/c), 0] \backsimeq 6\, t_{av.}\,[1 - (r/c)]^{n_2/2}$$

Having the relation that

$$M_\theta(r, 0) = (1/6)\sigma_\theta\,(r, 0)t^2\,(r, 0)$$

the stress at a point along the root is obtained by dividing Eq. (4) by one-sixth the square of the local thickness at the point.

It was expected that Eq. (4) might not give so good results as Eq. (3), but, being a semiempirical relation, test data or other theoretical calculations were required to test its validity. One set of experimental root stress data* for a double-wedge section at zero sweep angle[31] indicated correlation with magnitude but not with position of maximum stress, while additional data[32] for the same specimen at 30° sweep indicated fairly satisfactory correlation in both magnitude and position. The distribution predicted by Eq. (4) was good only near the position of maximum stress, as shown in Fig. 14. For comparative purposes, the product solution has been superimposed on the N.A.C.A. data in Figs. 12 and 13 and is seen to give reasonably good agreement with the theoretical results. Experimental stress data for the double-wedge case would also be desirable.

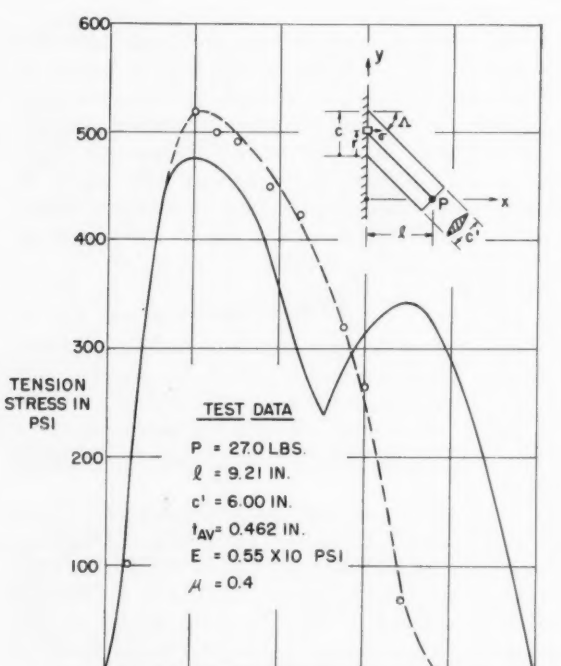

FIG. 14. Root stress variation of a constant-chord 30° swept double-wedge plastic wing under a tip shear load.

As a qualitative application of Eq. (4), the magnitude and location of maximum root stress for a cantilever double wedge of swept rectangular plan forms have been calculated, with the results shown in Fig. 14. It is important to note that double-wedge cross sections always have a finite maximum stress regardless of sweep angle. While the stresses for any thickness distribution that can be represented as a power variation of r/c can be calculated, it is probable that Eq. (4) will yield closer results for the higher sweep angles. The main utility is expected to lie in its possibility of furnishing the approximate value of the maximum stresses in the plate or wing in the event proposed theories prove too unwieldy for rapid use in preliminary design.

As a final example of dealing with swept wings idealized as solid plates of variable thickness, Fung[24] has used relaxation techniques to obtain the stress distribution in a 45° swept dog-leg full-span structure on a four-point support. The idealized wing has a constant thickness, t_0 from the leading edge back to the 50 per cent chord line and a linear taper to a thickness of $t_0/2$ at the trailing edge. The results calculated from the data in reference 24 are presented in Fig. 11 in terms of principal stress direction and magnitude. These numerical data indicate that the maximum stress occurs at the rear reaction points. The stress at the trailing-edge corner is 40 per cent lower. As this corner is formed by the intersection of two unloaded radial edges, the stress is theoretically finite,[44] and, hence, the numerical value is representative of the actual state of stress.

The relaxation technique employed by Fung is a numerical method that is not believed too cumbersome for engineering investigation and is, indeed, believed to be the only method presently available, except for electrical analog methods described below, for handling

* The data reported in references 31 and 32 were obtained from a test specimen made from a gravity castable, thermosetting plastic, Paraplex P-43, manufactured by Rohm and Haas Company, Philadelphia. This material has a fabricating advantage over most thermosetting plastics because it can be bonded to itself without the use of a dissimilar bonding agent. The joint is as strong as the parent material. Rohm and Haas and GALCIT have been cooperating in an evaluation of the use of P-43 as a structural test and/or photoelastic material. It shows promising characteristics for both purposes, and it is a pleasure to acknowledge the generous assistance and cooperation of the Rohm and Haas Company in this experimental investigation.

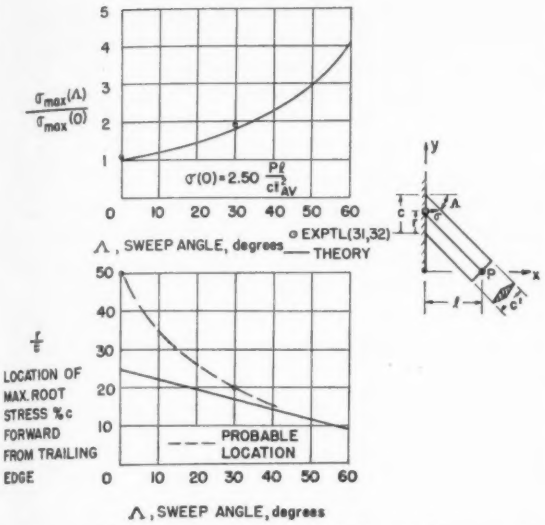

FIG. 15. Magnitude and location of the maximum stress along the root line of a swept rectangular plate of double-wedge cross section under a tip shear load.

swept plates on isolated supports. Experimental data at GALCIT to check this example are only partially complete and are not ready for presentation at this time.

One other method of solution should also be mentioned, since it may prove the most versatile for rapidly evaluating various loading conditions. It concerns the application of an electrical analog to plate problems developed by MacNeal.[19] While the method is conceptually satisfactory for plates of fairly arbitrary thickness and plan form for both static and dynamic loadings, the investigation in reference 19 was restricted by the number of high-quality transformers available. For the plate specimens simulated, however, the results were encouraging. More recent and extensive work has been carried out by the California Institute of Technology Analysis Laboratory on a delta wing. A comparison with experimental deflection tests made on a half-scale model showed favorable agreement for the static loadings investigated. Additional work sponsored by the N.A.C.A. is under way for swept and delta wings of multicell construction.

THICK-WALLED SHELL STRUCTURES

In the arbitrary division of structural types, a thick-shelled structure was not defined. A precise definition would indeed practically solve the problem of which analysis method should be used for a given structure. At the present time, however, let it suffice to class a wing structure as thick-walled if the bending stresses through the skin thickness are believed sufficiently large to be included in the analysis.

To the best of the author's knowledge, three formulations have been published for thick-walled swept shell structures. The first, given by Wan,[64] is essentially an extension of Levy's solution[1] for the stiffened sheet construction. Wan includes the bending energy of the thick sheet and computes the influence coefficients using Castigliano's theorem. The results are theoretical, and no examples are calculated. As mentioned earlier, the formulation of Schuerch includes application to both thick-walled and sandwich structures, but no extended examples were calculated in reference 34. The third solution is due to Fung[27] but has been applied only to a wing with cantilever boundary conditions. The hollow rectangular thick-walled section is analyzed as four plates rigidly joined together. The first step in the solution is to compute the stresses in the box by the conventional beam theory assuming the box to be clamped at a section normal to the spars. This fictitious root is taken normal to and at the root of the leading edge for a sweptback wing. The boundary conditions that the slope and deflection at the root of the trailing edge be zero are thus violated. To satisfy all the boundary conditions, a system of self-equilibrating forces and moments is applied at the root section (the beam is then free of constraint) and is chosen of such magnitude that it compensates the error introduced by the normal beam theory. The final stress state is obtained by a superposition.

While it is believed the latter method admits of extension, the most efficient way of handling different support conditions is not yet clear. The present formulation may, however, be adapted to multispar construction containing isolated ribs. One of the most important stress effects that has appeared in the experimental work is the relatively high chordwise stress that occurs

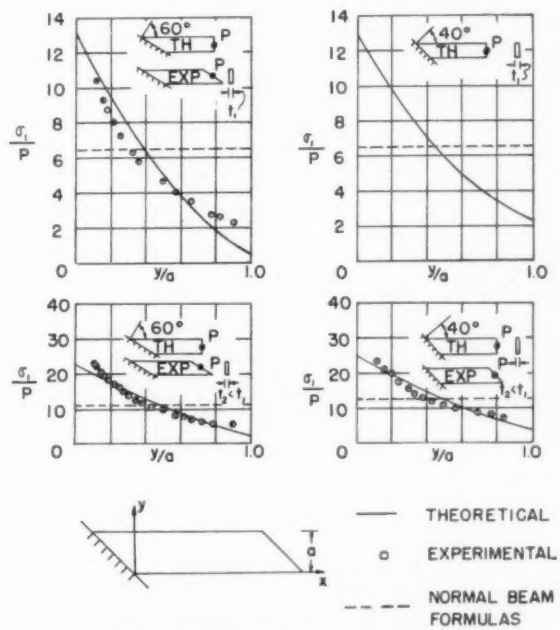

FIG. 16. Comparison of the Fung theory with certain experimental results on a hollow thick-shelled rectangular specimen showing the maximum principal stress σ_1, at the section $x = 0$ for a tip shear load.[27]

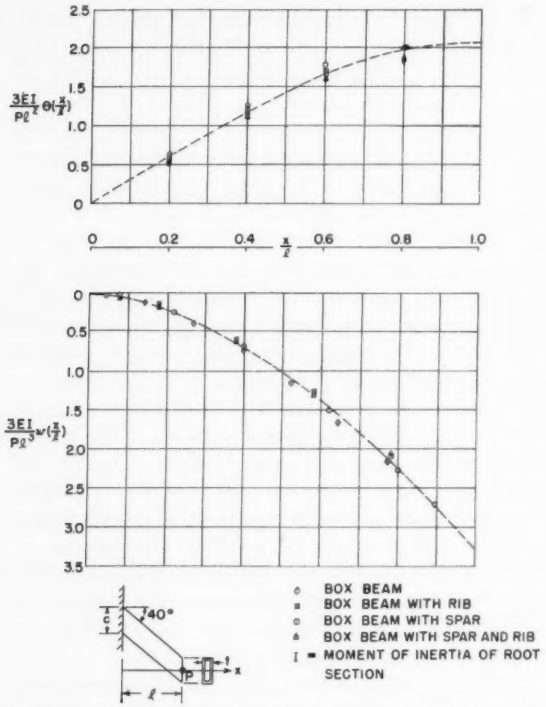

FIG. 17. Comparison of various air-stream rotations and centerline deflections for a 40° thick-walled shell specimen showing the effect of internal structural changes.

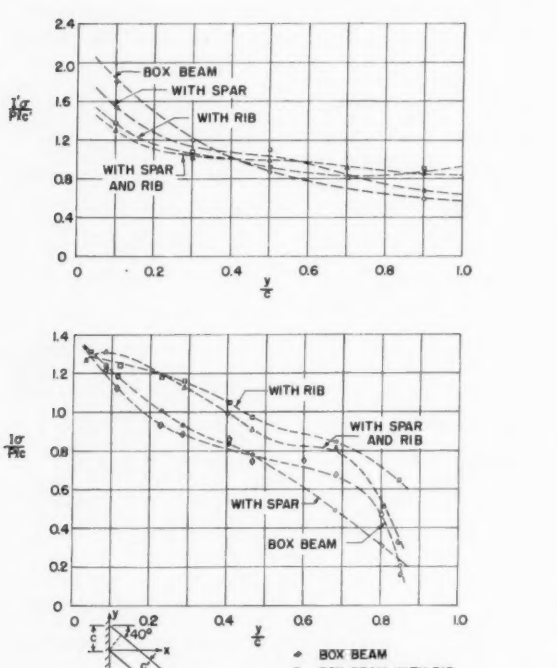

FIG. 18. Comparison of maximum principal stresses at the rib section, $x = y \tan 40°$ (*above*); at the root section, $x = 0$ (*below*), showing the effect of internal structural changes.

in the cover plate. In other words, theoretical solutions must consider bending rigidities in two orthogonal directions—not solely in the spanwise direction. As a typical illustration of the agreement with experimental data, Fig. 19 of reference 27 has been reproduced in this paper as Fig. 16. It shows the maximum principal stress due to a tip shear load for a 40° and 60° swept wing along a section (designated the rib chord) perpendicular to the leading edge and intersecting the trailing edge at the support. The basic specimen is a two-spar hollow rectangular shell with the cover plates being 1/40th of the rib chord. Two thickness ratios are shown—25 and 15 per cent overall—again based on the rib chord.

In concluding this section on heavy skin construction, attention should be drawn to Figs. 17 and 18, which show some preliminary experimental data on the effect of internal construction changes that have been extracted from reference 32. As may be seen, neither the air-stream rotation nor the centerline deflection is particularly affected by the three changes considered. Furthermore, a comparison of these normalized rotation and deflection values at the tip with the similar values for the plate specimen of Fig. 5 (40-in. length and 40° sweep angle) shows good correlation. This similarity may be important in design applications. The principal stresses across the same section as in Fig. 16 are also approximately the same in both distribution and magnitude, which is somewhat surprising, although the proper tendency is evident. One might conclude, however, that the stress rise is not reduced so much as might be expected by the addition of a spar or a rib perpendicular to the trailing edge at the root.

It is interesting to note that this small effect of a rib was also noted by Grossman and Forsberg[13] in the case of a swept wing of stiffened sheet construction.

In evaluating the effect of internal structural changes or additions upon the basis of the data shown here for rectangular box sections, it is well to remember that, aside from adding material to take the load, there is a second alternative that in many applications to swept-wing design is more important—namely, the high stress can be avoided by putting less material at the point of concentration. Two of the possible solutions, for example, are to build essentially single-spar wings or reduce the wing thickness proportional to the stress rise.

CONCLUSION

One of the obvious difficulties in writing a paper purporting to review a given subject is the sin of omission, and the author regrets any methods that have not been discussed in their proper perspective. One reason for the comparative brevity of the paper is the bibliography and critical review of swept-wing literature prepared by Sechler and Dixon[28] in the summer of 1950, from which many of the unclassified references have been taken. The main intention of the author has been

to discuss various methods that, to him, seemed the more promising from the comparative basis, because, while it seems fairly safe to conclude that there are now enough basic analysis methods available to handle with engineering accuracy the stresses and deflections in stiffened sheet, solid, and thick-walled swept-wing structures, with the possible exception of thick-walled wings with arbitrary support conditions, much remains to be done in optimizing the structure for a given flight velocity.

It is well known that sweep is a favorable aerodynamic device to employ at transonic speeds because of the drag reduction. On the other hand, after a certain amount of it on the wings of either aircraft or missiles, sweep becomes structurally inefficient from the weight and stiffness standpoint, and it again becomes desirable to build straight wings. At hypersonic speeds, wings as such may practically be omitted. Nevertheless, in the transonic region it appears that an optimizing problem should be set up, possibly as a variational problem with dual criteria—namely, that both the drag and weight be minimized simultaneously. One interim report has been written along these lines and an alternative formulation in terms of minimizing the overall work output has been prepared, but much remains to be done. The encouraging thing about the solid and thick-shelled structures is that they seem more amenable to analytical treatment, from the standpoint of investigating overall weight and stiffness variations in relative skin and spar thickness for instance, than does the conventional structure.

The foregoing review has been confined to three types of swept-wing structures, excluding sandwich construction, for example. To date, sandwich construction has been used relatively little on aircraft, although the author believes it may prove extremely efficient, in the production and economic sense, for unrecoverable pilotless missiles. It is expected that, if a satisfactory method of comparing the structural efficiency of the three types discussed herein is obtained, the sandwich-type construction will be bracketed and the proper region for its utility will be determined.

In a sense then, a very real problem remains. Even if there are sufficient separate analysis methods available to treat a specific type of construction, no analytical method yet exists, except possibly one based on Schuerch's work or the flow analogy, which permits a rapid evaluation of the relative efficiency of one type of construction against another for a given job. The proper compromise between the structural engineer's round tube and the aerodynamicist's thin plate is still unresolved.

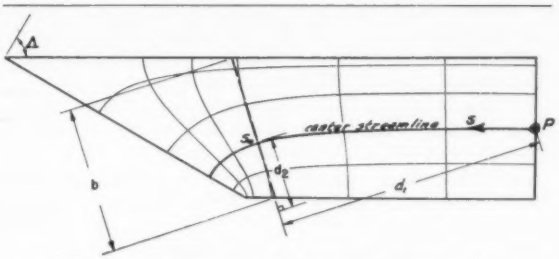

FIG. 19. A brief outline of the flow analogy method for calculating the deflection of a uniformly thick swept plate under a tip shear load.

(1) After approximating the potential lines by straight lines, determine the deflection and twist of the center streamline by numerical integration of

$$EI(s)\,[d^2\bar{W}(s)/ds^2] = M(s) = Pd_1(s) \quad (a)$$
$$GJ(s)\,[d^2\bar{\psi}(s)/ds^2] = T(s) = Pd_2(s) \quad (b)$$

using

$$I(s) = (1/12)b(s)t^3$$
$$J(s) = (\beta/3)b(s)t^3$$
$$\beta = \beta(b/t), \text{ torsion factor}$$

(2) Knowing $\bar{W}(s)$ and $\bar{\psi}(s)$, the deflection elsewhere on the plate is calculated assuming linear variation of the deflection along the (straight) potential lines.

(3) Other loadings are handled by considering strips Δs wide and resolving forces and moments to the center stream line. In the case illustrated, the distributed tip shear is considered as a concentrated load at mid-chord.

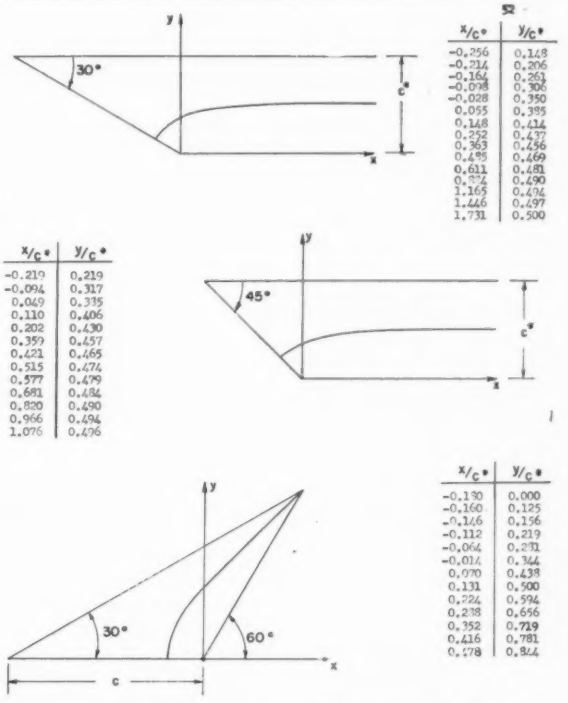

x/c *	y/c *
-0.256	0.148
-0.214	0.206
-0.164	0.261
-0.098	0.306
-0.028	0.350
0.055	0.395
0.148	0.434
0.252	0.457
0.363	0.456
0.485	0.469
0.611	0.481
0.732	0.490
1.165	0.494
1.446	0.497
1.731	0.500

x/c *	y/c *
-0.210	0.219
-0.094	0.317
0.049	0.395
0.110	0.406
0.202	0.430
0.359	0.457
0.421	0.465
0.515	0.474
0.577	0.479
0.681	0.484
0.820	0.490
0.966	0.494
1.076	0.496

x/c *	y/c *
-0.130	0.000
-0.160	0.125
-0.146	0.156
-0.112	0.219
-0.064	0.281
-0.014	0.344
0.070	0.438
0.131	0.500
0.224	0.594
0.238	0.656
0.352	0.719
0.416	0.781
0.478	0.844

FIG. 20. Location of the center stream line for certain plan forms.

REFERENCES

Stiffened Sheet Construction

[1] Levy, Samuel, *Computation of Influence Coefficients for Aircraft Structures with Discontinuities and Sweepback*, Journal of the Aeronautical Sciences, Vol. 14, No. 10, p. 547, October, 1947.

[2] Islinger, J. S., *Stress Analysis and Stress Measurements for a Sweptback Wing Having Ribs Parallel to the Airstream*, McDonnell Aircraft Corp. Report No. 1127, Serial No. 6, April, 1949.

[3] Goran, L. A., and Goetsch, G. F., *Stress Analysis of Swept-Back Box Beams Having Ribs Perpendicular to the Spars*, McDonnell Aircraft Corp. Report No. 1128, Serial No. 4, July, 1949.

[4] Bisplinghoff, R. L., and Lang, A., *An Investigation of Deformations and Stresses in Sweptback and Tapered Wings with Discontinuities for the Bureau of Aeronautics*, Mass. Inst. of Tech. [Contract No. NOa(s)-8790], July, 1949.

[5] Lang, A. L., and Bisplinghoff, R. L., *Some Results of Sweptback Wing Structural Studies*, Journal of the Aeronautical Sciences, Vol. 18, No. 11, p. 705, November, 1951.

[6] Bisch, P. E., *Determination of Stress Distribution and Rigidity of Multicell Box Structures by a General Method of Individual Panels*, North American Aviation Report No. NA 48-310, March, 1948.

[7] Bisch, P. E., *Unrestrained Torsion and Its Relations to Bending in Structures of the Box Beam Type*, North American Aviation Report No. NA 48-305, October, 1948.

[8] Zender, George, and Libove, Charles, *Stress and Distortion Measurements in a 45° Swept Box Beam Subjected to Bending and to Bending and to Torsion*, N.A.C.A. T.N. No. 1525, March, 1948.

[9] Benscoter, Stanley U., *Secondary Stresses in Thin-Walled Beams with Closed Cross Sections*, Calif. Inst. of Tech., Ph.D. Thesis, June, 1950. (Published as N.A.C.A. T.N. No. 2529.)

[10] Hall, D. B., *Method of Stress Analysis of a Sweptback Wing*, Glenn L. Martin Report No. SDR-37, October, 1947.

[11] Bisch, P. E., and Mattson, J. B., *The "Slice" Method of Box Beam Analysis as Applied to a Model Sweptback Wing*, North American Aviation Report No. NA-47-136, February, 1947.

[12] Zender, George, and Heldenfels, R. R., *Stress and Distortion Measurements in a 45° Swept Box Beam Subjected to Antisymmetrical Bending and Torsion*, N.A.C.A. T.N. No. 2054, April, 1950.

[13] Grossman, N., and Forsberg, R. H., *Experimental Stress Distributions and Deflections of a Swept Back Box Beam Subjected to Various Static Loadings*, Republic Aviation Corp. Report No. ERS-139, April, 1948.

[14] Redshaw, S. C., and Palmer, P. J., *The Construction and Testing of a Xylonite Model of a Delta Aircraft*, The Aeronautical Quarterly, Vol. II, Part II, September, 1951.

[15] Hall, A. H., *An Experimental Study of the Static Stiffness and Deformation of Swept Wings with Uniform Chord*, Proc. of the Third Anglo-American Aeronautical Conference, 1951 (R.Ae.S.-I.A.S.).

Solid and Thick-Walled Construction

The following reports, references 16 through 29, are parts of *Air Force Technical Report No. 5761*—Theoretical and Experimental Effect of Sweep Upon the Stress and Deflection Distribution in Aircraft Wings of High Solidity, prepared by the Structures Group at GALCIT. Parts 15–18 to follow.

[16] Fung, Y. C., *Part 1—Elastostatic and Aeroelastic Problems Relating to Thin Wings of High-Speed Airplanes*, February, 1949.

[17] Fung, Y. C., *Part 2—Stress and Deflection Analysis of Swept Plates*, June, 1949.

[18] DeGroff, H. M., *Part 3—Experimental Investigation of the Effect of Sweep Upon the Stress and Deflection Distribution in Cantilever Plates of Constant Chord and Thickness*, June, 1949.

[19] MacNeal, R. H., *Part 4—Application of the Electric Analog Computer to the Elastic Plate Problem*, June, 1949.

[20] Williams, M. L., *Part 5—Some Experimental Deflection Data for Uniformly Thin Swept Rectangular Cantilever Plates of Low Aspect Ratio*, October, 1950.

[21] Williams, M. L., *Part 6—The Plate Problem for a Cantilever Sector of Uniform Thickness*, June, 1950.

[22] Williams, M. L., Garrett, J., and Henry, W. E., *Part 7—An Experimental Investigation of the Stresses and Deflections in a Series of Cantilever Sectors of Uniform Thickness*, June, 1950.

[23] Hrebec, George M., *Part 8—Some Experimental Data on the Deflection and Root Stresses in a Cantilever Triangular Plate of Constant Thickness with Varying Trailing Edge Sweep Angle*, June, 1950.

[24] Fung, Y. C., *Part 9—On the Stresses in Cantilever Plates of Arbitrary Planform and Variable Thickness. (A Relaxation Procedure with Applications to the Swept Wing Problem)*, October, 1950.

[25] Dixon, Howard H., *Part 10—Stresses and Deflections of Unswept and Swept Thin-Walled Beams*, January, 1952.

[26] Williams, M. L., and Hrebec, G. M., *Part 11—An Experimental Investigation of the Stresses and Deflections in a Swept Thick-Walled Box Beam*, September, 1950.

[27] Fung, Y. C., *Part 12—On the Stresses and Deflections of Swept Thick-Walled Box Beams*, September, 1950.

[28] Sechler, E. E., and Dixon, H. H., *Part 13—Review of Analysis Methods for Swept Wing Aircraft Including a Bibliography and Abstracts of Pertinent Theoretical and Experimental References*, December, 1950 (Confidential).

[29] GALCIT Staff, *Part 14—Errata and Revisions*, November, 1950.

[30] GALCIT Staff, GALCIT 57 Progress Report No. 18 (Contract No. W-33-038-ac-16961) 1 June to 30 June, 1950. Calif. Inst. of Tech.

[31] GALCIT Staff, GALCIT 57 Progress Report No. 25 (Contract No. W-33-038-ac-16961) 1 July to 31 August, 1951. Calif. Inst. of Tech.

[32] GALCIT Staff, GALCIT 57 Progress Report No. 27 (Contract No. W-33-038-ac-16961) 1 November to 31 December, 1951.

[33] Department of Aeronautical Engineering, University of Cincinnati, *Analytical Investigations of High Solidity, Thin-Wing Designs*, Air Force Technical Report No. 5682, February, 1948.

[34] Schuerch, H. U., *Zur Statik von dunnen Flugzeug—Tragflächen*, Leemann Zurich, 1950.

[35] Schuerch, H. U., *Differential Bending Effect in Straight Thin Wing Structures of High Solidity*, Structures Memorandum No. 5 AESRL, Mass. Inst. of Tech., October, 1950.

[36] Schuerch, H. U., *Theoretical Analysis of Twist and Deflection of Swept Structures with Application to a Solid Delta Wing of Double Wedge Cross Section Subjected to Uniform Load*, Structures Memorandum No. 6 AESRL, Mass. Inst. of Tech., April, 1951.

[37] Reissner, E., and Stein, M., *Torsion and Transverse Bending of Cantilever Plates*, N.A.C.A. T.N. No. 2369, June, 1951.

[38] Stein, M., Anderson, J. E., and Hedgepeth, J. M., *Deflection and Stress Analysis of Thin Solid Wings of Arbitrary Plan Form with Particular Reference to Delta Wings*, N.A.C.A. T.N. No. 2621, November, 1951.

[39] Zahorski, A. T., *Mathematical Analysis of Cantilever Plates*, Northrop Aircraft, Inc., GM 313, Project MX 775, January, 1949.

[40] Williams, M. L., *A Simple Formula for the Root Stresses of Swept Triangular and Rectangular Cantilever Plates of Constant Thickness*, Northrop Aircraft, Inc., GM 320, October, 1949.

[41] Sechler, E. E., Williams, M. L., and Fung, Y. C., *An Initial Approach to the Overall Structural Problems of Swept Wings Under Static Loads*. Journal of the Aeronautical Sciences, Vol. 17, No. 10, p. 639, October, 1950.

[42] Gursahaney, H. J., and Martin, H. C., *An Observation Regarding the Deflections of Uniform Swept Cantilevered Plates*, Engrg. Exp. Sta. Bulletin No. 118, p. 100, University of Washington, 1951.

[43] Martin, H. C., and Gursahaney, H. J., *On the Deflection of Swept Cantilevered Surfaces*, Journal of the Aeronautical Sciences, Vol. 18, No. 12, p. 805, December, 1951.

[44] Williams, M. L., *Surface Stress Singularities Resulting from Various Boundary Conditions in Angular Corners of Plates Under Bending*, First U.S. National Congress of Applied Mechanics, Illinois Inst. of Tech., June 11, 1951.

[45] Southwell, R. V., *On the Analogues Relating Flexure and Extension of Flat Plates*, The Quarterly Journal of Mechanics & Applied Mathematics, September, 1950.

[46] Southwell, R. V., *Biharmonic Analysis as Applied to the Flexure and Extension of Flat Elastic Plates*, Phil. Trans., C, Vol. 1, pp. 15–56, 1941, or Proc. Roy. Soc. A., Vol. 239, pp. 419–460, 1945.

[47] Ashwell, D. G., *The Anticlastic Curvature of Rectangular Beams and Plates*, Jour. Roy. Aero. Soc., November, 1950.

[48] Gerard, G., *Note on Beams and Plates*, Readers' Forum, Journal of the Aeronautical Sciences, Vol. 19, No. 3, p. 207, March, 1952.

[49] Barton, M. V., Dalley, J. W., and Stuve, F. W., *Two Methods of Solving the Finite Difference Equations Used in Plate Analyses*, Defense Research Lab., The University of Texas Report No. CF-1094, DRL-180, UTX-1-AA-3, August, 1948.

[50] Barton, M. V., *Finite Difference Equations for the Analysis of Thin Rectangular Plates with Combinations of Fixed and Free Edges*, Defense Research Lab., The University of Texas Report No. CF-1005, DRL-175, UTX-1-AA-3, August, 1948.

[51] Barton, M. V., and Dalley, J. W., *Influence Coefficients for a Uniform Square Cantilever Plate with Application to the Determination of Deflections and Stresses for a Square Fin with a Pressure Distribution Corresponding to Mach Number 1.75*, Defense Research Lab., The University of Texas Report No. DRL-195, UTX-1-AA-3, January, 1949.

[52] Dalley, J. W., *Experimental Values of Deflection, Stresses and Influence Coefficients for a Thin Square Plate Fixed Along One Edge*, Defense Research Lab., The University of Texas Report No. DRL-189, UTX-1-AA-3, November, 1948.

[53] Barton, M. V., *Free Vibration Characteristics of Rectangular Cantilever Plates*, Defense Research Lab., The University of Texas Report No. CF-1258, DRL-212, UTX-1-AA-3, May, 1949.

[54] Barton, M. V., *Vibration of Rectangular and Skew Rectangular Plates Representing Idealized Missile Fins*, Defense Research Lab., The University of Texas Report No. CM-570, DRL-222, UTX-1-AA-3, December, 1949.

[55] Young, Dana, *Application of Ritz's Energy Method to Problems in the Vibration, Buckling and Bending of Rectangular Plates*, Defense Research Lab., The University of Texas Report No. CF-1265, DRL-209, UTX-1-AA-3, April, 1949.

[56] Lang, A. L., and Hallowell, F. C., Jr., *An Initial Study of Built-Up Versus Solid Wings*, Mass. Inst. of Tech. Structures Memorandums Nos. 1, 2, and 3, Project D.I.C. 6546, October, 1949.

[57] Luce, R. V., *Deflections of Cantilever Wings with Varying Geometrical Properties*, Mass. Inst. of Tech. Report No. A & R 100–40, August, 1949.

[58] Broderic, S. C., *Static Deflection Tests of MBV-3-Type Wing Surface Under Uniform Loading*, Mass. Inst. of Tech. Memorandum No. DG:S-100-2, DIC-6395, April, 1949.

[59] Benson, Albert S., and Niles, Alfred S., *Stress Relations in Oblique Coordinates*, Stanford University Technical Report No. 1, September, 1948.

[60] Benson, Albert S., and Niles, Alfred S., *Bending and Torsion of a Rhomboidal Cantilever Plate*, Stanford University Technical Report No. 2, October, 1948.

[61] Flügge, W., *Large Deflections of Thin Wings*, Stanford University Technical Report No. 3, June, 1949.

[62] Murray, Thomas R., and Niles, Alfred S., *Bending of Wide Beams of a Doubly Symmetrical Section*, Stanford University Technical Report No. 4, June, 1949.

[63] Flügge, W., *Numerical Study of a Trapezoidal Panel*, Stanford University Technical Report No. 12, June, 1949.

[64] Wan, C. C., *Calculations of Influence Coefficients for Sweptback Wings*, Chance Vought Aircraft Report RISM-1087, 1949.

[65] Sokolnikoff, I. S., *Mathematical Theory of Elasticity*, p. 286; McGraw-Hill Book Company, Inc., New York, 1946.

Library Facilities of the
Institute of the Aeronautical Sciences

To serve Institute members and others in the aeronautical industry, the Institute of the Aeronautical Sciences offers the facilities of:

The W. A. M. Burden Library

2 East 64th Street
New York 21, N.Y.

The facilities of this library are available for reference study at the Institute.

The Paul Kollsman Lending Library

2 East 64th Street
New York 21, N.Y.

This library loans books without charge to members and others in the United States over eighteen years of age. Full information will be sent on request.

The Pacific Aeronautical Library

7660 Beverly Boulevard
Los Angeles 36, Calif.

This is a service and reference library for West Coast members and organizations. Full information as to its facilities will be sent on request.

The Development of Cascade Profiles for High Subsonic Potential Flows*,†

HSUAN YEH‡

The Johns Hopkins University

SUMMARY

A method for developing cascade profiles for high subsonic potential flows to satisfy prescribed inlet and exit flow conditions and approximately prescribed cascade solidity is given. The method is based on the assumption that the compressibility of a gas can be represented by a linear pressure-volume relation (the Kármán-Tsien approximation). It is shown that with the proper selection of this pressure-volume relation, the error in specific volume in the linearized gas as compared to an isentropic gas at the same velocity is less than 2 per cent of the isentropic stagnation specific volume for Mach Numbers between approximately 0.4 to 0.9. An example shows that this Mach Number range covers almost the entire length of the cascade profile for an inlet Mach Number of 0.7 and a deflection of 22°. The deviation of the fluid angle from the blade angle at exit and the influence of inlet Mach Numbers on deviation are found to be in substantial agreement with previous experimental results.

NOMENCLATURE

a	=	location of symmetrically situated complex sources
a	=	[in Appendix (II)] local sound velocity
a_1, a_2	=	location of complex sources
a_0	=	sound velocity at stagnation of linearized gas
A, B	=	constants, strength of complex sources
c	=	chord
C	=	constant defined by Eq. (23)
C_1, C_2	=	constants defined by Eq. (17)
E	=	constant defined by Eq. (14)
F	=	$\phi + i\psi$, complex potential
$g(\zeta)$	=	mapping function in Eq. (1)
J_1, J_2, J_3, . . .	=	complex constants
K_1, K_2, K_3, . . .	=	complex constants
k	=	ratio of specific heats
L	=	leading edge
M	=	Mach Number
p	=	pressure, pitch
P	=	singularity in mapping function
q	=	velocity in the cascade plane
S	=	singularity in mapping function
T	=	trailing edge
v	=	specific volume
w	=	transformed velocity, see Eq. (8)
W	=	$we^{-i\theta}$
z	=	cascade plane
α	=	angle on the unit circle in ζ-plane
β	=	see Fig. 3
γ	=	see Fig. 1
ϵ	=	profile angle at trailing edge
ζ	=	unit circle plane
θ	=	inclination of velocity in the cascade plane
ρ	=	density
σ_1, σ_2	=	inlet and outlet flow angle, see Fig. 1
τ	=	blade exit angle, see Fig. 6

Received March 24, 1952.

* This paper is based on the first part of a Sc.D. thesis entitled "Design of Compressible Cascades" completed in July, 1950, in the Department of Mechanical Engineering, M.I.T.

† The author wishes to express his deep appreciation of the encouragement and help extended to him by Prof. E. S. Taylor, of the Gas Turbine Laboratory, M.I.T.; Prof. C. R. Soderberg, of the Department of Mechanical Engineering, M.I.T.; and Prof. C. C. Lin, of the Department of Mathematics, M.I.T. He also wishes to thank Mrs. Antonia Walker for carrying out the numerical calculations.

‡ Assistant Professor, Department of Mechanical Engineering.

INTRODUCTION

THE THEORETICAL ANALYSIS of flow through cascades has been the topic of a considerable amount of investigation. A recent survey[10] lists almost 50 articles on this subject. However, among the many papers in existence, few deal with compressible flows, so that, although both the direct and the inverse problem of an incompressible cascade can be said as more or less solved, a theory of comparable scope for compressible cascades is still lacking.

That a theory of compressible flow in cascades is important is shown by the fact that many cascades of airfoils in actual use in turbomachinery are approaching the sonic velocity, although with only a few exceptions they are still in the subsonic range.

Lin[1] first suggested that, with the assumption of a linear pressure-volume relation for a gas, the problem of generating a cascade for compressible flows could be accomplished without too much difficulty. To carry out such a process, there can be two methods of approach. One approach is to try to solve the complete "inverse" problem—namely, the finding of a profile that will give a prescribed velocity or pressure distribution along the entire profile or, if this is impossible, along a greater part of the profile. This approach is necessarily tedious, since it requires a great deal of numerical or graphical integration. Furthermore, it is by no means certain as to what is the most desirable velocity or pressure distribution. Carried to its logical conclusion, this method eventually aims at developing an ideal cascade profile.**

A second approach, which is the one used in this paper, is to find the simplest possible mapping function that will generate a cascade profile with a reasonable velocity distribution. The computational labor is thus reduced to a minimum. Although the profile obtained by this method may not be the ideal one, still, by changing the location of singularities (see below), one

** The complete "inverse" problem has been investigated by Costello, Sinnette, and Cummings.[11–13]

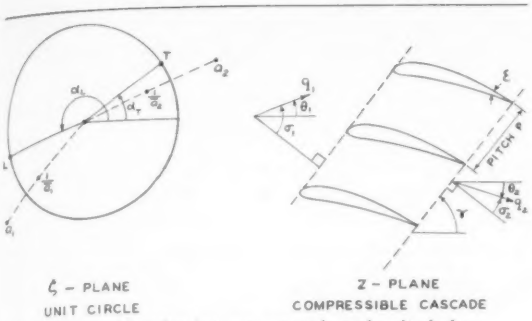

FIG. 1. Mapping between cascade and unit circle.

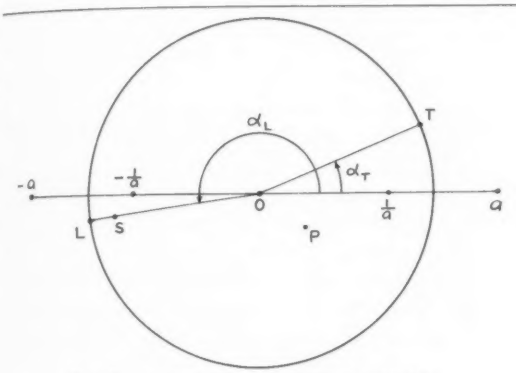

FIG. 2. ζ-plane for one family of cascades.

can obtain a vast family of cascades that may be made to approach very nearly the most desired one.

The method given in this paper, because of its ease in computation and its flexibility, might prove helpful in developing profiles for high-speed cascade testing, in which a potential flow solution is desirable as a reference for comparing actual test data, for only by comparison with a known two-dimensional potential solution can one evaluate the magnitude of the viscous and the three-dimensional effects of an actual cascade.

ANALYSIS

With the assumption of a linear pressure-volume relation (often called Kármán-Tsien approximation) for a compressible fluid, Lin[1] has shown that the transformation from an incompressible unit circle (ζ-plane) to a compressible cascade (z-plane) can be accomplished by the following functional relation:

$$dz = g(\zeta)\,(\zeta - a_1)^{-1}\,(\zeta - a_2)^{-1}\,d\zeta - \overline{(1/4a_0^2)F'^2(\zeta)\,\{g(\zeta)\}^{-1}\,(\zeta - a_1)\,(\zeta - a_2)\,d\zeta} \quad (1)$$

In this equation, $F(\zeta)$ is the complex potential function of the incompressible flow of two complex sources at $\zeta = a_1$ and $\zeta = a_2$ outside of the unit circle in the ζ-plane (Fig. 1). If A is the strength of the complex source at a_1 and B that at a_2 (A and B are complex numbers), then the function $F(\zeta)$ is represented by

$$F(\zeta) = A \log (\zeta - a_1) + \bar{A} \log [\zeta - (1/\bar{a}_1)] + B \log (\zeta - a_2) + \bar{B} \log [\zeta - (1/\bar{a}_2)] \quad (2)$$

Its derivative, or $F'(\zeta)$ in Eq. (1), is

$$F'(\zeta) = \frac{A}{\zeta - a_1} + \frac{\bar{A}}{\zeta - (1/\bar{a}_1)} + \frac{B}{\zeta - a_2} + \frac{\bar{B}}{\zeta - (1/\bar{a}_2)} \quad (3)$$

Since the strength of the source (or sink) at a_1 must be the same as the strength of the sink (or source) at a_2 so that there is no net source or sink at ∞, we must have

$$Re\,A = -Re\,B \quad (4)$$

The function $g(\zeta)$ in Eq. (1) must satisfy the following four conditions:

(a) Along the unit circle $|\zeta| = 1$,

$$\oint dz = 0 \quad (5)$$

This is the condition for closure of the profile.

(b) It is regular on and outside the unit circle, including infinity.

(c) It does not vanish on and outside the unit circle, including infinity, except at one point on the circle where, also, $F'(\zeta) = 0$; the order of the zero does not exceed 1. This point on the circle is mapped into a sharp trailing edge on the profile.

(d) The following inequality holds for the region on, and outside of, the unit circle:

$$\left|[F'(\zeta)/a_0]\,\{g(\zeta)\}^{-1}\,(\zeta - a_1)\,(\zeta - a_2)\right| < 2 \quad (6)$$

The compressible velocity field in the cascade plane is completely given by

$$W(\zeta) = we^{-i\theta} = [F'(\zeta)/g(\zeta)]\,(\zeta - a_1)\,(\zeta - a_2) \quad (7)$$

where the "distorted" velocity w is related to the true velocity q by

$$w = 2a_0 q/(a_0 + \sqrt{a_0^2 + q^2}) \quad (8)$$

For a complete background of this type of transformation, the reader is referred to references 1 to 4.

It is seen from the above discussion that, in order to complete the transformation represented by Eq. (1), our task is to find: (a) the strength of the two complex sources, or A, B; (b) the location of the two complex sources, or a_1, a_2; and (c) the function $g(\zeta)$.

Determination of A, B

In many cascade problems, the fluid inlet and exit conditions (i.e., velocity or Mach Number, and direction) are prescribed to satisfy other design requirements. Referring to Fig. 1, we are given the following quantities: σ_1, q_1, σ_2, and q_2. These quantities must, of course, satisfy among themselves the equation of continuity,

$$q_1\rho_1 \cos \sigma_1 = q_2\rho_2 \cos \sigma_2 \quad (9)$$

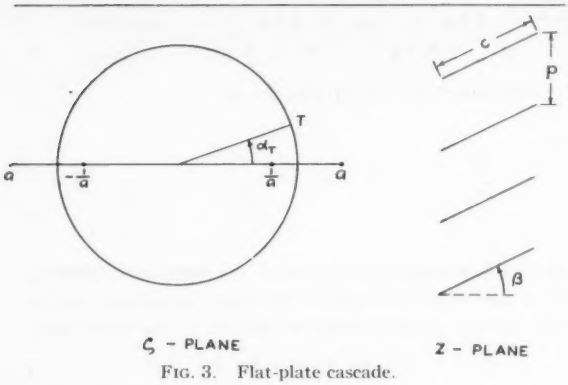

FIG. 3. Flat-plate cascade.

With q_1, q_2 given, we also have w_1, w_2, ρ_1, and ρ_2 [see Appendix (II)].

Since the points $\zeta = a_1, a_2$ transform into $z = -\infty$, $+\infty$ respectively, the velocity at $z = \pm\infty$ of the cascade can be obtained by substituting $\zeta = a_1, a_2$ into Eq. (7), which becomes

$$W_{-\infty} = w_1 e^{-i\theta_1} = A\,[(a_1 - a_2)/g(a_1)] \qquad (10)$$

$$W_{+\infty} = w_2 e^{-i\theta_2} = B\,[(a_2 - a_1)/g(a_2)] \qquad (11)$$

From these it can be shown [Appendix (I)] that

$$Im\,A/Re\,A = -(\rho_0/\rho_1)\tan\sigma_1 \qquad (12)$$

$$Im\,B/Re\,B = -(\rho_0/\rho_2)\tan\sigma_2 \qquad (13)$$

Eqs. (12) and (13), together with Eq. (4), determine the complex source strengths A and B except to a common factor. This common factor can be obtained finally by using either Eq. (10) or (11), but only after we decide on the values for a_1, a_2 and the function $g(\zeta)$.

It can be seen that, if we divide Eq. (10) by Eq. (11), we obtain

$$\frac{g(a_2)}{g(a_1)} = \frac{w_1}{w_2} e^{i(\sigma_2 - \sigma_1)} \left[\frac{1 - i(\rho_0/\rho_2)\tan\sigma_2}{1 - i(\rho_0/\rho_1)\tan\sigma_1}\right] \equiv E \qquad (14)$$

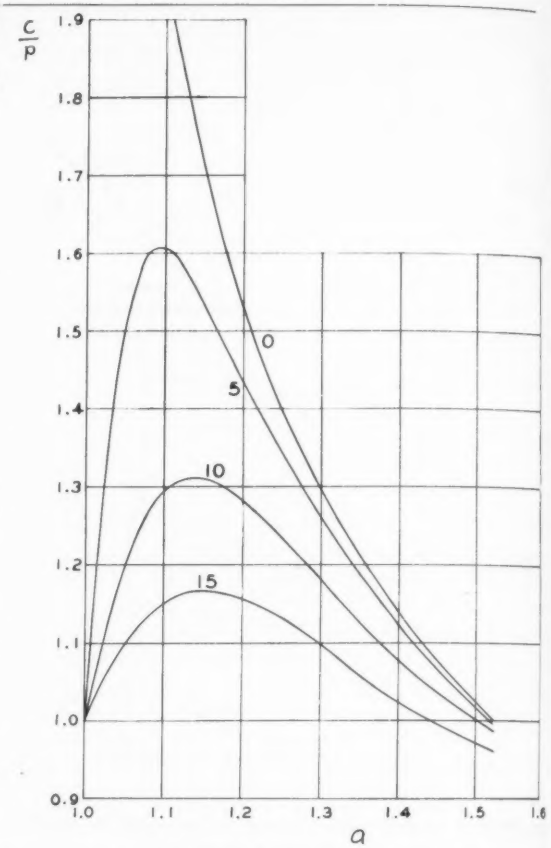

FIG. 4. Solidity for flat-plate cascade. (Numbers on curve represent α_T in degrees.)

The right-hand side of this equation consists of known quantities; hence, let it be called E. This equation therefore imposes a condition on the function $g(\zeta)$. It can be shown that Eq. (14) is identical with the condition for closure or Eq. (5).

Stagnation Points

Let the leading and trailing stagnation points be located at $\zeta = e^{i\alpha_L}$ and $\zeta = e^{i\alpha_T}$, respectively, on the unit circle (Fig. 1). From $F'(\zeta) = 0$ at these two points, we have, by Eq. (3),

$$\frac{A}{e^{i\alpha} - a_1} + \frac{\bar{A}}{e^{i\alpha} - (1/\bar{a}_1)} + \frac{B}{e^{i\alpha} - a_2} + \frac{\bar{B}}{e^{i\alpha} - (1/\bar{a}_2)} = 0 \qquad (15)$$

$\alpha = \alpha_L, \alpha_T$. Through some manipulation, Eq. (15) can be written in the following form, which has the advantage of involving only real quantities:

$$\left\{\frac{1 - |a_1|^2}{2|a_1|}\left(\frac{Im\,A}{Re\,A}\right) - \sin(\alpha - \text{Arg}\,a_1)\right\}\left\{\frac{1 + |a_2|^2}{2|a_2|} - \cos(\alpha - \text{Arg}\,a_2)\right\} -$$
$$\left\{\frac{1 - |a_2|^2}{2|a_2|}\left(\frac{Im\,B}{Re\,B}\right) - \sin(\alpha - \text{Arg}\,a_2)\right\}\left\{\frac{1 + |a_1|^2}{2|a_1|} - \cos(\alpha - \text{Arg}\,a_1)\right\} = 0 \qquad (16)$$

This equation can easily be solved for α with a few trials. One could also obtain an explicit solution for α from Eq. (15) by simply adding up the four fractions on the left side; the resulting numerator is a quadratic function of

$e^{i\alpha}$ which can be explicitly solved. Such a procedure, however, requires much manipulation with complex quantities and does not appear to be so simple as Eq. (16).

Symmetrically Situated Complex Sources

From now on, to simplify calculations, we shall restrict ourselves to a case in which the two complex sources are symmetrically located with respect to the unit circle in the ζ-plane. For such a case there is no loss of generality if, by a rotation of the axis, we further make the two complex sources fall on the real axis—that is, $a_1 = -a, a_2 = a$, with a being a real, positive quantity (Fig. 2).

Eq. (16) can now be reduced to a simple quadratic equation for $\sin \alpha$,

$$(1 + C_2^2) \sin^2 \alpha + 2C_1 \sin \alpha + (C_1^2 - C_2^2) = 0 \tag{17}$$

where C_1, C_2 are known constants,

$$C_1 = \frac{1 - a^2}{4a}\left(\frac{Im\ A}{Re\ A} - \frac{Im\ B}{Re\ B}\right), \quad C_2 = \frac{1 - a^2}{2(1 + a^2)}\left(\frac{Im\ A}{Re\ A} + \frac{Im\ B}{Re\ B}\right)$$

The two roots of Eq. (17) are α_L and α_T.

Determination of a

The value of a determines the solidity (chord/pitch ratio) of the cascade. However, the solidity is also influenced to a smaller degree by the mapping function $g(\zeta)$. It is therefore impossible to predict exactly the solidity before we have the entire mapping function. Fortunately, in most cases in practice, the solidity, unlike the inlet and exit conditions, need only have some approximate values based on previous design experience. In the present theory, an approximate solidity can be predicted by comparing the compressible cascade with an "equivalent" incompressible flat-plate cascade whose solidity can be exactly obtained.

The transformation from a unit circle (ζ-plane) to an incompressible flat-plate cascade (z-plane) is[5] (Fig. 3).

$$z = \frac{p}{2\pi}\left\{\log \frac{a + \zeta}{a - \zeta} + e^{2i\beta} \log \frac{\zeta + (1/a)}{\zeta - (1/a)}\right\} \tag{18}$$

with the solidity (chord/pitch ratio)

$$\frac{c}{p} = \frac{1}{\pi}\left\{\cos \beta \log \frac{1 + a^2 + 2a \cos \alpha_T}{1 + a^2 - 2a \cos \alpha_T} + 2 \sin \beta \tan^{-1} \frac{2a \sin \alpha_T}{a^2 - 1}\right\} \tag{19}$$

and the location of α_T

$$\tan \alpha_T = \tan \beta\ [(a^2 - 1)/(a^2 + 1)] \tag{20}$$

Eliminating β in Eq. (19) through Eq. (20), we obtain the solidity as a function of a and α_T. This is plotted in Fig. 4.

The choice of a is therefore as follows: First assume a value of a. Find α_T from Eq. (17). Experience shows that α_T is usually between 4° to 10°. Find solidity from Fig. 4. If the solidity is not what we desire, choose another a (smaller a corresponds to larger solidity and vice versa) and repeat the process until the desired a is found.

Actual calculations show that, for ordinary compressor cascades, the solidity is only 70 to 90 per cent of the solidity of the incompressible flat-plate cascade with the same a, and that the higher the Mach Number, the lower the solidity of the actual cascade, again with the same a. With this knowledge we can come closer to the desirable solidity of the actual cascade by picking an a corresponding to a solidity of a flat plate cascade that is 15 to 40 per cent greater than the desired solidity of the actual cascade.

Function $g(\zeta)$: One Family of Cascades

A simple $g(\zeta)$ function first suggested by Weinig[6] in connection with incompressible cascades is as follows:

$$g(\zeta) = \left(1 + \frac{1}{a\zeta}\right)^{-1}\left(1 - \frac{1}{a\zeta}\right)^{-1}\left(1 - \frac{S}{\zeta}\right)\left(1 - \frac{e^{i\alpha_T}}{\zeta}\right)^{1-(\epsilon/\pi)}\left(1 - \frac{P}{\zeta}\right)^{-2+(\epsilon/\pi)} \tag{21}$$

where $-a$ and $+a$ are the locations of the complex sources outside of the unit circle.

S is located on the radius to L (Fig. 2) at a distance of from 0.0125 to 0.15 from L. (Larger distance corresponds to a more blunt nose, and vice versa.) P is to be calculated in each case by Eq. (14), and ϵ is the profile angle enclosed by the trailing edge.

For this class of cascades, the mapping function is, after substituting Eqs. (21) and (3) into Eq. (1),

$$dz = \frac{(\zeta - S)\,(\zeta - e^{i\alpha_T})^{1-(\epsilon/\pi)}\zeta^2}{(\zeta + a)\,(\zeta - a)\,[\zeta + (1/a)]\,[\zeta - (1/a)]\,(\zeta - P)^{2-(\epsilon/\pi)}}\,d\zeta - \left(\frac{C^2}{4a_0^2}\right)\frac{(\zeta - e^{i\alpha_L})^2\,(\zeta - e^{i\alpha_T})^{1+(\epsilon/\pi)}\,(\zeta - P)^{2-(\epsilon/\pi)}}{(\zeta + a)\,(\zeta - a)\,[\zeta + (1/a)]\,[\zeta - (1/a)]\,(\zeta - S)\,\zeta^2}\,d\zeta \quad (22)$$

where

$$C = (B - A)a + (\bar{B} - \bar{A})\,(1/a) \quad (23)$$

The calculation of the cascade profile from Eq. (22) requires, in general, a stepwise integration. For the special case of $\epsilon = 0$, corresponding to a cusp at the trailing edge, one can easily integrate Eq. (22) as follows: Let Eq. (22) be rewritten as

$$dz = H_1(\zeta)\,d\zeta - \frac{C^2}{4a_0^2}H_2(\zeta)\,d\zeta \quad (24)$$

where

$$H_1(\zeta) = \frac{(\zeta - S)\,(\zeta - e^{i\alpha_T})\zeta^2}{(\zeta + a)\,(\zeta - a)\left(\zeta + \frac{1}{a}\right)\left(\zeta - \frac{1}{a}\right)(\zeta - P)^2} \quad (25)$$

$$H_2(\zeta) = \frac{(\zeta - e^{i\alpha_L})^2\,(\zeta - e^{i\alpha_T})(\zeta - P)^2}{(\zeta + a)\,(\zeta - a)\left(\zeta + \frac{1}{a}\right)\left(\zeta - \frac{1}{a}\right)(\zeta - S)\,\zeta^2} \quad (26)$$

are known functions of ζ. We now write

$$H_1(\zeta) = \frac{J_1}{(\zeta + a)} + \frac{J_2}{[\zeta + (1/a)]} + \frac{J_3}{(\zeta - a)} + \frac{J_4}{[\zeta - (1/a)]} + \frac{J_5}{(\zeta - P)} + \frac{J_6}{(\zeta - P)^2}$$

$$H_2(\zeta) = \frac{K_1}{(\zeta + a)} + \frac{K_2}{[\zeta + (1/a)]} + \frac{K_3}{(\zeta - a)} + \frac{K_4}{[\zeta - (1/a)]} + \frac{K_5}{\zeta} + \frac{K_6}{\zeta^2} + \frac{K_7}{(\zeta - S)}$$

where the constants J_1, J_2, J_3, J_4 can be evaluated by[7]

$$J_1 = (\zeta + a)\,H_1(\zeta), \qquad (\zeta \to -a)$$

$$J_2 = [\zeta + (1/a)]H_1(\zeta), \qquad (\zeta \to -1/a)$$

and so on, and the constants J_5, J_6 are determined by

$$J_5 = (d/d\zeta)\,[(\zeta - P)^2H_1(\zeta)], \qquad (\zeta \to P)$$

$$J_6 = (\zeta - P)^2\,H_1(\zeta), \qquad (\zeta \to P)$$

similarly for the constants $K_1, K_2, \ldots, K_7$. The following identities can serve as checks to one's calculations:

$$J_1 = g(-a)/-2a$$

$$J_3 = g(+a)/2a$$

$$K_1J_1 = A^2/C^2$$

$$K_3J_3 = B^2/C^2$$

$$J_1 + J_3 + (c^2/4a_0^2)\,(K_1 + K_3) = 0$$

$$\alpha_T + \alpha_L = 180^\circ - 2\,\mathrm{Arg}\,(C/a_0)$$

The mapping function can, for $\epsilon = 0$, be integrated as

$$z = z_1 - (C^2/4a_0^2)z_2 \quad (27)$$

where

$$z_1 = J_1 \log(\zeta + a) + J_2 \log[\zeta + (1/a)] + J_3 \log(\zeta - a) + J_4 \log[\zeta - (1/a)] + J_5 \log(\zeta - P) - J_6(\zeta - P)^{-1}$$

$$z_2 = K_1 \log(\zeta + a) + K_2 \log[\zeta + (1/a)] + K_3 \log(\zeta - a) + K_4 \log[\zeta - (1/a)] + K_5 \log\zeta - K_6\zeta^{-1} + K_7 \log(\zeta - S)$$

For the family of cascades represented by Eq. (21), the velocity at every point is given by Eq. (7), which now becomes, for any ϵ,

$$\frac{w}{a}e^{-i\theta} = \frac{C}{a_0}\frac{(\zeta - e^{i\alpha_L})(\zeta - e^{i\alpha_T})^{\epsilon/\pi}\,(\zeta - P)^{2-(\epsilon/\pi)}}{(\zeta - S)\zeta^2} \quad (28)$$

Procedure

A step-by-step procedure to generate compressible cascades with prescribed trailing-edge angle ϵ and prescribed flows at $\pm\infty$ can now be outlined as follows:

Given inlet velocity q_1/a_0, inlet angle σ_1, outlet angle σ_2 and trailing-edge profile angle ϵ. [The relation between the Mach Number of an isentropic gas and q/a_0 of a linearized gas is given in Appendix (II).]

(1) *Find* ρ_1/ρ_0, ρ_2/ρ_0, q_2/a_0, w_1/a_0, w_2/a_0 from continuity Eq. (9) and linearized gas relations of Appendix (II).

(2) *Find* $Im\,A/Re\,A$, $Im\,B/Re\,B$ from Eqs. (12) and (13).

(3) *Determine* a from the approximate solidity desired (discussed under the heading "Determination of a").

(4) *Find* α_T, α_L by Eq. (17).

(5) *Locate* P in the mapping function $g(\zeta)$ of Eq. (21). Substituting Eq. (21) into Eq. (14), we have

$$\left(\frac{-a - P}{a - P}\right)^{2-(\epsilon/\pi)}\left(\frac{a - S}{-a - S}\right)\left(\frac{a - e^{i\alpha_T}}{-a - e^{i\alpha_T}}\right)^{1-(\epsilon/\pi)} = E$$

This can be explicitly solved for the only unknown P.

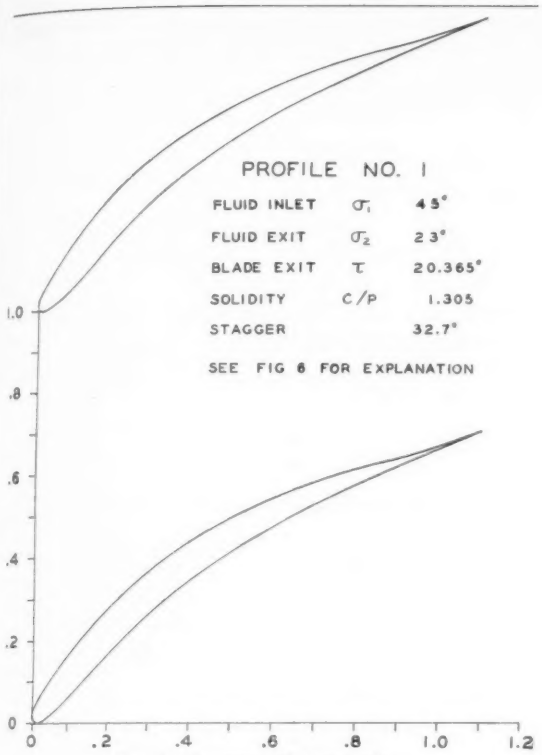

FIG. 5. Incompressible cascade.

(6) *Find* $|A|$, $|B|$ by Eqs. (10) and (11). A and B are now completely determined, since we already have $Im\,A/Re\,A$ and $Im\,B/Re\,B$.

(7) *Check* for the fulfillment of the inequality Eq. (6). This inequality becomes, for the given family of $g(\zeta)$,

$$\left|(C/a_0)\,(\zeta - e^{i\alpha_L})\,(\zeta - e^{i\alpha_T})^{\epsilon/\pi}(\zeta - P)^{2-(\epsilon/\pi)} \times (\zeta - S)^{-1}\,\zeta^{-2}\right| < 2$$

This condition is, in general, satisfied when the flow is limited to subsonic.

(8) The profile is now obtained by integrating Eq. (22). For the special case of $\epsilon = 0$, the profile is given directly by Eq. (27).

(9) The velocity distribution is given by Eq. (28).

It might be mentioned that the above procedure also applies to the incompressible cascade, which becomes an especially simple case.

Example

Two cascade profiles have been calculated using the methods developed above. In order to form a basis for comparison, both profiles are designed on the same inlet angle $\sigma_1 = 45°$ and the same exit angle $\sigma_2 = 23°$. The deflection for both profiles is therefore 22°. Also, ϵ is taken as zero for both profiles. Profile No. 1 is for the incompressible cascade and Profile No. 2 is for an inlet Mach Number of 0.7. The results can be summarized as follows:

Profile No. 1 (Fig. 5)

Solidity (chord/pitch ratio) = 1.305
Blade angle at exit = 20.365°
Deviation (fluid exit angle minus blade angle at exit) = 2.635°
Stagger = 32.7°

$$\frac{Im\,A}{Re\,A} = -1.0000, \quad \frac{Im\,B}{Re\,B} = 0.42447$$
$$\alpha_T = 4.00°, \quad \alpha_L = 189.53°$$
$$P = 0.113764 - 0.080675i$$

Profile No. 2 (Fig. 6)

Solidity = 1.086
Blade angle at exit = 20.056°
Deviation = 2.944°
Stagger = 32.1°

$$\frac{Im\,A}{Re\,A} = -1.37144, \quad \frac{Im\,B}{Re\,B} = 0.49899$$
$$\alpha_T = 4.677°, \quad \alpha_L = 193.024°$$
$$P = 0.123877 - 0.080825i$$

For both profiles, $a = 1.183$, and $S = 0.96\,e^{i\alpha_L}$. It can be noted that, with the same a, the solidity of the compressible cascade is considerably smaller than that of the incompressible cascade. One could, if one desires, bring the compressible profile nearer in solidity with the incompressible one by using a smaller value of a for the former.

The velocity distribution around the profile is shown in Figs. 7 and 8.

CONCLUSIONS AND SUGGESTIONS FOR FUTURE WORK

Although no definite conclusion can be drawn when only two cascades have been calculated so far, there are several interesting aspects worthy of mentioning.

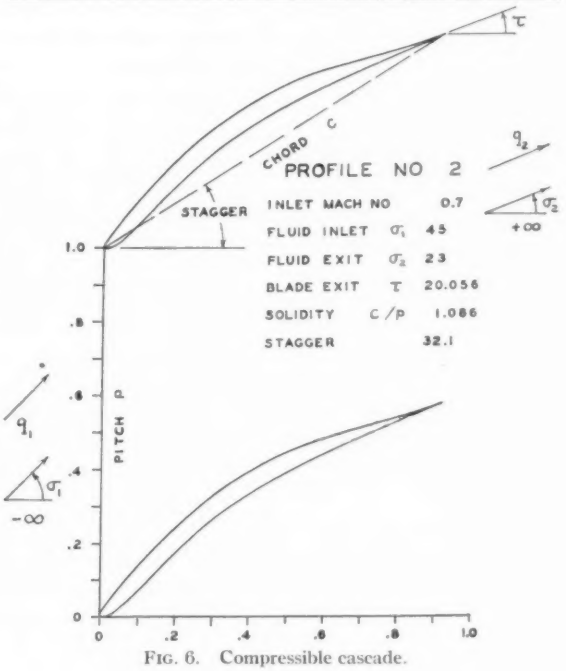

FIG. 6. Compressible cascade.

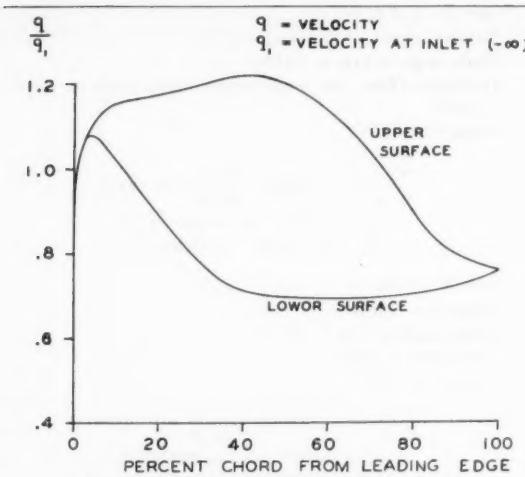

FIG. 7. Velocity distribution Profile No. 1.

The deviation, or the difference of the fluid angle from the blade angle at exit, is around 3° in both cases. Howell's[8] experimental data indicate, for this particular cascade arrangement, a deviation of about 5°. The slight discrepancy between theory and experiments on the value of deviation may be partly due to the viscous and the three-dimensional effects in experiments and partly due to the somewhat unconventional upturn of the trailing edge of the developed profile.

For the same fluid exit angle, the blade exit angle of the compressible cascade is only 0.309° larger. It appears therefore that, for a given cascade and inlet fluid angle, the influence of Mach Number on the fluid exit direction is negligible. This is also the result of experiments by Bogdonoff.[9]

The velocity distribution does not seem out of line with those of actual blades used in practice.

Future work could extend the use of this method to different flow angles, solidity, and Mach Numbers. There is also great flexibility in modifying the blade shape and therefore in improving the velocity distribution by varying the location of singularities in the function $g(\zeta)$. Specifically, one can consider the following three variations: (1) Shift the location of S in Eq. (21) by a slight amount; (2) add another factor $[1 - (Q/\zeta)]^n$ in Eq. (21), where Q is slightly away from the center of the unit circle and the exponent n is preferably ± 1 or ± 2 to facilitate computation; (3) for greater generality it might be desirable to have the two complex sources located nonsymmetrically. Other variations of $g(\zeta)$ function are, of course, also possible.

APPENDIX (I)

In the cascade plane in Fig. 1, the fluid angles at $\pm\infty$, or θ_1, θ_2, are given by Eqs. (10) and (11) or by

$$\theta_1 = -\text{Arg}\,[A(a_1 - a_2)/g(a_1)]$$
$$\theta_2 = -\text{Arg}\,[B(a_2 - a_1)/g(a_2)]$$

The angle of the cascade axis, or γ, is, by the Cauchy integral formula and by virtue of Eqs. (1) and (3),

$$\gamma = \text{Arg}\,[\oint_{(a_1)} dz] = \frac{\pi}{2} + \text{Arg} \times \left[\frac{g(a_1)}{a_1 - a_2} + \frac{1}{4a_0^2}\frac{\overline{A^2(a_1 - a_2)}}{g(a_1)}\right] = \text{Arg}\,[-\oint_{(a_2)} dz] = \frac{\pi}{2} + \text{Arg}\left[\frac{g(a_2)}{a_1 - a_2} + \frac{1}{4a_0^2}\frac{\overline{B^2(a_1 - a_2)}}{g(a_2)}\right]$$

where $\oint_{(a_1)}$ and $\oint_{(a_2)}$ represent a small closed path around the singularities a_1 and a_2, respectively.

If the fluid angles are measured from the cascade axis, then (Fig. 1)

$$\sigma_1 = \theta_1 + (\pi/2) - \gamma$$
$$\sigma_2 = \theta_2 + (\pi/2) - \gamma$$

Substituting the expressions for θ_1, θ_2, and γ

$$\sigma_1 = -\text{Arg}\left[A + \frac{1}{4a_0^2}\left|\frac{A(a_1 - a_2)}{g(a_1)}\right|^2 \bar{A}\right]$$

$$\sigma_2 = -\text{Arg}\left[-B - \frac{1}{4a_0^2}\left|\frac{B(a_2 - a_1)}{g(a_2)}\right|^2 \bar{B}\right]$$

However, from Eqs. (10) and (11),

$$w_1 = \left|\frac{A(a_1 - a_2)}{g(a_2)}\right|, \quad w_2 = \left|\frac{B(a_2 - a_1)}{g(a_2)}\right|$$

Hence,

$$-\tan\sigma_1 = \frac{1 - (w_1^2/4a_0^2)}{1 + (w_1^2/4a_0^2)}\left(\frac{Im\,A}{Re\,A}\right)$$

$$-\tan\sigma_2 = \frac{1 - (w_2^2/4a_0^2)}{1 + (w_2^2/4a_0^2)}\left(\frac{Im\,B}{Re\,B}\right)$$

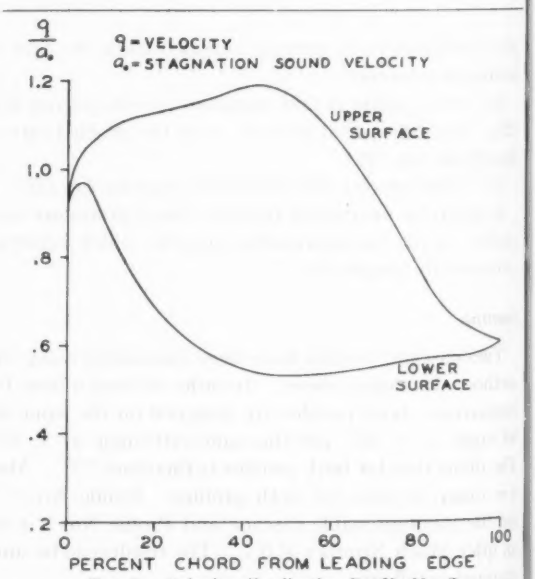

FIG. 8. Velocity distribution Profile No. 2

TABLE 1
Linearized Gas

M_s	q/a_0	q/a	v/v_0	w/a_0	v/v_{0s}	v_s/v_{0s}	Error in v/v_{0s}
0	0	0	1	0	0.93178	1.00000	−0.06822
0.1	0.14035	0.13899	1.00980	0.13967	0.94091	1.00500	−0.06409
0.2	0.27987	0.26951	1.03843	0.27460	0.96759	1.02013	−0.05254
0.3	0.41774	0.38546	1.08375	0.40095	1.00982	1.04561	−0.03579
0.4	0.55319	0.48405	1.1428	0.51632	1.06484	1.08192	−0.01711
0.5	0.68553	0.56542	1.2124	0.61972	1.12973	1.12973	0
0.6	0.81414	0.63135	1.2895	0.71119	1.20153	1.18984	+0.01169
0.7	0.93854	0.68437	1.3715	0.79152	1.27794	1.26330	+0.01464
0.8	1.05826	0.72685	1.4457	0.86540	1.34710	1.35135	−0.00425
0.9	1.17299	0.76098	1.5414	0.92311	1.43625	1.45552	−0.01927
1.0	1.28252	0.78861	1.6263	0.97667	1.51535	1.57744	−0.06209

From the relations of a linearized gas,

$$\frac{v_0}{v} = \frac{\rho}{\rho_0} = \frac{1 - (w^2/4a_0^2)}{1 + (w^2/4a_0^2)}$$

Hence,

$$-\tan \sigma_1 = (\rho_1/\rho_0)\ (Im\ A/Re\ A)$$
$$-\tan \sigma_2 = (\rho_2/\rho_0)\ (Im\ B/Re\ B)$$

which are Eqs. (12) and (13).

APPENDIX (II)

Relations of a Linearized Gas for Cascades

For a linearized gas satisfying the following pressure-volume relation:

$$p_1 - p = D(v - v_1) \qquad \text{(II-1)}$$

where D is a constant and the subscript 1 represents any chosen reference point. It can then be shown that the following relations hold:[2]

$$q^2/a^2 = 1 - (v_0^2/v^2) \qquad \text{(II-2)}$$

$$a^2/q^2 = (a_0^2/q^2) + 1 \qquad \text{(II-3)}$$

$$w/a_0 = (2q/a_0)/[1 + \sqrt{1 + (q/a_0)^2}]$$

or

$$q/a_0 = 4(w/a_0)/[4 - (w/a_0)^2] \qquad \text{(II-4)}$$

In the above equations, q is the velocity, a is the velocity of sound, and the subscript 0 refers to the stagnation state.

It has been customary in dealing with single profiles to use the state of the free stream—i.e., the undisturbed flow at $\pm\infty$—as the reference state p_1, v_1 in Eq. (II-1). In an infinite cascade, however, there is no such thing as a state of undisturbed flow. For best approximation for high subsonic cascades, it is suggested here to pick the point corresponding to isentropic Mach Number (M_s) of 0.5 as the reference point. Let the subscript s denote the properties of an isentropic gas, as distinguished from those of a linearized gas which use no subscript. Then the isentropic relation,

$$(p_s/p_{0s})\ (v_s/v_{0s})^k = 1$$

is being approximated by a chord (Fig. 9) passing through $M_s = 0.5$, with the slope equal to the slope of another line joining the two points $M_s = 0$ and $M_s = 1$ on the isentropic curve. Fig. 9 shows that, with this straight-line approximation, the error introduced is kept to a minimum for the range of M_s covering almost the entire length of a calculated cascade profile for high subsonic flows.

At the reference state (1), $M_s = q_1/a_{1s} = 0.5$ and $p_1/p_{0s} = 0.84302$, $v_1/v_{0s} = 1.12973$ when the ratio of specific heats is taken as 1.4. The slope of the line joining the two points $M_s = 0$ (where $p_s/p_{0s} = v_s/v_{0s} = 1$) and $M_s = 1$ (where $p_s/p_{0s} = 0.52828$, $v_s/v_{0s} = 1.57744$) is −0.81692. The linearized gas is therefore represented by

$$p/p_{0s} = 1.76592 - 0.81692(v/v_{0s})$$

The velocity of sound is defined as

$$a^2 = -v^2 \frac{dp}{dv} = -\left(\frac{v}{v_{0s}}\right)^2 v_{0s}p_{0s} \frac{d(p/p_{0s})}{d(v/v_{0s})}$$

For the isentropic gas,

$$a_s^2 = \left(\frac{v_s}{v_{0s}}\right)^2 v_{0s}p_{0s} \left(\frac{kp_s/p_{0s}}{v_s/v_{0s}}\right)$$

For the linearized gas,

$$a^2 = (v/v_{0s})^2\, v_{0s}p_{0s}\ (0.81692)$$

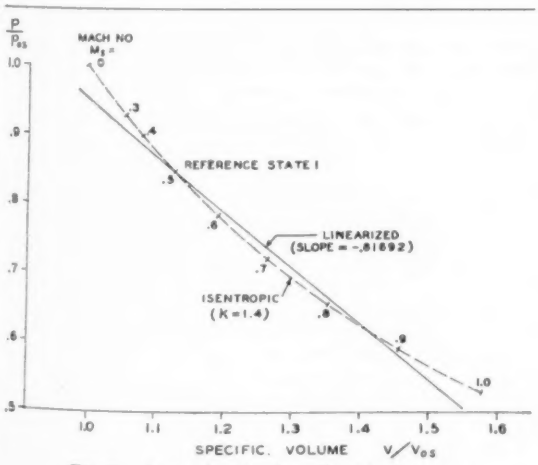

FIG. 9. Approximation by a linearized gas.

At the reference point (1), $v_1 = v_{1s}$; hence, we have, by taking the ratio of the two equations above and substituting the known value of p_s/p_{0s} and v_s/v_{0s} at 1,

$$a_1/a_{1s} = 0.88429$$

Since $M_{1s} = q_1/a_{1s} = 0.5$, therefore,

$$q_1/a_1 = (a_{1s}/a_1)\,(q_1/a_{1s}) = 0.56543$$

Eq. (II-3) gives $q_1/a_0 = 0.68553$.

A table for this linearized gas can be compiled as follows: For a given isentropic Mach Number M_s between 0 and 1, we can find the ratio of the velocity at that M_s to the velocity at $M_s = 0.5$. This is q/q_1. Then,

$$q/a_0 = (q/q_1)\,(q_1/a_0) = 0.68553\,(q/q_1)$$

Having obtained q/a_0, we can find q/a by Eq. (II-3), w/a_0 by Eq. (II-4), and v/v_0 by Eq. (II-2). The resulting table is given herein as Table 1.

In Table 1, the last three columns are for estimating the error involved in the linear approximation. At our reference point (1) where $M_s = 0.5$, we have $v/v_0 = 1.2124$. At the same point, $v/v_{0s} = 1.1297$ from standard gas tables. Hence, for this linearized gas,

$$v_0/v_{0s} = 1.1297/1.2124 = 0.93178$$

Using v_{0s} as the basis of comparison, we can express v of the linearized gas by the ratio

$$v/v_{0s} = 0.93178v/v_0$$

Comparing this ratio with the isentropic v_s/v_{0s} from standard gas tables, we find the error in v/v_{0s} shown in the last column of Table 1.* We see that the error is small for M_s between 0.4 and 0.9.

* This error is an indication of the slight difference in compressibility of the linearized gas as compared with that of the isentropic gas for the same velocity.

References

[1] Lin, C. C., *On the Subsonic Flow through Circular and Straight Lattices of Airfoils*, Jour. of Math. & Physics, Vol. 28, No. 2, July, 1949.

[2] Tsien, H. S., *Two-Dimensional Subsonic Flow of Compressible Fluids*, Journal of the Aeronautical Sciences, Vol. 6, No. 8, August, 1939.

[3] Lin, C. C., *On an Extension of the von-Kármán-Tsien Method of Two-Dimensional Subsonic Flow with Circulation around Closed Profiles*, Quart. of App. Math., Vol. 4, No. 3, October, 1946.

[4] Clauser, F. H., *Two-Dimensional Compressible Flows Having Arbitrarily Specified Pressure Distributions for Gases with Gamma Equal to Minus One*, Symposium on Theoretical Compressible Flow, pp. 1–32, U.S. Naval Ordinance Laboratory, June, 1949.

[5] Durand, W. F., *Aerodynamic Theory*, Vol. II, pp. 91–96; Julius Springer, Berlin, 1934.

[6] Weinig, F., *Die Stromung um die Shaufeln von Turbomaschinen*, Verlag von Johann Ambrosius Barth, 1935.

[7] Gardner, N. F., *Transients in Linear Systems*, Vol. I, pp. 160–163; John Wiley & Sons, Inc., New York, 1942.

[8] Howell, A. R., *Fluid Dynamics of Axial Flow Compressors*, The Inst. of Mech. Engineers Proceedings, Vol. 153, War Emergency Issue No. 12, 1945.

[9] Bogdonoff, S. M., *Performance of Compressor Blade Cascades at High Mach Numbers*, N.A.C.A. R.M. L7D11a, July, 1947.

[10] Tyler, R. A., *The Available Theoretical Analysis of Two-Dimensional Cascade Flow*, Aeronautical Note AN-4, National Research Council of Canada, 1949.

[11] Costello, G. R., *Method of Designing Cascade Blades with Prescribed Velocity Distribution in Compressible Potential Flows*, N.A.C.A. Report No. 978, 1950 (formerly N.A.C.A. T.N. No. 1970).

[12] Costello, G. R., Cummings, R. L., and Sinnette, J. T., Jr., *Detailed Computational Procedure for Design of Cascade Blades with Prescribed Velocity Distributions in Compressible Potential Flows*, N.A.C.A. T.N. No. 2281, February, 1951.

[13] Sinnette, J. T., Jr., Costello, G. R., and Cummings, R. L., *Expressions for Measuring the Accuracy of Approximate Solutions to Compressible Flow through Cascades of Blades with Examples of Use*, N.A.C.A. T.N. No. 2501, October, 1951.

Readers' Forum

BRIEF REPORTS of investigations in the aeronautical sciences and discussions of papers published in the JOURNAL are presented in this special department. The publication will be completed as soon as possible after receipt of the material. The Editorial Committee does not hold itself responsible for the opinions expressed by the correspondents. Contributions should not exceed 800 words in length.

Comments on "Remarks on Dynamic Loads in Landing"[1]

H. Norman Abramson
Analytical Engineer, Dynamic Analysis Group, Chance Vought Aircraft Division, United Aircraft Corporation, Dallas, Tex.
May 9, 1952

THE PROBLEM DISCUSSED by Mr. Zahorski[1] has received a great deal of attention in recent years; however, the analysis of the problem is not yet in a completely satisfactory state.

The writer would like to point out that the method of "normal modes" used in the subject paper has several limitations imposed on it which tend to hamper its accuracy. Among these the following may be specifically mentioned:

(1) The duration of impact must be large compared with the period of the lower modes of vibration so that only a reasonable number of modes need be considered. This was indirectly brought out in the classic paper dealing with the landing impact problem by Biot and Bisplinghoff.[2] It is shown that the moment and shear of a simply supported rectangular beam subjected to a unit impulse is given very poorly by the normal mode procedure, while the same quantities resulting from a unit step function are given relatively more accurately.

(2) Obviously, the distribution of the loading on the structure will be of great importance, for, if the distribution were of the shape of one of the normal modes, only that single mode would be excited. In the problem under discussion, we normally have the load applied at two discrete points along the wing span, and therefore we will expect that many modes will be excited. If the landing is an unsymmetrical one, then we have even more modes to consider, since the unsymmetrical modes will also be excited.

(3) Finally, one must be aware of the fact that resonance between slightly coupled components of the structure may give rise to a transfer of energy from one component to another.

(4) As the author has pointed out, the initial shape of the forcing function is also of considerable importance. This is, of course, intimately related to item (1).

In an experimental investigation, Ramberg[3] has compared the normal mode method (using the analysis of Biot and Bisplinghoff but modified to account for phase relationships between modes) with two other methods.[4, 5] It was found that both of the other methods gave more accurate results than the normal mode method for the case of unsymmetrical impact of *large* duration compared with the fundamental flexural period of the model wing under test. For an unsymmetrical impact of *short* duration, none of the methods gave particularly good results; however, again, the methods of references 4 and 5 gave results that were better than the normal mode method. In all fairness it should be mentioned that the analysis by normal modes employed only three unsymmetrical modes.

Robinson[6] has also felt that " . . . the method of normal modes may be unable to describe contemporary impact load problems adequately" (with regard to landing impact). Perhaps his analysis of beam problems will lead the way to a traveling-wave-type analysis of complex structures under impulsive loading.

In connection with this discussion, one more paper should be mentioned. Kroll and Levy[7] have taken the paper dealing with gust response by Houbolt[8] and adopted his suggestion that a similar analysis might prove of value in the landing problem but with some modification. Kroll and Levy studied the experiments of Ramberg[3] and found, for the long-duration impact, a good correlation with the experimental results. The time required for analysis by this method was slightly less than for the other methods.

This writer feels that the method of normal modes may be used with good results if the modes used (both number and shape) are carefully selected and if the loading situation is not severe [see items (1) and (2) above].

Finally, the writer would like to refer to the question of treating the landing impact force as independent of the response of the structure. Mr. Zahorski feels that " . . . information obtained from an arbitrary free drop of the landing gear is practically useless so far as the dynamic loads are concerned." The writer concurs with this statement as it stands. However, he would like to point out, in view of several references,[9–11] that a good analysis is still possible when assuming the landing impact force to be independent of the airplane structural flexibility, provided that the force-time relations for the shock strut are obtained by replacing the flexible structure by a rigid one of the same mass. Then, perhaps, we can use drop tests, but for the complete assembly and not just the landing gear itself.

REFERENCES

[1] Zahorski, A., *Remarks on Dynamic Loads in Landing*, Journal of the Aeronautical Sciences, Vol. 19, No. 4, p. 258, April, 1952.

[2] Biot, M. A., and Bisplinghoff, R. L., *Dynamic Loads on Aircraft Structures During Landing*. N.A.C.A. A.R.R. 4H10 (W-92), October, 1944.

[3] Ramberg, W., *Transient Vibrations in an Airplane Wing Obtained by Several Methods*, N.B.S. Journal of Research, May, 1949.

[4] Williams, D., and Jones, R. P. N., *Dynamic Loads in Aeroplanes Under Impulsive Loads with Particular Reference to Landing and Gust Loads on a Large Flying Boat*, British R.&M. 2221, September, 1945.

[5] Levy, S., unpublished notes (see reference 3).

[6] Robinson, A., *Shock Transmission in Beams*, British R.&M. 2265, October, 1945.

[7] Kroll, W. D., and Levy, S., *A Step-by-Step Method of Determining the Dynamic Response of Aircraft in Landing*, N.B.S. Lab. No. 6.4/1–181, Pr. 6., September, 1949.

[8] Houbolt, J. C., *A Recurrance Matrix Solution for the Dynamic Response of Aircraft in Gusts*, N.A.C.A. T.N. No. 2060, March, 1950.

[9] Bisplinghoff, R. L., et. al., *Investigation of Stresses in Aircraft Structures Under Dynamic Loading*, M.I.T. Report, January, 1949.

[10] Goland, M., et. al., *Prediction of Dynamic Landing Loads*, U.S.A.F. Air Material Command, T.R. 5815, January, 1949.

[11] Stowell, E. Z., and Houbolt, J. C., *An Evaluation of Some Approximate Methods of Computing Landing Stresses in Aircraft*, N.A.C.A. T.N. No. 1584, May, 1948.

A Third Kind of "Incompressible" Fluid*

A. Martinot-Lagarde
Director, Institute of Fluid Mechanics, Lille, France
May 16, 1952

PROFESSORS KOVASZNAY AND CORRSIN[1] have considered the appropriate approximation to the heat term of the energy equation for two kinds of "incompressible" flow: (a) flow of a "perfect liquid" (density, ρ = constant, exactly) and (b) flow of a gas with Mach Number $M \ll 1$. I should like to examine the question in slightly different terms and to point out a third case: (c) flow of most real liquids.

First, I should like to propose the term "isovolume fluid" (meteorologists often use "isopycnic") instead of "incompressible fluid"; the latter expression overemphasizes the pressure at the expense of other thermodynamic variables.

In purely mechanical problems, we need only write that, for nearly isovolume fluids, $dV \equiv d(1/\rho)$ is zero or negligible. In thermodynamics, things are more complicated. For studying the approximation in question it is convenient to choose alternative pairs of independent variables. For example, with T and V, the heat received is

$$dQ = c_v\,dT + l\,dV \cong c_v\,dT \tag{1}$$

while with T and p,

$$dQ = c_p\,dT + h\,dp \cong c_p\,dT \tag{2}$$

These are the two "isovolume" approximations in question, and we shall see that in most cases Eq. (2) is closer than Eq. (1). c_p and c_v are the customary specific heats, $l \equiv (\partial U/\partial V)_T + p$, $h \equiv l(\partial V/\partial p)_T$, and U is internal energy.

Let us denote the errors in Eqs. (1) and (2) by

$$\epsilon' = l\,dV/c_v\,dT; \qquad \epsilon = h\,dp/c_p\,dT \tag{3}$$

and represent the equation of state over a small range by

$$dV/V = \alpha\,dT - \kappa\,dp \tag{4}$$

where $\alpha = (1/V)(\partial V/\partial T)_p$ and $\kappa = -(1/V)(\partial V/\partial p)_T$, the isothermal compressibility.

From the two laws of thermodynamics, we can deduce some results of Clapeyron.

$$h = -TV\alpha; \quad l = \frac{T\alpha}{\kappa}; \quad c_p - c_v = \frac{TV\alpha^2}{\kappa} \tag{5}$$

These will permit numerical estimates of ϵ and ϵ'. We have first

$$\epsilon = -(TV\alpha/c_p)(dp/dT) \tag{6}$$

As a typical real liquid, consider water near the boiling point flowing through a radiator: $\alpha = 0.00073$, $V = 0.00105$, $\kappa = 0.5 \times 10^{-9}$, and $c_p = 4{,}210$, all in m.k.s.a. units. For conservatism in estimating the negligibility of ϵ, take Δp relatively large and ΔT small: $\Delta p = 10^5$ (about 1 atmosphere) and $\Delta T = 10°$ C. These give $-\epsilon = +0.0007 \ll 1.0$.

We pursue ϵ a bit farther. If Δp corresponds to a velocity change from 0 to u,

$$-V\Delta p \cong (1/2)u^2$$

whence,

$$\epsilon \cong T\alpha u^2/c_p\Delta T \tag{7}$$

For a gas $\epsilon \cong u^2/2c_p\Delta T$; for a liquid it is much smaller.

In general, ϵ can be interpreted in terms of temperature changes alone. If $(dT)_s$ denotes the temperature change that would occur if the pressure variation dp were produced isentropically, $(dT)_s = -h\,dp/c_p$, so that

$$\epsilon = -(dT)_s/dT \tag{8}$$

Now we turn to ϵ'. With the equation of state [Eq. (4)] and l in Eq. (5),

$$\epsilon' = (TV\alpha/\kappa c_v\,dT)(\alpha\,dT - \kappa\,dp) \tag{9}$$

Although $dV/V = (\alpha\,dT - \kappa\,dp)$ is small in isovolume flow, the multiplying factor may be large. Introducing α and κ as in Eq. (5), Eq. (9) becomes

$$\epsilon' = \frac{c_p - c_v}{c_v} + \frac{h\,dp}{c_v\,dT} = (\gamma - 1) + \gamma\epsilon \tag{10}$$

where $\gamma \equiv c_p/c_v$. The second term becomes negligible relative to unity as ϵ does, but the first term is negligible only in certain cases. For example, for water at 4°C., $\alpha = 0$. However $c_p = c_v$ and approximations (1) and (2) are identical in this case anyway.

For gases, $(\gamma - 1)$ is not $\ll 1.0$. Consider a typical liquid. For water at 100°C., $\gamma = 1.11$; for mercury at 0°C., $\gamma = 1.14$; for ethyl ether, $\gamma = 1.40$. It is clear that for gases and most liquids, the $c_p\,dT$ approximation is permissible, while the $c_v\,dT$ is not.

Professor Corrsin has suggested to me that the ϵ'/ϵ ratio admits simple presentation. For example,

$$\frac{\epsilon'}{\epsilon} = \frac{l\,dV}{h\,dp}\cdot\frac{c_p}{c_v} = -\frac{\gamma}{\kappa V}\frac{dV}{dp} = \frac{\kappa_{act.}}{\kappa_s} \tag{11}$$

where $\kappa_{act.}$ is the compressibility in the actual process $[-(1/V)(dV/dp)]$ and κ_s is the "isentropic compressibility" (κ/γ). Eq. (11) shows that approximation (2) is better than (1) for a process far from isentropic but that both are bad—and roughly the same—for nearly isentropic processes.

The principal conclusion of this note is that $dQ \cong c_p\,dT$ whenever $|(dT)_s| \ll |dT|$, even though it may seem paradoxical to equate actual heat received to constant pressure heat received in a process with varying pressure.

REFERENCE

[1] Corrsin, S., and Kovasznay, L. S. G., *The Energy Equation for Two Kinds of "Incompressible" Flow*, Readers' Forum, Journal of the Aeronautical Sciences, Vol. 18, No. 12, p. 843, December, 1951.

* Adapted from a note in the *Revue Générale de Mécanique*, Vol. 40, p. 110, 1952.

Computation of Possio's Integral for Linearized Supersonic Flow

Frederic E. Fuller
Lockheed Aircraft Corporation, Burbank, Calif.
May 26, 1952

THE POTENTIAL,[1] $\varphi(x, y, +0, t)$ for harmonic motions,

$$\Phi e^{ivt} = \frac{e^{ivt}}{\beta\pi}\int_{\xi_1}^{x} e^{-(iv M/\beta^2 a)(x-\xi)}\,d\xi \int_0^{\pi} w(\xi,\eta)\times \cos\left[\frac{\nu}{\beta^2 a}(x-\xi)\sin\theta\right]d\theta \tag{1}$$

is well known.[2–4] In Eq. (1), θ is defined[2] by

$$\eta = [(x-\xi)/\beta]\cos\theta + y \tag{2}$$

The pressure on the $+0$ side of the wing is

$$p(x, y, +0, t)e^{ivt} = -\rho V\left(\frac{\partial\Phi}{\partial x} + \frac{iv}{V}\Phi\right)e^{ivt} \tag{3}$$

The regions of wing plan forms for which Eq. (1) is applicable is, in part at least, well known. Evvard's theorem[3, 4] and a theorem due to Miles and Froelich[5, 6] are useful in this field. The purpose of this note, however, is to outline a method with

which, by means of high-speed digital computing machines, the pressure distribution and the flutter aerodynamic coefficients due to Eq. (1), where applicable, may be computed for suitably arbitrary downwash functions, $w(\xi, \eta)$.

By definition, the flutter aerodynamic coefficient is

$$Q_{\alpha\beta} = \iint_S Z_\alpha(x, y)\, p_\beta(x, y)\, dx\, dy \tag{4}$$

where $Z_\alpha(x, y)$ is the deflection form α and $p_\beta(x, y)$ is the pressure due to the deflection form $Z_\beta(x, y)$ and the integration is over the top and bottom surfaces of the wing. On substituting Eq. (3) in Eq. (4) and integrating by parts,

$$Q_{\alpha\beta} = \rho V \int \left[- \left| Z_\alpha \Phi_\beta \right|_{x_l}^{x_t} + \int \left(\frac{\partial Z_\alpha}{\partial x} - \frac{i\nu}{V} Z_\alpha \right) \Phi_\beta \, dx \right] dy \tag{5}$$

where x_l and x_t are the values of x at the leading and trailing edges, respectively. Φ vanishes at the leading edge, the limit x_l is shown for completeness.

Also,

$$w(x, y) = V \left(\frac{\partial Z}{\partial x} + \frac{i\nu}{V} Z \right) \tag{6}$$

On substituting Eq. (6) in Eq. (1),

$$\Phi = - \frac{V}{\beta\pi} \int_{\xi_l}^{x} e^{-(i\nu M/\beta^2 a)(x-\xi)}\, d\xi \int_0^\pi \left(\frac{\partial Z}{\partial x} + \frac{i\nu}{V} Z \right) \times \cos \left\{ \frac{\nu}{\beta^2 a} (x - \xi) \sin\theta \right\} d\theta \tag{7}$$

The plan is to compute the potential Φ according to Eq. (7) at a set of points on the wing; then by means of these values the pressure distribution according to Eq. (3) and the flutter aerodynamic coefficients according to Eq. (5) will be computed. In these computations and results, the deflections z_α and z_β will remain as explicit symbols, which may be assigned values as required in the use of the results.

For the computations, let the points rs be on a rectangular lattice, and at the points of this lattice on the wing let the deflections z_α, z_β be known. Define the wing plan form by its intersections with the lines of this lattice. A rectangular lattice is chosen in order that the digital computing machine programs may be arranged in part, once and for all, for all plan forms to which this method applies. Devise interpolation formulas so that, with functions known at the points rs, values of the functions may be computed at intermediate points. Intermediate points will be introduced as required for the numerical integrations.

In the following, let $[\ ]$, $[^0]$, $\{\ \}$, $|\ |$ denote rectangular, diagonal, column, and row matrices, respectively. Construct a matrix $[w]$ defined by

$$\left\{ \frac{\partial Z}{\partial x} + \frac{i\nu}{V} Z \right\}_{rs} = [w] \{ Z_{rs} \} \tag{8}$$

Consider now the computation of the potential at the point rs on the wing. First, consider computation of the integral

$$\int \left\{ \frac{\partial Z}{\partial x} + \frac{i\nu}{V} Z \right\} \cos \left\{ \frac{\nu}{\beta^2 a} (x - \xi) \sin\theta \right\} d\theta \tag{9}$$

for a given point rs at xy and for a particular ξ within the forward Mach lines through rs. On the line ξ, choose points at equal intervals of θ and interpolate $\{(\partial Z/\partial x) + (i\nu/V)Z\}$ to these points. Then compute the integrand of Eq. (9) at these points and finally the integral (9). The computations may be arranged as follows:

Let

$[w^\xi]$ = the part of $[w]$ which gives values of $\{(\partial Z/\partial x) + (i\nu/V)Z\}$ on the span-wise line ξ

$[I^{\xi rs}]$ = a matrix for interpolating from the point on the line ξ to the points equally spaced in θ relative to the point rs

$[J_\theta^{\xi rs}]$ = a matrix for integrating over θ on the points equally spaced in θ relative to the point rs

$[{}^0\cos^{\xi rs}]$ = matrix of the quantities $\cos\{(\nu/\beta^2 a)(x - \xi) \sin\theta\}$ at the points equally spaced in θ

Then,

$$\left\{ \int \left\{ \frac{\partial Z}{\partial x} + \frac{i\nu}{V} Z \right\} \cos \left\{ \frac{\nu}{\beta^2 a} (x - \xi) \sin\theta \right\} d\theta \right\}^{\xi rs} = [J_\theta^{\xi rs}]\, [{}^0\cos^{\xi rs}]\, [w^\xi]\, \{ Z_\beta \} \tag{10}$$

When $\{(\partial Z/\partial x) + (i\nu/V)Z\}$ is constant over the interval of integration from 0 to π, the integral (9) is

$$\pi J_0 \{(\nu/\beta^2 a)(x - \xi)\}\, [w^\xi]\, \{ Z_\beta \} \tag{11}$$

At the point $\xi = x$, the integral (9) is

$$\pi [w^\xi]\, \{ Z_\beta \} \tag{12}$$

Having computed the integrals (9) relative to rs on segments of spanwise lines at ξ intercepted by the forward Mach lines through rs or wing plan form, arrange them in a matrix

$$[\theta^{\xi rs}]\, \{ Z_\beta \}$$

Compute the $e^{-(i\nu M/\beta^2 a)(x - \xi)}$ for the corresponding spanwise lines and arrange them in a matrix $[{}^0e^{\xi rs}]$; construct a matrix $[J_\xi^{\xi rs}]$ for integrating over all the ξ on the wing in the Mach cone forward of the point rs. Then, finally, for the point rs,

$$\Phi^{rs} = - \frac{V}{\beta\pi} [J_\xi^{\xi rs}]\, [{}^0e^{\xi rs}]\, [\theta^{\xi rs}]\, \{ Z_\beta \} \tag{13}$$

Arrange all the Φ^{rs} in a matrix form

$$|\Phi^{rs}| = -(V/\beta\pi)\, |P|\, \{ Z_\beta \} \tag{14}$$

If the pressures at the points rs are required, then

$$\{ p_{rs} \} = [\rho V^2/\beta\pi)\, [w]\, [P]\, \{ Z_\beta \} \tag{15}$$

For computing the $Q_{\alpha\beta}$, construct the matrix

$$[S] = [[\bar{w}]\, [{}^0J_x^{\,y}] - [\delta_{rt}]]\, [J_y{}^0] \tag{16}$$

Then,

$$Q_{\alpha\beta} = - (\rho V^2/\beta\pi)\, |Z_\alpha|\, [S]\, [P]\, \{ Z_\beta \} \tag{17}$$

where

$[\bar{w}]$ = transpose of the complex conjugate of $[w]$

$[\delta_{rt}]$ = matrix corresponding to $[\bar{w}]$ but with zero elements, except for the trailing edge points where the element is unity

$[{}^0J_x]$, $[{}^0J_y]$ = diagonal matrices of terms which, if multiplied as a prefactor with a column and summed, give the integral over x, y of the function for which the column gives the values at the points of x, y

The matrices $[S]$ and $[w]$ are, except for $i\nu/V$ in the diagonal elements, constants independent of Mach Number and frequency but depending on plan form. The matrices $[J_\xi^{\xi rs}]$ are independent of Mach Number and frequency and depend on plan form. The matrices $[J_\theta^{\xi rs}]$ are constants but are dependent on the range of θ and are proportional to the range of η corresponding to range of θ. The sets of numbers $x - \xi$ are also constants. Thus, although the task of preparing the problem for the computing machines is formidable, much of it, when once done, applies for all Mach Numbers and frequencies for which Eq. (1) is applicable for a particular plan form.

A major task in proceeding from the statement of the problem given here to programs for digital computing machines lies in devising integrating means for equally spaced data but oddly placed limits. The number of cases for a particular Mach Number and

plan form is large; all of the cases change for different Mach Number or plan form.

References

[1] Possio, C., *L'Azione Aerodinamica sul profilo oscillante alle velocita ultrasonore*, Acta, Pont. Acad. Sci., Vol. I, No. 11, pp. 93–106, 1937.

[2] Garrick, I. E., and Rubinow, S., *Theoretical Study of Airforces on an Oscillating or Steady Wing in a Supersonic Main Stream*, N.A.C.A. T.R. No. 872, July, 1947.

[3] Stewart, H. J., and Ting-Yi Li, *Source Superposition Method of Solution of a Periodically Oscillating Wing at Supersonic Speeds*, Quarterly of Applied Mathematics, April, 1951.

[4] Evvard, J. C., *A Linearized Solution for Time-dependent Velocity Potentials Near Three-Dimensional Wings at Supersonic Speeds*, N.A.C.A. T.N. No. 1699, September, 1948.

[5] Miles, John W., *On Harmonic Motion of Wide Delta Airfoils at Supersonic Speeds*, NAVORD Report 1234, NOTS 294, June 13, 1950.

[6] Froelich, Jack E., *Nonstationary Motion of Purely Supersonic Wings*, Journal of the Aeronautical Sciences, Vol. 18, No. 5, pp. 298–310, May, 1951.

Remarks on "Correction for Aspect Ratio of the Indicial Lift Functions of Wagner and Küssner"

S. F. Shen

Department of Aeronautical Engineering, University of Maryland, College Park, Md.

May 29, 1952

IN A RECENT NOTE, Scanlan[1] pointed out that, knowing the aspect ratio correction on the Theodorsen function $C(k)$, such as Reissner's $\sigma(k)$, one can deduce, by the well-known transform relationships first proposed by Garrick, the appropriate indicial lift functions of Wagner and Küssner including the aspect ratio effects.

Attention might be called to the fact that Jones[2] had previously employed exactly the same resultant expressions in his theory of lifting surfaces in nonuniform motion. although the aspect ratio correction $\sigma(k)$ was derived in a different manner. In fact, Jones went slightly further to include a correction on the apparent mass term, which was omitted in reference 1.

References

[1] Scanlan, R. H., *Correction for Aspect Ratio of the Indicial Lift Functions of Wagner and Küssner*, Readers' Forum, Journal of the Aeronautical Sciences, Vol. 19, No. 5, pp. 357–358, May, 1952.

[2] Jones, W. P., "Aerodynamic Forces on Wings in Non-uniform Motion," British R. & M. 2117, 1945.

Hooke's Gas in Aerothermodynamics

Ing. Ennio Mattioli

Scuola di Ingegneria Aeronautica, Rome, Italy

May 19, 1952

Summary

It is shown that the use of Hooke's gas ($\gamma = -1$) is inopportune and that it is preferable to limit oneself to Kármán-Tsien's "tangent gas." One observes that the "correction coefficient" of the latter is nearly exact in the *entire* flow if $M_{max.} = \sim 0.5$.

Discussion

MANY TRANSFORMATIONS OF AEROTHERMODYNAMICS[1] are assumed to be adiabatic. This gives, for perfect gases, the relation

$$p\rho^{-\gamma} = \text{const.} = k, \quad k > 0 \tag{1}$$

One can construct an aerothermodynamics assuming as an equation of the adiabatic transformation any relation

$$f(p, \rho) = 0 \tag{2}$$

of a type different from Eq. (1). It will be sufficient to set aside some of the hypotheses of the perfect gas. In particular, one can consider the gases with straight adiabatic in the plane $(1/\rho, p)$:

$$p - p_1 = m[(1/\rho) - (1/\rho_1)], \quad m = \text{const.} \tag{3}$$

$1/\rho_1$, p_1 being value at a state of reference of the gas.

Preserving, also, the definition of the velocity of sound,

$$a^2 = dp/d\rho \tag{4}$$

(differentiation along an adiabatic) one will have for such gases,

$$a^2\rho^2 = -m \tag{5}$$

and, therefore, we must have $m < 0$.

Bernoulli's equation,

$$(dp/\rho) + V\,dV = 0$$

integrated along a stream line gives

$$a^2 - V^2 = \text{const.} \tag{6}$$

Dividing Eq. (6) by Eq. (5), one obtains

$$(1 - M^2)/\rho^2 = \text{const.} \tag{7}$$

with M = Mach Number. This result was found for a "tangent gas" by Tsien[2] and von Kármán,[3] who substituted for the adiabatic line of the perfect gas its tangent at the point $1/\rho_1$, p_1 corresponding to conditions at infinity. They utilized the constancy of the first member of Eq. (7) in order to obtain their noted "correction coefficient."

For this "tangent gas," therefore, Eqs. (5) and (6) are satisfied with

$$m = -\rho_1^2 a_1^2 = -\rho_1^2 (dp/d\rho)_1 = -\gamma p_1 \rho_1 < 0 \tag{8}$$

For the perfect gas, one has, in place of Eqs. (5) and (6), as noted[4]

$$a^2\rho^{1-\gamma} = \text{const.} \tag{5'}$$

$$a^2 + [(\gamma - 1)/2]V^2 = \text{const.} \tag{6'}$$

$$\left(1 + \frac{\gamma - 1}{2} M^2\right)^{2/(1-\gamma)} / \rho^2 = \text{const.} \tag{7'}$$

Hooke's gas is defined as a hypothetical perfect gas having $\gamma = -1$.[5, 6]

With $\gamma = -1$, Eq. (1) becomes a straight line,

$$p = k(1/\rho) \tag{9}$$

Therefore, for this gas, Eqs. (5) and (6) hold true with $m = k$. However, since Eqs. (5′) and (6′) must hold true also, with $\gamma = -1$, it follows that the relationship of Eqs. (5) and (6) valid for the gases with straight adiabatics, and in particular for Kármán-Tsien's tangent gas, can be obtained formally from those of the perfect gas by putting in the latter $\gamma = -1$. However, the adiabatic equations of these gases are of the type of Eq. (3) with $m < 0$ and cannot result in any way from the corresponding formula for the perfect gas.

For Hooke's gas, one has

$$a^2 = -(p/\rho) < 0 \tag{10}$$

therefore, one cannot speak in this case of the velocity of sound. In the numerous problems in which the speed of sound figures in the square, one can use formally Eq. (10), but it is rather inopportune to introduce in the calculations an expression a^2 to indicate a negative number.

The adiabatics of Hooke's gas pass through the point of intersection of the axis with the slope $k > 0$; therefore, such a gas can never be used as a "tangent gas" of a perfect gas.

In addition, Eq. (9), since $k > 0$, shows that in an adiabatic expansion of Hooke's gas the pressure and volume increase simultaneously; this is in striking contrast to our usual concept of physics in this connection.

For these reasons it seems inadvisable to use Hooke's gas even as a simple mathematical model.

If one develops in series the numerator of Eq. (7′) and supposes the powers of M with exponent ≥ 4 to be insignificant compared with unity, one obtains again Eq. (7) as an approximation to Eq. (7′). For $M = 0.5$ and $\gamma = 1.4$, the error committed in stopping the development in series at the second term is about 3 per cent and decreases to about 1 per cent for $M = 0.4$.

Therefore, if the Mach Numbers of the entire field of speed do not exceed much more than $M = 0.5$, the Kármán-Tsien coefficient deduced from Eq. (7) can be considered sufficiently exact for all the points of the flow, from those at stagnation to those of maximum velocity. This represents a sure advantage over the linearized theory which is in error near $V = 0$.

References

[1] Crocco, G. A., *Principi concettuali della propulsione a reazione*, Ministero della Difesa-Aeronautica, 1949.

[2] Tsien, H. S., *Two-Dimensional Subsonic Flow of Compressible Fluid*, Journal of the Aeronautical Sciences, Vol. 6, No. 10, pp. 399–407, August, 1939.

[3] von Kármán, Th., *Compressibility Effects in Aerodynamics*, Journal of the Aeronautical Sciences, Vol. 8, No. 9, pp. 337–356, July, 1941.

[4] Pistolesi, E., *Lezioni di aerodinamica*, Vallerini, Pisa, 1950.

[5] Busemann, Adolf, *The Drag Problem at High Subsonic Speeds*, Journal of the Aeronautical Sciences, Vol. 16, No. 6, p. 337, June, 1949.

[6] Sauer, R., *Ecoulements des fluides compressibles*, Ch. Beranger, Paris, 1951.

Reply to Comments on "Horizontal Tail Loads in Abrupt Pull-Ups from Level Flight"

J. L. Decker
The Glenn L. Martin Company, Baltimore, Md.

May 26, 1952

The comments of Etkin[1] on "Horizontal Tail Loads in Abrupt Pull-Ups from Level Flight"[2] indicate that several points relative to the subject require clarification.

The general tail-load problem involves the determination of the air loads that are critical in the design of the structure. The critical design loads fall into four broad categories: (1) maximum overall tail load, (2) maximum torque load, (3) maximum load on elevator, and (4) maximum load on stabilizer. Of these four critical load types, only the first is critical in pull-up or pushover maneuvers involving pitching acceleration. The maximum horizontal tail torque, for instance, is usually critical in a steady turning maneuver at limit load factor, with a forward center of gravity location.

Etkin raises three objections to the fourth-degree polynomial n vs. t relation used in reference 2 to represent the pull-up that gives the maximum tail load. These objections are:

(1) $d\delta_e/d_t \neq 0$ at $t = 0$, the start of the maneuver.

(2) $d\delta_e/d_t$ during the entry to the pull-up is too small in absolute magnitude relative to $d\delta_e/d_t$ at $n_{max.}$.

(3) If the solution is extended beyond the time for $n_{max.}$, higher tail loads are computed.

With respect to the first objection, it is obviously theoretically true that, if a pull-up maneuver is initiated from stabilized level flight, $d\delta_e/d_t = 0$ at the start of the maneuver. However, as may be seen from flight records, of which those in reference 3 are typical, the time interval required to develop an elevator deflection rate of the magnitude required by Eq. (13) of reference 2 is extremely small and, for engineering purposes, is negligible. Considerable success has been achieved in the calculation of maneuvering tail loads in the past[4] by assuming the elevator motion producing the maneuver to be made up of several constant $d\delta_e/d_t$ segments. This implies infinite acceleration of the elevator at each end of a segment.

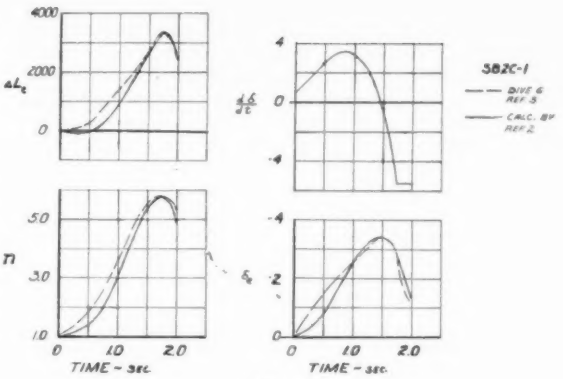

FIG 1.

Concerning the relatively low elevator rates required by Eq. (13) of reference 2 during the early phases of the maneuver, it was realized by the writer that larger values of positive pitching acceleration could, and sometimes would, exist in the early part of the pull-up. This is not considered objectionable, since this phase of the maneuver does not result in a critical loading condition of the horizontal tail. Flight records, such as are shown in reference 3, indicate that the tail load in the pull-up entry is but a fraction of the load existing at the maximum load factor. This is particularly true at aft c.g. locations where the maximum tail load occurs.

It was pointed out by the author in reference 2 that the quartic polynomial n vs. t relation resulted in a tail-load variation that was increasing at the time for $n_{max.}$ and that this relation was not to be used after $n_{max.}$ was attained. It was also pointed out that, if the pitching acceleration at $n_{max.}$ (which is the largest value of $\ddot{\theta}$ occurring during the maneuver) is held throughout the recovery, the tail load diminishes during the recovery. It is also true that, if $d\delta_e/d_t$ existing at $n_{max.}$ is maintained throughout the recovery, the maximum tail load will still occur at $n_{max.}$ If a tail load that exceeds the value existing at $n_{max.}$ is to be developed, it is necessary to have available a value of $d\delta_e/d_t$ which exceeds that existing at $n_{max.}$. Since, in reference 2, a variation of the maximum value of $d\delta_e/d_t$ for use in the tail-loads calculations has been proposed, it is inconsistent with the general method to use a higher value of $d\delta_e/d_t$ in the recovery. From a mathematical standpoint, the type of pull-up recovery may be defined by the condition: for $t \geqq t_{max.}$,

$$(d\delta_e/d_t)_{\text{during recovery}} = (d\delta_e/d_t)_{\text{at } t_{max.}}$$

The type of recovery so defined will be consistent with the pull-up of reference 2.

Inspection of considerable flight-test data, for which reference 3 shows representative results, indicates that the maximum tail load occurs simultaneously with the maximum load factor in an abrupt pull-up maneuver. Normal piloting technique results in a type of maneuver for which the tail load decreases rapidly after $n_{max.}$ has been attained. It should be noted that there is an infinite number of maneuvers in which an airplane can reach a given load factor in a given time as the piloting technique is altered. From a practical standpoint, the prime requirement of the method to compute the maneuvering tail load is that it predicts the maximum positive pitching acceleration that is likely to occur at the limit load factor. For airplanes that have been checked by the writer, the method of reference 2 has yielded excellent results.

Fig. 1 shows the variation of load factor, change in elevator deflection from trim, and change in tail load from the level flight trim condition versus time for an abrupt pull-up performed with an SB2C-1 airplane. Flight data from reference 3 and calculations by reference 2 are compared. The maximum load factor of 5.8 and time to attain it of 1.75 sec. were selected for the calculations to duplicate the flight example. A maximum increment in tail load during the pull-up of 3,330 lbs. was computed from reference 2, and this shows nearly perfect agreement with the flight results, which indicate approximately, 3,300 lbs. delta tail load. The constant value of $d\delta_e/d_t$ in the recovery produces a load variation that closely checks that in the flight results.

REFERENCES

[1] Etkin, Bernard, *Comments on Horizontal Tail Loads in Abrupt Pull-Ups from Level Flight*, Readers' Forum, Journal of the Aeronautical Sciences, Vol. 19, No. 4, p. 283, April, 1952.

[2] Decker, James L., *Horizontal Tail Loads in Abrupt Pull-Ups from Level Flight*, Journal of the Aeronautical Sciences, Vol. 18, No. 12, p. 835, December, 1951.

[3] Matheney, C. E., *Comparison Between Calculated and Measured Loads on Wing and Horizontal Tail in Pull-Up Maneuvers*, N.A.C.A. A.R.R. L5H11, 1945.

[4] Kelley, Joseph, Jr., and Misall, John W., *Maneuvering Horizontal Tail Loads*, AAFTR 5185, 1945.

Note on the Calculation of Transport Properties of Gas Mixtures*

Eldon L. Knuth

Guggenheim Fellow in Jet Propulsion, Daniel and Florence Guggenheim Jet Propulsion Center, California Institute of Technology

May 23, 1952

As a result of recent theoretical studies on transport properties of gases by Hirschfelder, et al.,[1] and others,[2] the dynamic viscosity (μ), the thermal conductivity (λ), and the mechanical diffusivity (D), as well as the dimensionless ratios Prandtl Number ($Pr = C_p \mu/\lambda$, where C_p = specific heat at constant pressure), Schmidt Number ($Sc = \mu/\rho D$, where ρ = density), and $\lambda/\rho C_p D$† may now be calculated rapidly and with a reasonable degree of accuracy both for pure gases and for mixtures of gases, provided that the temperature of the gases is not too low. This happy state of affairs does not seem to be realized by aeronautical engineers, and it is the purpose of the present note to call attention to it.

The greatest error in these calculations arises in the determination of λ, where the Eucken approximation is used. This approximation involves the assumption that thermal equilibrium is established between the translational and internal degrees of freedom of colliding molecules, an assumption that describes physical facts most closely at elevated temperatures. However, even at moderate temperatures, the calculated values of λ are not in error, in most cases, by more than 2 per cent according to reference 1.

As an illustration, calculations have been made for Pr of dry air (80 per cent nitrogen and 20 per cent oxygen) and for Sc and $\lambda/\rho C_p D$ for water diffusing into air, assuming that C_p (see reference 4), μ, ρ, and λ are those of dry air and that no diffusion by temperature gradient occurs. The results of these calculations are presented in Fig. 1. It is expected that the methods of calculation to which attention has been called in this communication will be of value, for example, to engineers interested in

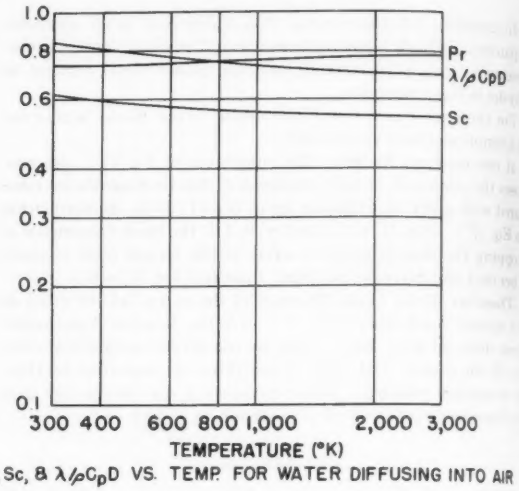

FIG. 1.

boundary-layer calculations or the determination of transport coefficients in combustion chambers.

REFERENCES

[1] Hirschfelder, J. O., Bird, R. B., and Spotz, Ellen L., *Viscosity and Other Physical Properties of Gases and Gas Mixtures*, Trans. A.S.M.E., November, 1949.

[2] Bromley, L. A., and Wilke, C. R., *Viscosity Behavior of Gases*, Ind. & Eng. Chem., July, 1951.

[3] Klinkenberg, A., and Mooy, H. H., *Dimensionless Groups in Fluid Friction, Heat, and Material Transfer*, Chemical Engineering Progress, January, 1948.

[4] For values of C_p, see, for example, National Bureau of Standards, "Tables of Selected Values of Chemical Thermodynamic Properties," Series III, Vol. I, March 31, 1947, to June 30, 1949.

The Prandtl Membrane Analogy for Temperature Fields with Permanent Heat Sources or Sinks

Paul J. Schneider

Department of Mechanical Engineering, The State University of Iowa

June 4, 1952

The Prandtl membrane analogy is frequently employed for experimental evaluation of mechanical stress fields as exemplified by the well-known Saint-Venant torsion problem for prismatic bars.[1-3] The analogy has a number of logical extensions, one of which includes experimental solutions for steady-state two-dimensional temperature distributions satisfying the Poisson partial-differential equation—i.e., temperature fields in regions with permanent internal heat sources or sinks. Approximate numerical (iterative) solutions and exact eigenfunction solutions for these temperature fields are possible to obtain only when the boundary geometry of such regions is of elementary form—circular, elliptical, and rectangular. On the other hand, membrane solutions encompass all cases of nonregular boundary geometry which are otherwise numerically awkward and mathematically intractable.

The ordinates $z(x,y)$ of the surface of a homogeneous membrane (such as the soap film in Fig. 1) spread between appropriately designed boundaries and dilated by a uniform static pressure are to be accurately measured, and these measurements are then to be reinterpreted in terms of the temperature field

* The calculations required for Fig. 1 were made with the assistance of E. Zukoski, G. McLeod, F. Hartwig, and J. Schroeder.

† Although a Klinkenberg and H. H. Mooy have given the name "Lewis Number" to $\lambda/\rho C_p D$ in reference 3, this nomenclature is not generally used in the present literature.

FIG. 1. Side view of a dilated soap film on a circular boundary.

$t(x,y)$ in a region having the same two-dimensional boundaries. The partial-differential equation of this membrane surface is given in reasonable approximation by

$$\frac{\partial^2}{\partial x^2} z(x,y) + \frac{\partial^2}{\partial y^2} z(x,y) + \frac{p}{\tau} = 0 \qquad (1)$$

providing the maximum slope of the film does not exceed say 30°. The constants p and τ are identified, respectively, as the dilation pressure and film tension. Now, the characteristic partial-differential equation satisfied by the steady-state temperature $t(x,y)$ in a region of constant thermal conductivity k_0 generating or absorbing uniform heat q_0 is given by

$$\frac{\partial^2}{\partial x^2} t(x,y) + \frac{\partial^2}{\partial y^2} t(x,y) + \frac{q_0}{k_0} = 0 \qquad (2)$$

The apparent mathematical identity exhibited between Eqs. (1) and (2) leads directly to an analogic relation between the analogs $z(x,y)$ and $t(x,y)$ of the form

$$\xi[t(x,y)] = (k_0/q_0)t(x,y) \equiv \xi[z(x,y)] = (\tau/p)z(x,y) \qquad (3)$$

or specifically

$$t(x,y) = (q_0/k_0)\,(\tau/p)z(x,y)$$

Identifying q_0 and k_0 for the region gives the algebraic relation in terms of the ratio τ/p for converting experimental membrane data $z(x,y)$ to analogous temperatures $t(x,y)$.

In all cases the experimental ratio p/τ can be evaluated with sufficient accuracy from an auxiliary dilated soap film on a circular boundary. The ordinary differential equation in cylindrical coordinates for the surface of this auxiliary symmetrical film of radius r_1 is

$$\frac{d^2}{dr^2} z_a + \frac{1}{r}\frac{d}{dr} z_a + \left(\frac{p}{\tau}\right)_a = 0$$

which has the particular solution

$$z_a = (1/4)\,(p/\tau)_a\,(r_{a_1}{}^2 - r_a{}^2)$$

satisfying the required boundary conditions $z_a(r_1) = 0 = (dz_a \div dr)_{r=0}$. Herewith in terms of the easily measured maximum ordinate z_{a_0} at $r = 0$

$$(p/\tau)_a = (4/r_{a_1}{}^2)z_{a_0} \qquad (4)$$

Then, simply, $(p/\tau) = (p/\tau)_a$ if $p = p_a$. In this way any boundary temperature may be duplicated by building up z on the main boundary without introducing additional difficulties in evaluating p/τ. For the most elementary case with $t(\eta,\mu) = 0$ on the boundary (η,μ), then also $z(\eta,\mu) = 0$ for the membrane boundary.

These techniques encompass all cases with known distributions of boundary temperature regardless of the geometric complexity of the boundary. In support of this, experimental evidence has been obtained for a number of elementary examples to verify that such analogic solutions are in substantial agreement with corresponding exact analytical solutions.

REFERENCES

[1] Cushman, P. A., *Shearing Stresses in Torsion and Bending by Membrane Analogy*, Trans. A.S.M.E. (Applied Mech.), June, 1932.

[2] Griffith, A. A., and Taylor, G. I., *The Use of Soap Films in Solving Torsion Problems*, Trans. I.M.E., December, 1917.

[3] Neubauer, E. T. P., and Boston, O. W., *Torsional Stress Analysis of Twist-Drill Sections by Membrane Analogy*, Trans. A.S.M.E., November, 1947.

Note on the Theory of Hurricanes

Theodore Theodorsen
Hq., Air Research & Development Command, Baltimore, Md.

April 30, 1952

THERE ARE CERTAIN INTERESTING CONSEQUENCES of the new theory of turbulence* applying directly to the theory of hurricanes. These are: Hurricanes are created by the "collapse," in a universal pattern, of a large-scale boundary layer of considerable horizontal extension. Contrary to the situation in a small-scale boundary layer, where the more or less symmetrical "horseshoe" develops, only the counterclockwise branch of the vortical motion will generally appear in the northern hemispheres, since there is no longer complete symmetry because of the action of the Coriolis forces. Evidently, the required boundary layer develops by the passing of an air mass over extensive smooth surfaces such as the oceans or plains. The boundary layer becomes superlatively unstable, or, one may say, there obtains under such circumstances a greatly delayed transition. Then, let us say that somewhere on the surface below the air mass an obstruction occurs; the transition takes place violently, since the lower critical may have been passed by a thousand-fold. Turbulence develops behind the obstruction and produces an extensive retarded air mass. This situation is then mathematically equivalent to the existence of a portion of a large vortex extending from the ground over the upper boundary of the disturbed air mass and down to the ground on the other side of the retarded air mass. As the Reynolds Number is far above the critical, the vortex develops with great intensity by the universal turbulent mechanism; the horizontal portion of the vortex is moved downstream and upwards as shown in the new theory of turbulence. Clearly, the counterclockwise arm will develop most easily and, at least for large dimensions, will appear alone. Thus, the creative mechanism of hurricanes is entirely similar to the mechanism of turbulence.

* The Second Midwestern Conference on Fluid Mechanics, March 17, 1952, Theodore Theodorsen, "Mechanism of Turbulence."

On Boundary-Layer Temperature Recovery Factors

B. des Clers and J. Sternberg
Ballistic Research Laboratories, Aberdeen Proving Ground, Md.

May 15, 1952

IN A PAPER IN THE January, 1952, JOURNAL OF THE AERONAUTICAL SCIENCES, "Recent Investigation of Temperature Recovery and Heat Transmission on Cones and Cylinders in Axial Flow in the N.O.L. Aeroballistics Wind Tunnel," Eber presents some experimental data for boundary-layer temperature recovery factors. The results of a series of recovery factor measurements in the B.R.L. flexible nozzle tunnel using cones and

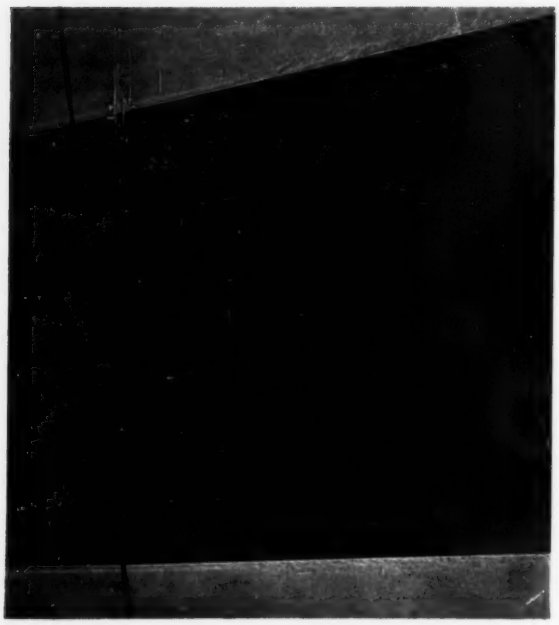

FIG. 1. Spark shadowgraph showing transition at $Re_\infty = 3.2 \times 10^6$. Surface Mach Number = 3.40.

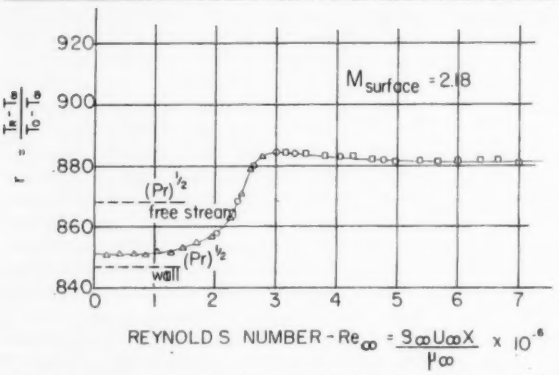

FIG. 2. Cone recovery factors — 10° included angle cone surface Mach Number = 2.18. R, conditions at an insulated wall; ∞, conditions at outer edge of boundary layer; 0, conditions at stagnation.

cone cylinders do not agree with Eber's results for the transitional and turbulent recovery factors.

Laminar, transitional, and turbulent boundary-layer flow was obtained on a 14.5-in. 10° included angle cone at surface Mach Numbers of 1.40 to 3.40. The model was constructed of wood, and thermocouple wires attached to small plugs spaced along an element of the cone were used to measure the recovery temperature. The tunnel was operated at the test condition for 20–30 min. to allow the model to reach its equilibrium temperature. Shadowgraph pictures, such as Fig. 1, corroborate the identification of the transition region made from the temperature measurements. A typical set of measurements is shown in Fig. 2. The absolute accuracy in r is estimated at ± 0.007; the relative accuracy can be seen from the graph. Our conclusions are as follows:

(1) The turbulent recovery factor has a value of about 0.88 and does not significantly change with Mach Number, at least up to $M = 3.40$. Eber obtained a value of $r = 0.92$ at $M = 2.86$ and $r = 0.97$ at $M = 4.25$.

(2) The recovery temperature rises smoothly from the laminar value to a maximum not more than 1 per cent higher than the turbulent value. At $M = 2.87$, Eber obtained peak values about 5 per cent higher. We believe that the peak that we obtained (which is not present in all cases) may be due to nonequilibrium turbulent profiles at the end of the transition region, since the temperature and velocity profiles at the end of the transition region should depend on the mechanism of transition in any given case.

The measurements on a cone cylinder where transition occurred on the cylinder agree with the above results.*

It is possible that Eber's measurements do not represent equilibrium conditions. The recovery temperature at the measuring station may be affected by heat transfer from the model to the boundary layer ahead of the measuring station, since with the short running time available it is probable that the large thermal inertia of his model prevents it from coming to temperature equilibrium. As noted by Eber, his schlieren photographs show that the boundary layer is fully turbulent where the recovery factors are constant. Since the boundary layer is laminar on the cone, it is possible that, over most of the region downstream of the shoulder which he labels transitional, the boundary layer may still be laminar.

* Measurements just published at the N.A.C.A. Ames Aeronautical Laboratory by H. A. Stine and R. Scherrer (*N.A.C.A. T.N. No. 2664*) are in complete agreement with our conclusions (1) and (2).

Secondary Flow in Cascades

H. G. Loos and J. Zwaaneveld
National Aeronautical Research Institute, Amsterdam Holland
May 26, 1952

IN A NOTE BY STEPHENSON,[1] the vortex field behind a cascade with an infinite number of blades in a nonuniform flow is investigated. Stephenson calculates the secondary rotation behind the cascade and adds the trailing vortices.

In a later note, by Eichenberger,[2] it is suggested that the adding of the trailing vortices is incorrect.

Eichenberger's arguments are the following: The flow through the cascade can be idealized as a flow through a curved channel. The secondary vortices then give a flow field as shown in Fig. 1 and on the two sides of the wall A-A there is a different velocity.

So, the wall A-A can be replaced by a vortex sheet. On the other hand, a vortex sheet with vortices along stream lines can be replaced by a thin wall. So, the resulting velocity field due to the nonuniform inlet flow can be said to be induced by the second-

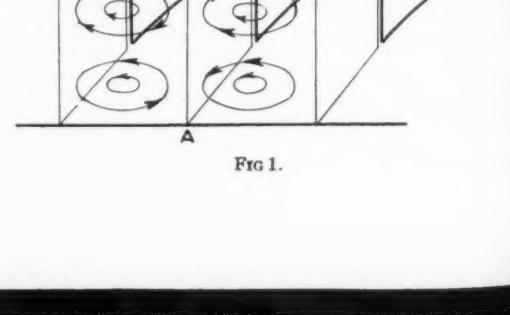

FIG 1.

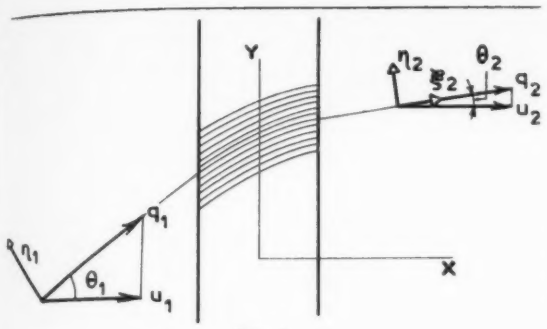

FIG 2.

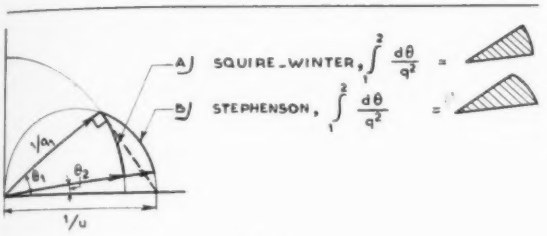

FIG 3.

ary vortices alone if the trailing vortex sheets are replaced by walls.

Eichenberger concludes that the velocity field of the trailing vortices must not be taken into account.

Making Eichenberger's conclusion, one must say explicitly that the velocity field of the secondary vortices must be determined with the boundary conditions on the walls, which replace the trailing vortex sheets. However, the shape of these "walls" is not yet known, since, therefore, the complete flow field must be known. Therefore, this point of view seems to be fruitless.

To obtain an approximate solution, the secondary vortices and the trailing vortices are considered to be transported by the mean flow, so that the induced velocities can be calculated.

Instead of the direct connection (suggested by Eichenberger) between the secondary vortices and trailing vortices, there exists another, more complicated connection via the downwash field of the secondary vortices and the Kutta condition at the trailing edges of the blades.

As Eichenberger remarks, the vorticity vector does not remain constant through the cascade, in general. However, for a cascade with an infinite number of blades, it is impossible to determine the secondary vortices with Squire and Winter's[4] assumption for the basis flow (q/τ = constant).

In problems like this, where the secondary rotation in lightly nonuniform flows is investigated, the relation of Hawthorne[3]

$$(\xi/q)_2 - (\xi/q)_1 = -2|\eta_1|q_1\int_1^2 (d\theta/q^2)$$

appears to be useful.

In this relation, q and θ are the modulus and the angle of the velocity vector in the mean flow, while ξ and η are the components of the rotation in the mean flow direction and perpendicular to it (Fig. 2).

The integral must be evaluated along the stream lines of the mean flow.

Using the fact that the velocity component u (Fig. 2) is constant in the whole field, the integral can be calculated directly

$$\int_1^2 \frac{d\theta}{q^2} = \frac{1}{u^2}\int_1^2 \cos^2\theta\, d\theta = \frac{1}{2u^2}\left[(\theta_2 - \theta_1) + \frac{1}{2}(\sin 2\theta_2 - \sin 2\theta_1)\right]$$

and is independent of the distribution of the circulation along the blades. Hence,

$$\xi_2 = \frac{-|\eta_1|}{\cos\theta_1 \cos\theta_2}\left[(\theta_2 - \theta_1) + \frac{1}{2}(\sin 2\theta_2 - \sin 2\theta_1)\right]$$

There is an interesting interpretation for the integral

$$\int_1^2 d\theta/q^2$$

in Hawthorne's relation. Mapping the (x, y) plane (Fig. 2) on the plane with polar coordinates $(1/q, \theta)$, a figure for the stream lines is obtained, where areas with the origin as pole are corresponding with the value of the integral

$$\int_1^2 d\theta/q^2$$

Therefore, the secondary vorticity ξ is, apart for a factor, equal to areas in the plane of the reciprocal hodograph. This plane is represented in Fig. 3.

The curve (a) corresponds with a typical stream line in the configuration of Squire and Winter[4] (q = constant), while curve (b) corresponds with a stream line in the Stephenson's cascade with an infinite number of blades ($u = q\cos\theta$ = constant).

REFERENCES

[1] Stephenson, J. M., *Secondary Flow in Cascades*, Readers' Forum, Journal of the Aeronautical Sciences, Vol. 18, No. 10, p. 699, October, 1951.

[2] Eichenberger, H. P., *Note about Secondary Flow in Cascades*, Readers' Forum, Journal of the Aeronautical Sciences, Vol. 19, No. 2, p. 137, February, 1952.

[3] Hawthorne, W. R., *Secondary Circulation in Fluid Flow*, Proc. of the Royal Society of London, Series A, Vol. 206, No. A 1086, pp. 374–387, May 7, 1951.

[4] Squire, H., and Winter, K. G., *The Secondary Flow in a Cascade of Airfoils in Nonuniform Stream*, Journal of the Aeronautical Sciences, Vol. 18, No. 4, p. 271, April, 1951.

The von Kármán Integral Method as Applied to a Turbulent Boundary Layer

Nguyen Van Le

Gas Turbine Laboratory, Massachusetts Institute of Technology

May 2, 1952

THE PRESENT two-dimensional incompressible boundary-layer equation

$$\frac{\tau_0}{\rho U^2} - \frac{d\theta}{dx} - \left(\frac{\delta^*}{\theta} + 2\right)\frac{\theta}{U}\frac{dU}{dx} = 0 \qquad (1)$$

was obtained by Gruschwitz (reference 1, p. 118) by integrating, across the boundary-layer thickness, the Navier-Stokes equations simplified by Prandtl. The same result was later obtained by von Kármán by considering a control volume.

As derived, this equation is applied to laminar, as well as turbulent, boundary layer. However, recent investigations[2, 3] show that the equation fails to give suitable results in cases of positive pressure gradients. It considers only the mean flow. The object of this note is to present a simple derivation of the boundary-layer equation in a turbulent incompressible two-dimensional flow, taking into consideration the time components of the velocity. It will make use of the von Kármán integral method and of the results available from the derivation of Eq. (1). (See Fig. 1.)

Application of the momentum theorem to this control volume gives

$$-\frac{\delta}{\rho}\frac{\partial p}{\partial x} - \frac{\tau_0}{\rho} = \frac{\partial}{\partial x}\int_0^\delta u^2\, dy - U\frac{\partial}{\partial x}\int_0^\delta u\, dy$$

Upon taking the time average, one obtains

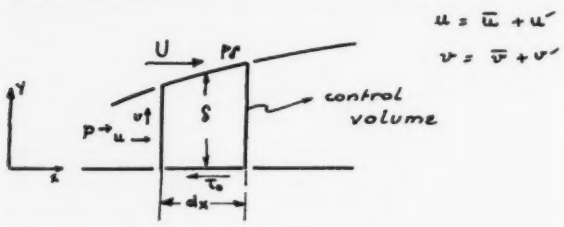

FIG. 1.

$$-\frac{\delta}{\rho}\frac{\partial \bar{p}}{\partial x} - \frac{\tau_0}{\rho} = \frac{\partial}{\partial x}\int_0^\delta \bar{u}^2\,dy - U\frac{\partial}{\partial x}\int_0^\delta \bar{u}\,dy \qquad (2)$$

With $u = \bar{u} + u'$ and $\overline{u^2} = \bar{u}^2 + \overline{u'u'}$, Eq. (2) becomes

$$-\frac{\delta}{\rho}\frac{\partial \bar{p}}{\partial x} - \frac{\tau_0}{\rho} = \frac{\partial}{\partial x}\int_0^\delta \bar{u}^2\,dy - U\frac{\partial}{\partial x}\int_0^\delta \bar{u}\,dy + \frac{\partial}{\partial x}\int_0^\delta \overline{u'u'}\,dy \qquad (3)$$

Because of the fluctuation components, $\partial\bar{p}/\partial x$ can no longer be calculated as usual from the flow outside the boundary layer With the usual assumptions for boundary-layer study, the dynamic equation in the y direction gives (reference 1, p. 337)

$$-\frac{1}{\rho}\frac{\partial \bar{p}}{\partial y} = \frac{\partial}{\partial x}\overline{u'v'} + \frac{\partial}{\partial y}\overline{v'v'} \qquad (4)$$

Assuming $\overline{v'v'} = 0$ at $y = 0$, $y = \delta$, one obtains from Eq. (4)

$$p_0 - \bar{p}_\delta = \rho\int_0^\delta \frac{\partial}{\partial x}\overline{u'v'}\,dy$$

$$p_0 - \bar{p} = \rho\int_0^y \left(\frac{\partial}{\partial x}\overline{u'v'} + \frac{\partial}{\partial y}\overline{v'v'}\right)dy$$

$$\bar{p} = \bar{p}_\delta + \rho\int_0^\delta \frac{\partial}{\partial x}\overline{u'v'}\,dy - \rho\int_0^y \left(\frac{\partial}{\partial x}\overline{u'v'} + \frac{\partial}{\partial y}\overline{v'v'}\right)dy$$

$$\frac{1}{\rho}\frac{\partial \bar{p}}{\partial x} = \frac{1}{\rho}\frac{d\bar{p}_\delta}{dx} + \int_0^\delta \frac{\partial}{\partial x}\overline{u'v'}\,dy - \int_0^y \frac{\partial}{\partial x}\left(\frac{\partial}{\partial x}\overline{u'v'} + \frac{\partial}{\partial y}\overline{v'v'}\right)dy$$

Thus $\partial\bar{p}/\partial x$ is a variable in y through the last term. As understood from the momentum theorem applied to the previous control volume, $(\delta/\rho)(\partial\bar{p}/\partial x)$ in Eqs. (2) and (3) is the mean value in the y direction; therefore,

$$\left(\frac{\delta}{\rho}\frac{\partial \bar{p}}{\partial x}\right)_{\substack{\text{mean value in}\\ y\text{ direction}}} = \frac{\delta}{\rho}\frac{d\bar{p}_\delta}{dx} + \delta\int_0^\delta \frac{\partial}{\partial x}\overline{u'v'}\,dy - \int_0^\delta\int_0^y \frac{\partial}{\partial x}\left(\frac{\partial}{\partial x}\overline{u'v'} + \frac{\partial}{\partial y}\overline{v'v'}\right)dy\,dy \qquad (5)$$

Putting Eq. (5) in Eq. (3), dividing by U^2, and rearranging, we get

$$\frac{\delta}{\rho U^2}\frac{d\bar{p}_\delta}{dx} + \frac{\tau_0}{\rho U^2} + \frac{\partial}{\partial x}\int_0^\delta \frac{\bar{u}^2}{U^2}\,dy - \frac{\partial}{\partial x}\int_0^\delta \frac{\bar{u}}{U}\,dy = -\frac{1}{U^2}\int_0^\delta \frac{\partial}{\partial x}\overline{u'u'}\,dy - \frac{\delta}{U^2}\int_0^\delta \frac{\partial}{\partial x}\overline{u'v'} + \frac{1}{U^2}\int_0^\delta\int_0^y \frac{\partial}{\partial x}\left(\frac{\partial}{\partial x}\overline{u'v'} + \frac{\partial}{\partial y}\overline{v'v'}\right)dy\,dy \qquad (6)$$

The left-hand member of this equation is recognized to be the one obtained with the mean value of the velocity by von Kármán (reference 4, p. 132). With the usual definition

$$\text{Displacement thickness } \delta^* = \int_0^\delta \left(1 - \frac{\bar{u}}{U}\right)dy$$

$$\text{Momentum thickness } \theta = \int_0^\delta \frac{\bar{u}}{U}\left(1 - \frac{\bar{u}}{U}\right)dy$$

it yields the classical equation, Eq. (1), Eq. (6) is written immediately as

$$\frac{\tau_0}{\rho U^2} - \frac{d\theta}{dx} - \left(\frac{\delta^*}{\theta} + 2\right)\frac{\theta}{U}\frac{dU}{dx} = -\frac{1}{U^2}\int_0^\delta \frac{\partial}{\partial x}\overline{u'u'}\,dy - \frac{\delta}{U^2}\int_0^\delta \frac{\partial}{\partial x}\overline{u'v'}\,dy + \frac{1}{U^2}\int_0^\delta\int_0^y \frac{\partial}{\partial x}\left(\frac{\partial}{\partial x}\overline{u'v'} + \frac{\partial}{\partial y}\overline{v'v'}\right)dy$$

Together with reference 3, this study gives a parallel result to those of Gruschwitz and von Kármán mentioned previously. Experimental work is now directed toward the correlation of the time components of the velocities.

REFERENCES

[1] Schlichting, H., *Grenzschicht-Theorie.*

[2] Rubert, Kennedy F., and Persh, Jerome, *A Procedure for Calculating the Development of Turbulent Boundary Layer Under the Influence of Adverse Pressure Gradients*, N.A.C.A. T.N. No. 2478, 1951.

[3] Bidwell, J. M., *Application of the von Kármán Momentum Theorem to Turbulent Boundary Layers*, N.A.C.A. T.N. No. 2471, 1951.

[4] Goldstein, S., *Modern Development in Fluid Mechanics.*